

NOTE TO USERS

This reproduction is the best copy available.

UMI[®]

**HEAT RECOVERY FROM MOLTEN BLAST FURNACE SLAG
IN A FLUIDIZED BED**

by

MARK M^cQUEEN

A thesis submitted to the Department of Mining Engineering
in conformity with the requirements for
the degree of Master of Science (Engineering)

Queen's University
Kingston, Ontario, Canada
December, 2000

copyright © M. M^cQueen, 2000



National Library
of Canada

Acquisitions and
Bibliographic Services

395 Wellington Street
Ottawa ON K1A 0N4
Canada

Bibliothèque nationale
du Canada

Acquisitions et
services bibliographiques

395, rue Wellington
Ottawa ON K1A 0N4
Canada

Your file Votre référence

Our file Notre référence

The author has granted a non-exclusive licence allowing the National Library of Canada to reproduce, loan, distribute or sell copies of this thesis in microform, paper or electronic formats.

The author retains ownership of the copyright in this thesis. Neither the thesis nor substantial extracts from it may be printed or otherwise reproduced without the author's permission.

L'auteur a accordé une licence non exclusive permettant à la Bibliothèque nationale du Canada de reproduire, prêter, distribuer ou vendre des copies de cette thèse sous la forme de microfiche/film, de reproduction sur papier ou sur format électronique.

L'auteur conserve la propriété du droit d'auteur qui protège cette thèse. Ni la thèse ni des extraits substantiels de celle-ci ne doivent être imprimés ou autrement reproduits sans son autorisation.

0-612-55918-1

Canada

ABSTRACT

A method for heat recovery from molten blast furnace slag was investigated using a fluidized bed and a molten LiCl-KCl salt mixture with eutectic composition, which acted as a low temperature analogue of the slag. The amount of energy contained within the blast furnace slag is approximately 3% of the total energy requirement of an integrated steel mill. The recovery of this energy can reduce fuel costs and decrease the amount of carbon dioxide released.

The effects of air flowrate, molten salt feedrate, and bed mass on the heat transfer characteristics of the fluidized bed were studied. Convective gas to particle heat transfer coefficients were measured in the fluidized bed and found to be in the range of 360 to 730 W/m²K. The heat recovery efficiency ranged from 65 to 82%. These values were confirmed by a heat transfer modeling program written in Microsoft Excel. In addition, the model predicted the effect of various feed and bed properties.

Particle growth and agglomeration caused significant temporal changes in the bed properties, which affected the heat transfer and the bed operation. It was found that the molten salt feedrate and the mass of the fluidized bed did not directly affect heat transfer; rather these variables altered the regime of fluidization, which in turn influenced both the operation of the bed and the heat transfer processes within it. These considerations, which were not modeled, were responsible for the discrepancy between the model prediction and the experimental work.

ACKNOWLEDGEMENTS

It is with pleasure that I gratefully acknowledge my thesis supervisors Dr. C.A. Pickles whose support and wisdom assisted me greatly through the course of this project, and Dr. R. Sridhar who suggested the problem and whose enthusiasm towards it made this project enjoyable and educational.

I would also like to express my appreciation to others:

To my parents, Nairn and Cheryl McQueen, whose undying support and encouragement helped me throughout this undertaking;

To my grandmother, who assisted me financially;

To my girlfriend, Jodi Phillips, for her patience and sense of humour;

To Dr. V.I. (Lucky) Lakshmannan for providing the space and equipment for my experiments;

To everyone at Process Research ORTECH that assisted me, especially Dr. Jun (John)

Shu, Bob deLaat, Marion Gotts, Marc Rishia, and Pat Ross-Smith;

To Dieter Engel at Emerald Glass for his skilled artisanship.

CONTENTS

1.0	<u>INTRODUCTION</u>	1
1.1	<u>BLAST FURNACE OPERATION</u>	3
1.1.1	<i>Process Chemistry</i>	3
1.1.2	<i>Energy Requirements</i>	6
1.1.3	<i>Coking Requirements</i>	7
1.1.4	<i>Gas Distribution</i>	9
1.1.5	<i>Residence Time</i>	10
1.1.6	<i>Slag Production</i>	11
1.2	<u>SCOPE</u>	14
2.0	<u>LITERATURE REVIEW</u>	16
3.0	<u>THEORY</u>	38
3.1	<u>FLUID MECHANICS</u>	38
3.2	<u>MODEL DESCRIPTION</u>	44
3.2.1	<i>Heat Transfer from a Falling Molten Droplet</i>	44
3.2.3	<i>Gas to Particle Heat Transfer</i>	47
3.2.4	<i>Bed to Wall Heat Transfer</i>	51
3.2.5	<i>Normal Model Operation</i>	52
3.2.6	<i>Reverse Model Operation</i>	53
4.0	<u>APPARATUS</u>	56
4.1	<u>FEED MATERIAL</u>	56
4.2	<u>EQUIPMENT</u>	57
4.3	<u>EXPERIMENTAL DESIGN</u>	64
5.0	<u>RESULTS AND DISCUSSION</u>	68
5.1	<u>MODEL PREDICTIONS</u>	68
5.1.1	<i>Analysis of Model Data</i>	69

<u>5.2</u>	<u>EXPERIMENTAL DATA</u>	84
<u>5.2.1</u>	<u>Bed Mass</u>	84
<u>5.2.2</u>	<u>Salt Feedrate</u>	92
<u>5.2.2.1</u>	<u>Mechanisms of Particle Growth</u>	100
<u>5.2.3</u>	<u>Air Flowrate</u>	103
<u>5.3</u>	<u>INDUSTRIAL CONSIDERATIONS</u>	112
<u>6.0</u>	<u>CONCLUSION AND RECOMMENDATIONS</u>	120
<u>7.0</u>	<u>LITERATURE CITATIONS</u>	123
<u>APPENDIX A</u>	126

TABLES

Table 1.1 Global Warming Potentials (GWP) of Common Pollutants (Lupis, 1999).	2
Table 4.1. Bounds of experiments conducted in this study.	67
Table 5.1. Modeling conditions for the Excel algorithm.	69
Table 5.2. Modeled response of the fluidized bed heat recovery system to changes in system parameters.	70
Table 5.3. Comparison of the difference between the actual and the predicted gas to particle heat transfer coefficients when expressed as a function of salt feedrate and bed mass.	91
Table 5.4. Difference between the experimental data and the predicted gas to particle heat transfer coefficients as a function of time for a salt flowrate of 1.22 g/min and a bed mass of 125g.	98
Table 5.5 Differences between the experimental and the predicted gas to particle heat transfer coefficients as a function of time for a salt flowrate of 1.18 g/min and a bed mass of 100g.	99
Table 5.6. Correlation between the actual and the predicted gas to particle heat transfer coefficients. The values shown in the table are the percentage differences between the actual and the predicted values.	107

FIGURES

<u>Figure 1.1 Trends in world steel production since 1970</u>	4
<u>Figure 1.2 Sectional diagram of a blast furnace..</u>	8
<u>Figure 2.1 Three forms of blast furnace slag: (a) air-cooled; (b) foamed; (c) granulated.</u>	18
<u>Figure 2.2 Scanning electron micrograph of untreated slag aggregate at 1000X magnification..</u>	20
<u>Figure 2.3 Scanning electron micrograph of slag aggregate treated at 1000°C at 3000X</u> <u>magnification.....</u>	20
<u>Figure 2.4 Impinging jet atomization.</u>	22
<u>Figure 2.5 Schematic diagram of the methanation-steam reformation process for heat recovery</u> <u>from molten slag.....</u>	23
<u>Figure 2.6 Schematic diagram of the experimental apparatus to measure the rate of the CH₄-H₂O</u> <u>reaction</u>	25
<u>Figure 2.7 Lay-out of the NKK/Mitsubishi air granulation plant.....</u>	27
<u>Figure 2.8 Lay-out of the NKK cooling drum process</u>	28
<u>Figure 2.9 Dry slag granulation by Kvaerner Metals</u>	30
<u>Figure 2.10 Rotary-cup, air-blast atomizer.....</u>	33
<u>Figure 2.11 Molten slag granulation and fluid bed heat recovery plant.....</u>	34
<u>Figure 2.12 Heat recovery from molten blast furnace slag to produce steam</u>	36
<u>Figure 3.1 Pressure drop versus velocity for a fluidized bed of sand</u>	40
<u>Figure 3.2 The Geldart classification of particles for air at ambient condition.</u>	42
<u>Figure 4.1 Phase diagram of the KCl-LiCl system.....</u>	58
<u>Figure 4.2 Fluidized bed and molten salt feeder configuration</u>	62
<u>Figure 4.3 Quartz feeders used for fluid bed heat recovery in this study..</u>	63
<u>Figure 5.1 Effect of salt feed temperature on the droplet and gas to particle heat transfer</u> <u>coefficients.</u>	71
<u>Figure 5.2 Effect of salt feedrate on the droplet and gas to particle heat transfer coefficients.....</u>	72
<u>Figure 5.3 Effect of droplet size on the droplet and gas to particle heat transfer coefficients.....</u>	74
<u>Figure 5.4 Effect of bed particle density on the droplet and gas to particle heat transfer</u> <u>coefficients.</u>	76

<u>Figure 5.5 Effect of bed particle size on the droplet and gas to particle heat transfer coefficients.</u>	77
.....	
<u>Figure 5.6 Effect of bed mass on the droplet and gas to particle heat transfer coefficients.</u>	78
<u>Figure 5.7 Effect of air flowrate on the droplet and gas to particle heat transfer coefficients.</u>	79
<u>Figure 5.8 Effect of air preheat temperature on the droplet and gas to particle heat transfer coefficients</u>	81
.....	
<u>Figure 5.9 Effect of air pressure on the droplet and gas to particle heat transfer coefficients.</u>	82
<u>Figure 5.10 The gas to particle heat transfer coefficient as a function of the bed mass for various molten salt feedrates. The air flowrate in all cases is 0.078m³/min.</u>	86
<u>Figure 5.11 The gas to particle heat transfer coefficient as a function of the bed mass for various molten salt feedrates. The air flowrate in all cases is 0.085m³/min.</u>	87
<u>Figure 5.12 Change in fluidization regimes with solids type and gas velocity</u>	89
<u>Figure 5.13 The gas to particle heat transfer coefficient as a function of the molten salt feedrate for various air flowrates. The fluidized bed had an initial mass of 100g.</u>	93
<u>Figure 5.14 The gas to particle heat transfer coefficient as a function of the molten salt feedrate for various air flowrates. The fluidized bed had an initial mass of 125g.</u>	94
<u>Figure 5.15 The gas to particle heat transfer coefficient as a function of the molten salt feedrate for various air flowrates. The fluidized bed had an initial mass of 150 g.</u>	95
<u>Figure 5.16 (a) Photograph of 150g of initial bed material operating with a molten salt flowrate of approximately 1.0g/min; (b) Photograph of 150g of initial bed material operating with a salt flowrate of approximately 4.9g/min; (c) Defluidization of a bed of 100g initial mass due to the formation of large agglomerates in the fluidized zone.</u>	102
<u>Figure 5.17 The gas to particle heat transfer coefficient as a function of the air flowrate for various molten salt feedrates. The fluidized bed had an initial mass of 100g.</u>	104
<u>Figure 5.18 The gas to particle heat transfer coefficient as a function of the air flowrate for various molten salt feedrates. The fluidized bed had an initial mass of 125g.</u>	105
<u>Figure 5.19 The gas to particle heat transfer coefficient as a function of the air flowrate for various molten salt feedrates. The fluidized bed had an initial mass of 150g.</u>	106
<u>Figure 5.20 Correlation between the predicted gas to particle heat transfer coefficient and the heat recovery efficiency</u>	109
<u>Figure 5.21 Correlation between the predicted gas to particle heat transfer coefficient and the heat recovery efficiency for a slugging bed.</u>	111
<u>Figure 5.22 Emission reductions and economic gain with heat recovery from blast furnace slag.</u>	113
.....	

Figure 5.23 Time required for solid spheres to reach within 1% of the fluidized bed operating temperature for the system used in this study. 117

NOTATION

Variables

u_{mf}	minimum fluidization velocity, m/s
u_o	superficial air velocity, m/s
ϵ_m	void fraction of packed bed, dimensionless
ϵ_{mf}	void fraction of incipiently fluidized bed, dimensionless
ΔP	pressure drop across bed, kPa
μ_f	effective shear viscosity for fluid phase, Pas
μ_A	effective shear viscosity for air, Pas
ρ_f	density of fluid, kg/m ³
ρ_p	density of particle, kg/m ³
ρ_A	density of air, kg/m ³
ρ_D	density of molten salt droplet
ρ_p^p	density of particle fluidizing at higher velocity, kg/m ³
ρ_p^f	density of particle fluidizing at lower velocity, kg/m ³
D_D	diameter of molten droplet, m
d_m	mean particle diameter, m
d^p	diameter of particle fluidizing at higher velocity, m
d^f	diameter of particle fluidizing at lower velocity, m
g	acceleration due to gravity, m/s ²
$v_{A \rightarrow D}$	relative velocity between falling molten droplet and passing air, m/s
x_f	mole fraction of particles that fluidize at lower velocity, %mol/mol
h_D	convective heat transfer coefficient between air and molten droplet, W/m ² K
k_A	thermal conductivity of air, W/mK
\dot{m}_A	mass flowrate of air, kg/s
\dot{m}_S	mass flowrate of molten salt, kg/s
\dot{N}_{drops}	flowrate of molten salt drops, drops/s
A_D	area of one molten salt droplet, m ²
V_D	volume of one molten salt droplet, m ³
$A_{eff,bed}$	effective area of the fluidized bed, m ²
$A_{eff,bed}^*$	effective area of the fluidized bed determined by the computer algorithm, m ²
$A_{internals}$	area of internals immersed in the fluidized bed, m ²
t_{fall}	free-fall time experienced by a molten salt droplet, s
d_{fall}	free-fall distance experienced by a molten salt droplet, s

c_p	specific heat capacity, J/molkg
$T_{A,in}$	feed temperature of the air, K
$T_{A,exhaust}$	temperature of the air exiting the reactor, K
T_{bed}	temperature of the bed, K
$T_{S,in}$	feed temperature of the molten salt, K
$T_{S,bed}$	temperature of the salt as it enters the fluidized region, K
T_{wall}	temperature of the reactor wall, K
T_{∞}	temperature of the surroundings, K
ΔH_{fusion}	heat of fusion of the molten salt
h_{gp}	convective gas to particle heat transfer coefficient, W/m ² K

Dimensionless groups

Re	$\equiv \frac{\rho_f du}{\mu}$, Reynold's number
Nu	$\equiv \frac{hd}{k}$, Nusselt number
Pr	$\equiv \frac{\mu c_p}{k}$, Prandtl number
Ga	$\equiv \frac{d^3 \rho_f^2 g}{\mu^2}$, Galileo's number
Bi	$\equiv \frac{hV}{kA}$, Biot number
Ar	$\equiv \frac{d^3 g(\rho_p - \rho_f)\rho_f}{\mu^2}$, Archimedes' number

1.0 Introduction

The earth's surface and the lower atmosphere are partially heated by radiation from atmospheric gases that absorb energy emitted by the planet and re-radiate it back towards the surface. In this way, the natural greenhouse effect causes the earth's surface to be approximately 33K higher than it would be otherwise. The two most significant greenhouse gases are carbon dioxide and water vapour, both of which are highly emissive species. Other gases such as methane, nitrous oxide (N_2O), ozone, and chlorofluorocarbons contribute an additional warming effect equivalent to fifty percent of that of carbon dioxide. An increase in the amounts of any of these gases implies that more energy will be re-radiated back to the planet's surface, causing an increase in the average surface temperature.

An equal increase in each gas will not generate the same response, since some gases emit more radiation than others. In order to directly compare the effect of releasing different gases into the atmosphere, a factor known as the global warming potential (GWP) has been developed (Lupis, 1999). The GWP uses carbon dioxide as a baseline gas, and relates the warming potentials of other gases to this value. For example, one mole of methane has 24.5 times the global warming potential of carbon dioxide. These factors for various gases are included in Table 1.1. Alternatively, emissions may be accounted for in terms of their carbon equivalent. Although much debate exists over the severity of global warming, it is a fact that for roughly 1000 years preceding the dawn of the industrial revolution, atmospheric carbon dioxide concentrations remained relatively constant at 280 ppm. In the last 150 years, the concentration has risen to over 350 ppm,

Table 1.1 Global Warming Potentials (GWP) of Common Pollutants (Lupis, 1999).

Gas	Atmospheric Lifetime (yr)	GWP
Carbon dioxide (CO ₂)	50 to 200	1
Methane (CH ₄)	12	24.5
Nitrous oxide (N ₂ O)	120	320
Various hydrofluorocarbons (C _x H _y F _a)	1.5 to 264	140 to 12,100
Perfluorinated carbons (C _x H _y F _b)	10,000 to 50,000	9400
SF ₆	3200	24,900

an increase of over 25% (Martocci, 1996). The additional carbon dioxide can be attributed to fossil-fuel combustion, natural gas flaring, cement production, cattle ranching, rice paddies, deforestation, and mining and metallurgy: these are all anthropogenic sources (Nagasawa, 1996). In order to achieve stabilization of greenhouse gas emissions, drastic measures must be taken. Models of the carbon cycle predict that in order to achieve immediate stabilization of CO₂ at its present level, an immediate reduction of emissions on the order of 50-70% would be required, along with subsequent further reductions. Nitrous oxide would require a reduction of about 50% to stabilize its concentration, and most of the other greenhouse gases (except methane) have such long atmospheric lifetimes that their emissions would have to be virtually eliminated as soon as possible.

The main source of CO₂ emissions is clearly fossil fuel combustion; in 1984, 5.3 x 10⁹ metric tons of carbon were released into the atmosphere in this manner, whereas only 0.4-0.8 x 10⁹ tons were produced by tropical deforestation (Forrest, 1991). The primary metals industry is a large consumer of energy, and thus of fossil fuels. In 1985, the energy consumption of the United States' primary metals industry was estimated at 2.477

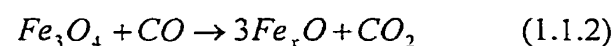
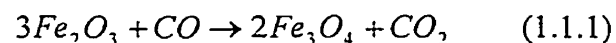
exajoules, and carbon emissions at 65.6 Mt (Forrest, 1991). Although these numbers represent a considerable decrease from 1968 levels, the carbon emissions, when extrapolated to global proportions, represent a significant portion of the five billion tons of carbon released in 1984. Any decrease in the overall global emission of greenhouse gases must be paralleled by changes or reductions in the primary metals industry. These modifications cannot exclude the steel industry, which has increased its output by approximately fifty percent in the last thirty years. The growth of steel production is evident in Figure 1.1.

The ultimate goal is to achieve emissions reductions without affecting the ability of a process to compete economically. Solutions to this problem require an appreciation of the technology. For this reason, a discussion regarding blast furnace operation, and in particular energy efficiency, is included below. It is meant primarily as background information, and although it is somewhat detailed, it by no means conveys the enormous complexities involved in ironmaking.

1.1 Blast Furnace Operation

1.1.1 Process Chemistry

The ultimate goal of any blast furnace is to reduce iron oxide to metallic iron. The main reactions are as follows:



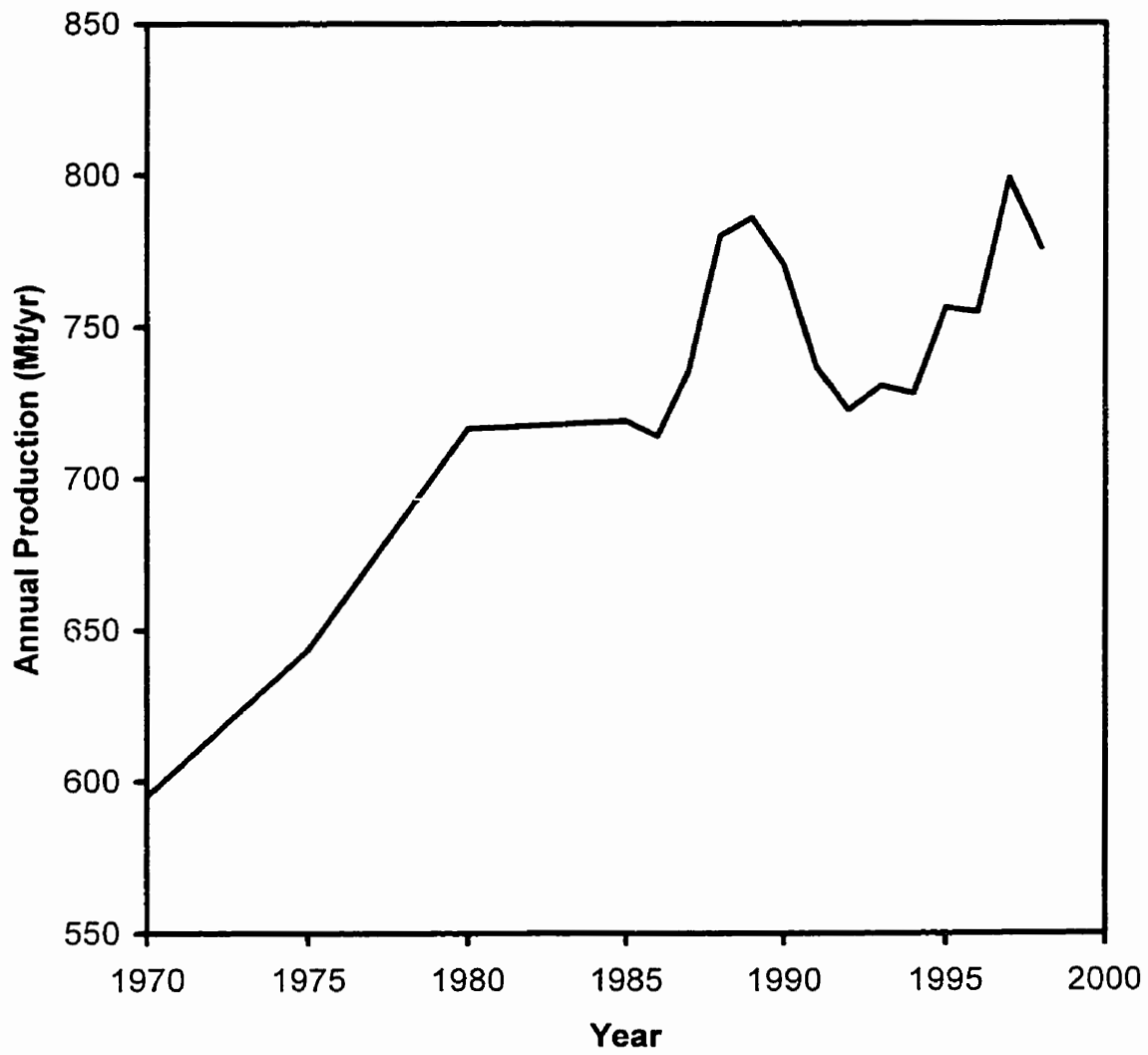


Figure 1.1 Trends in world steel production since 1970 (Norris, 1999).

The overall reaction is endothermic, and the combustion of carbon in the blast furnace provides the energy. Once significant reduction to Fe_3O_4 has occurred (which happens readily given the correct CO/CO_2 ratio in any blast furnace), an additional reaction may take place



This is known as Bells' reaction and is strongly exothermic, with a reaction rate maximum at 823K. This reaction is important because it provides about 11% of the carbon needed for the direct reduction of Fe_2O_3 . Further down in the furnace, at the higher temperatures, the limestone (if added) decomposes endothermically to produce CO_2 . This reaction is undesirable since it leads to thermal inefficiencies. Also, if the limestone is fed in large enough sizes, decomposition will not fully occur until a temperature of 1273K is reached, at which point carbon monoxide is formed endothermically via the reverse of reaction (1.1.5), further contributing to the inefficiency. The current practice of using prefluxed sinter and prefluxed pellets has reduced the amount of limestone added to the furnace, thereby reducing this inefficiency.

When the solids have reached a temperature of 1273K (i.e. when they have descended to an adequate depth in the furnace), a mixture of Fe and Fe_xO usually exists. Reduction by reaction (1.1.3) no longer occurs, but rather is achieved by reaction (1.1.4), which is actually the sum of reaction (1.1.3) and the reverse of reaction (1.1.5), which is known as Boudouard's reaction, or the Endothermic Gasification of Carbon (EGC). This is referred to as direct reduction, and is strongly endothermic.

Slag is formed from the silica and the alumina present in the coke, gangue in the concentrate, and from lime or magnesia. The overall composition must be such that it is fully liquid at the temperature in the furnace. If the temperature/composition

combination dictates that the slag is outside of the eutectic valley, less liquid slag is present. Thus, its effectiveness is greatly reduced because its effective liquid, or reactive, volume is decreased. It should be noted that in a large furnace, the slag composition varies across the hearth diameter.

In this discussion of process chemistry, it is important to remember that the energy for the above reactions is provided by the heat of combustion of metallurgical coke. Upon entrance to the furnace, the oxygen, the water vapour, and any injected hydrocarbons are reacted to produce carbon monoxide; the principal reducing agent in the furnace. Silica may also react with carbon to produce carbon monoxide, and this reaction increases the silicon content of the metal.

1.1.2 Energy Requirements

The energy design parameters for a blast furnace are the heat supplied by the blast air, the heat absorbed by the slag and the hot metal, and the heat leaving the system in the top gas. In addition, some heat is lost to the furnace walls. However, the most important design criteria is that the gas phase is above the temperature required to heat the iron and the slag to the necessary temperatures (usually around 1620 K). A drawing of a typical blast furnace is given in Figure 1.2.

In general, it can be assumed that there are three zones present in the furnace. In the first, the exiting top gas preheats the solid phase. The solid phase heats up as it moves down through the furnace, and the bosh gas cools as it rises. At a specific point in the furnace, the solids and the gas are at the same temperature. This pinch point is known as the thermal reserve zone, and the temperature of both phases is typically near 1300 K. The third zone is located at the bottom of the furnace, where the bosh gases are the hottest. Here, it is essential that the molten metal reaches a temperature of 1620 K so that

a quality, usable product will result. Thus, the combustion must be controlled such that the adiabatic flame temperature is high enough that the temperature of the metal and the slag components will be raised from 1300 K to 1620 K.

1.1.3 Coking Requirements

Coke is added to a blast furnace for three reasons: to provide a good reducing atmosphere, to provide a fuel source, and to give structure to the furnace. Coke is manufactured on the ironmaking site using a number of different coals. Coke manufacture is an energy-intensive operation, accounting for nearly 4% of the total energy requirements of an operating unit. The emission standard for NO_x for existing coke ovens is 350 ppm: a value that is easy to meet (Berry, 1994). The standard for new ovens of 170 ppm, however, will require changes to the combustion mechanism used (Berry, 1994). This will likely involve the use of Ultra-Low NO_x Burners (ULNB), or the employment of one of many NO_x reduction strategies such as reburning, internal or external flue gas recirculation, and selective catalytic or selective non-catalytic reduction. Thus, possible techniques do exist; it is merely a matter of cost.

In coke plants, a major concern is the CO_2 emissions. The most effective and economical solution is to reduce fossil fuel consumption as much as possible. A number of technologies, which have been developed in Japan, have been successful. One method is to reduce the moisture of the coal feed by using dryers, which in turn, will reduce the energy requirement of coke production and thus the specific fossil fuel use. Computer-based control mechanisms have been installed to regulate combustion in the ovens more

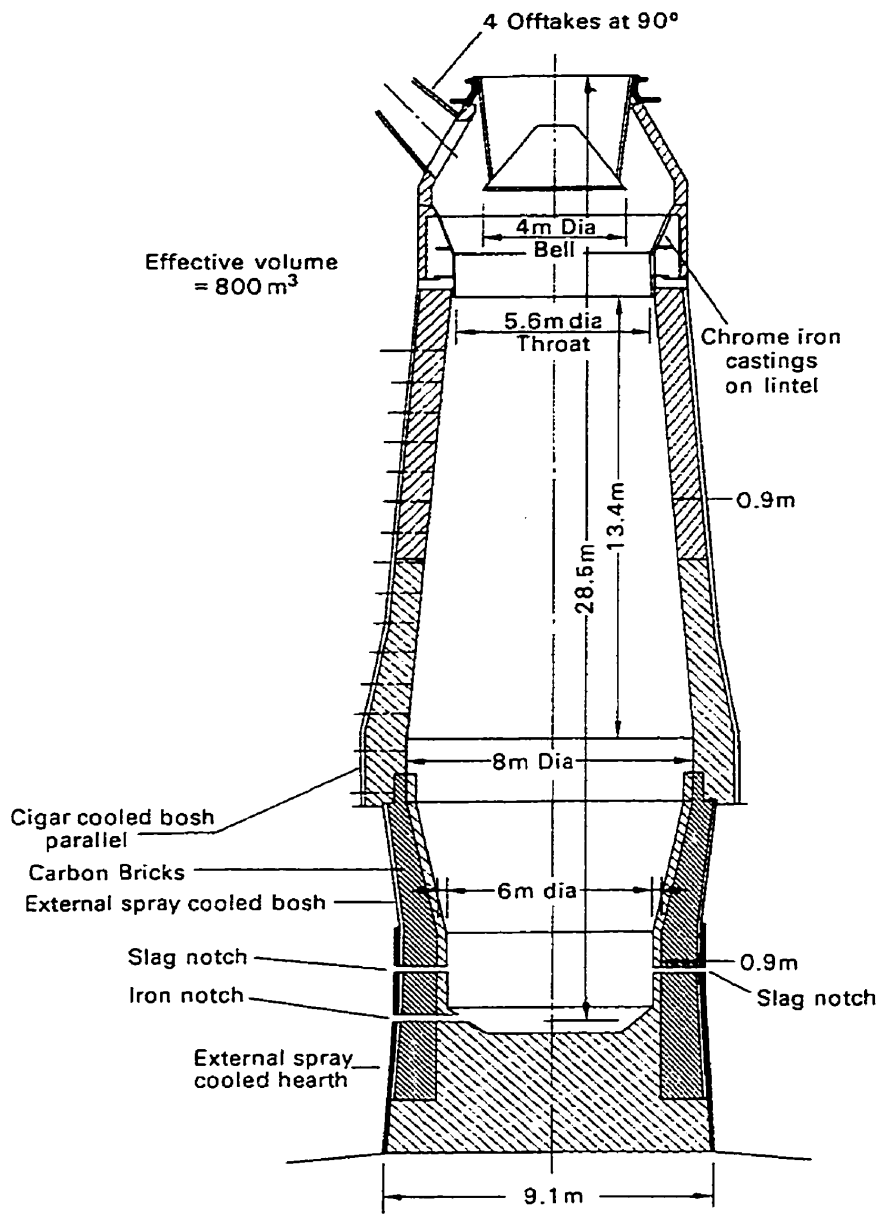


Figure 1.2 Sectional diagram of a blast furnace (Lee, 1974).

efficiently, and to govern waste heat facilities. By employing these technologies, coke oven producers have reduced energy consumption from nearly 900 Mcal/tonne of coke in 1980 to 440 Mcal/tonne of coke in 1992 (Nagasawa, 1996).

1.1.4 Gas Distribution

Because the production of hot metal is proportional to the amount of reducing gas supplied by the system, it is imperative that a given blower can provide the maximum possible blast. This requires that the pressure drop per unit length be minimized. A form of Ergun's equation stipulates that this parameter is related to the void fraction and the equivalent diameter of particles in the bed. Since the material fed to the top of the furnace is reacting as it descends, then the physical parameters will change. As well, the large temperature gradients in the furnace allow for correspondingly large gaseous density gradients, which also affects the local pressure drop. For example, resistance to flow (and hence pressure drop) increases when the gas density is high, when the particles are small, or when the void fraction is low. Both of the latter conditions increase as the feed material descends into the bosh and the hearth.

Generally, gases introduced into the blast furnace leave the tuyeres and immediately rise upwards in the furnace, and their momentum carries them toward the centre. As the gases reach a point where the solid particles are just beginning to melt (this occurs at the lower boundary of the cohesive zone), the gases encounter alternating layers of solid coke and softened ore. These materials have different physical characteristics, and hence different resistances to flow. As a result, the gases channel through the coke layers and proceed to rise through the rest of the feed material; channeling may also occur in the granular zone. Overall, channeling is an unwanted phenomenon from a mass transfer point of view; it represents superficial transport which

decreases interphase contact and slows the overall rate and extent of the reaction. Channeling may also occur if the particles are fed in a segregated fashion such that large particles collect in the centre of the furnace, and the smaller particles migrate outwards. In this case, the gas will channel through the region of large particles, resulting in poor utilization of the reducing gases. Thus, a problem faced by many designers is deciding how to best feed the furnace with solids at the top and hot air from the bottom in order to maximize intimate physical contact and hence efficient chemical reduction.

1.1.5 Residence Time

A number of different materials circulate to different degrees in the furnace, including sulphur, silicon, the alkalis, and carbon; the degree of recycle affects the residence time of the material, and increases its chance for reaction.

Nearly all the sulphur found in a furnace is introduced in the coke in the form of FeS (pyrrhotite), and as such does not react until the coke combusts. A number of intermediate species are formed, but upon cooling, sulphur is found either in the slag, in the form of CaS, or in the iron solution.

The majority of silicon enters the metal phase via the gas phase from the disproportionation of silicon monoxide to elemental silicon. The net reduction reaction is given below in Equation (1.1.6).



The reduction of silica can only be achieved in the presence of carbon. Since the carbon combustion reaction occurs at temperatures above 1673K, the silica reduction cannot occur above this furnace isotherm. Therefore, all silica reduction takes place between the tuyeres and this point. If the furnace has excess thermal energy, then the isotherm will be

located higher up in the furnace, and therefore the silicon content in the metal will be higher.

Sodium and potassium are troublesome alkalis that enter in the coke and the ores. Stable alkali cyanides form, and once part of the recirculating load of the furnace, produce carbonates. These compounds tend to build up in the furnace, as they can only be removed by reaction with acid slag constituents. Alkalis may also be absorbed by the iron oxide charge and coke, and lower their softening point and severely compromise their strength, respectively. In either case, the furnace permeability is decreased, and an increase in the unevenness of operation results. Evidence has also been provided to indicate that significant carbon recycling occurs in furnaces. This is caused by carbon deposition in the temperature range of 723K to 923K according to reaction (1.1.5). This reaction is catalyzed by metallic iron, and although it does not occur to any degree on many acid sinters, it does occur on both acid and fluxed pellets. The result of the carbon recycling is a change in the ore/coke ratio in the lower portion of the furnace, which leads to an overall thermal redistribution in the system. The amount of direct reduction occurring in the furnace is also affected. Because of these energetic ramifications, a constant oscillation of the thermal condition in the bosh and stack will be evident, and will result in the same variations in the hot metal temperature and the silicon content of the iron.

1.1.6 Slag Production

In the ironmaking process, a slag is produced which is a molten silicate complex formed by the combination of agglomerated earthy matter with the ore, fuel, and fluxes (Lee, 1974). Slag composition varies according to the extraction or refining process used, but in the case of slags produced in small blast furnaces, it is most often comprised

of three oxides, namely CaO, Al₂O₃, and SiO₂. Modern iron and steelmaking operations produce blast furnace slag at a rate on the order of 0.35 tons per ton of steel, or approximately 0.3 tons per ton of pig iron produced (Pickering, 1985). The annual worldwide production of steel was 776 million tons in 1998 (Norris, 1999), necessitating the production of approximately 270 million tons of blast furnace slag. Fortunately, slag has been considered a useful by-product of the iron and steelmaking process since Roman times. During this period, slag was commonly used as road cover. In the 19th century, slag was used for rail ballast and as a construction material for bridges. Slag is presently produced in three forms: air-cooled, foamed, and granulated, each of which possess different physical properties. Commercial uses of slag include:

- Slag cement;
- Concrete and concrete block aggregate;
- Railroad ballast;
- Bituminous pavements;
- Mineral wool;
- Roofing cover material;
- Sewage trickling filters;
- Highway and airport pavement base/sub-base construction aggregate;
- Agricultural uses such as soil conditioning;
- Landfill construction;
- Mine backfill material.

In addition to the above uses, slag is also a readily available source of heat. One ton of slag tapped from a blast furnace will typically have a temperature between 1673K

to 1873K, and contain 2-3% of the total energy required for the manufacturing of one ton of steel. Therefore, 0.4-0.6 GJ/ton of steel produced is available as a high quality heat stored within the molten slag (Pickering, 1985). If the heat is recovered quickly, the slag will be glassy, and this will allow it to be used in applications that place high value on slag by-products. As well, the recovered heat can be used to preheat blast furnace combustion gases or power turbines to generate electricity. The recovered heat represents energy that would otherwise be obtained by combusting fossil fuels, and results in a net decrease in carbon dioxide emissions. In the past twenty-five years, a number of processes have been proposed to recover heat from blast furnace slag. These will be discussed in further detail in Chapter 2. Generally, these processes were flawed: either the technology could not produce a valuable slag product or the mechanism of heat recovery was impractical.

As mentioned, ironmaking and steelmaking processes are energy intensive requiring on the order of 20 GJ per ton of steel shipped (Pickering, 1985). The vast amount of fossil fuels combusted generates 18 million tons of carbon dioxide annually in Canada, accounting for 2% of the total CO₂ emissions (Martocci, 1996). As the world's consumption of steel increases and environmental legislation tightens, it is evident that there is a need to decrease the unit carbon dioxide production in the iron and steel industries.

Some attempts have been made to improve the energy efficiency of the iron and steelmaking process, and there has been some success. Since the 1970s, the energy efficiency in North American mills has increased by approximately 45% and the carbon dioxide emissions have decreased by an approximately equal amount (Norris, 1999). In the 1990s alone, the energy consumption in Canadian mills has dropped by 15% and the

carbon dioxide emissions have been reduced by 12% (Norris, 1999). Most of these improvements have been achieved through a variety of mechanisms including those listed below (Sharkey, 1998):

- Phasing out open hearth furnaces;
- An increase in the use of continuous casting;
- Developing substitutes for coke in the blast furnace;
- Increasing the use and improving the process technologies of electric arc furnaces, which use no coke;
- Improving reheat furnace technology;
- Pioneering thin-slab casting which eliminates energy intensive process steps.

1.2 Scope

As an alternative to the above list of carbon dioxide reduction technologies, this study aims to employ a fluidized bed for heat recovery from molten blast furnace slag.

The objectives are threefold:

- To design a fluidized bed system allowing heat recovery from a molten material, and extend the results to industrial conditions;
- To use a low temperature analogue consisting of a LiCl/KCl eutectic mixture to determine the effect of molten feedrate, air temperature, air velocity, and bed particle size on the heat recovery and the heat transfer coefficients;
- Predicting the heat recovery and heat transfer coefficients of the eutectic system using mathematical models described in Excel Solver routines and comparing the calculated values to those obtained experimentally.

The remainder of this work begins with a literature review of processes designed to recover heat from blast furnace slag. The scientific and engineering theory governing the computer model is then given. Next, the apparatus used in this study is described, and the experimental design is justified. The results of both the computer model and the experimental work are discussed, from which a number of conclusions and recommendations are drawn.

2.0 Literature Review

As mentioned previously, blast furnace slag is being increasingly viewed as a co-product of the ironmaking process rather than as a waste material. This is largely due to growing environmental concerns regarding the volume of slag production, estimated to be in excess of 200 million tons worldwide in 1998 alone (Norris, 1999). The value of the blast furnace slag depends on the cooling and granulating processes, which can greatly influence the physical properties of the final product.

In order to recover energy from a slag, a heat transfer medium is required. The two most common media are air and water (Lee, 1974). The most widely used method to cool hot blast furnace slag is to pour the molten material into an open pit; water is then introduced to quench the slag. Large volumes of water are required in this operation, and environmentally unfriendly gases such as H_2S and SO_2 are emitted. A foamed product will result in this case. Alternatively, some facilities employ air-cooled pits, which alleviate the generation of the sulphur-based gases: however there is no opportunity for heat recovery. Wet granulation is a process that gives a more valuable product than slag processed in pits. In this case, molten slag falls from the end of a slag runner, and is atomized by impinging water jets. The slag is granulated into pellets on the order of 2-5 mm in diameter, which allows for extremely rapid cooling of the slag. As a result, the slag is extremely glassy (amorphous), and is therefore suitable for use in cement applications (Lee, 1974). The water is recycled, although some is lost as an acid mist. Some disadvantages of the wet granulation processes are possible groundwater contamination problems, high capital costs to eliminate pollution, high operating costs to

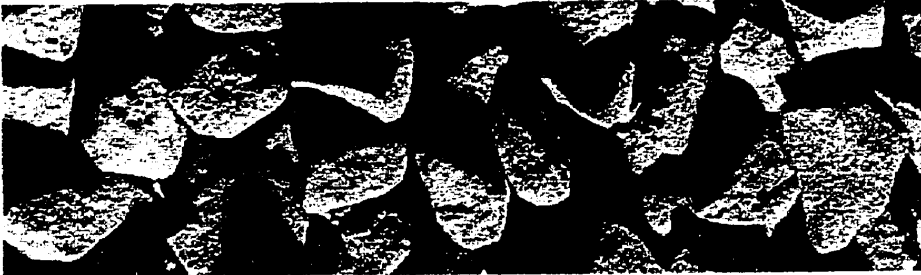
dry the pelletized product, and abrasive build-up in the recycled water stream causing maintenance problems.

A variation of wet granulation is wet pelletizing. In this case, water running over a rotating drum is used to atomize the slag. Water requirements are substantially less than in wet granulation, but the environmental problems associated with water contacting the slag remain. This process has been largely phased out and replaced by wet granulation technologies (Featherstone et al., 1998). The three main forms of blast furnace slag are shown in Figure 2.1.

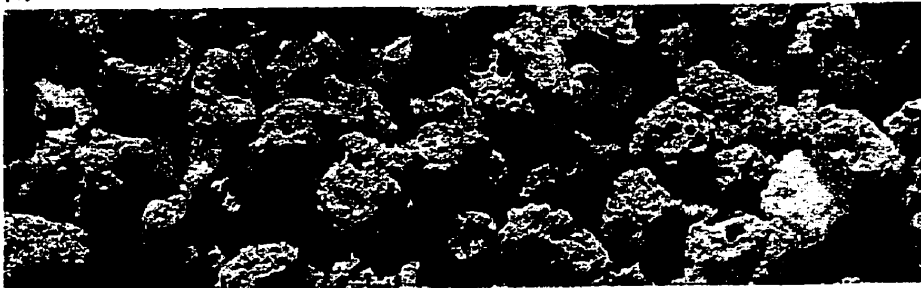
With environmental legislation becoming more stringent, many facilities have studied and implemented blast furnace slag treatment processes that use air instead of water; these techniques are said to be dry processes. There are many advantages to cooling blast furnace slag with air. When air-cooled blast furnace slag is crushed, its physical properties make it suitable for use as an aggregate: coated or uncoated. It has a rough surface texture giving good frictional properties, and adhesion to bituminous and cement binders are excellent. These features give air-cooled slag the best resistance (when compared to other road aggregates) to the stripping of the binder caused by the combined action of water and traffic (Lee, 1974). Furthermore, blast furnace slags produced using air-cooling methods perform well in many standard tests involved in road construction such as aggregate crushing value, polished stone value, and frost resistance. However, the speed of cooling also has an impact on the properties of the final product.

Figures 2.2 and 2.3 are photomicrographs of blast furnace slag, and demonstrate the effect of cooling speeds on the nature of the final product. In order to obtain the

(a)



(b)



(c)

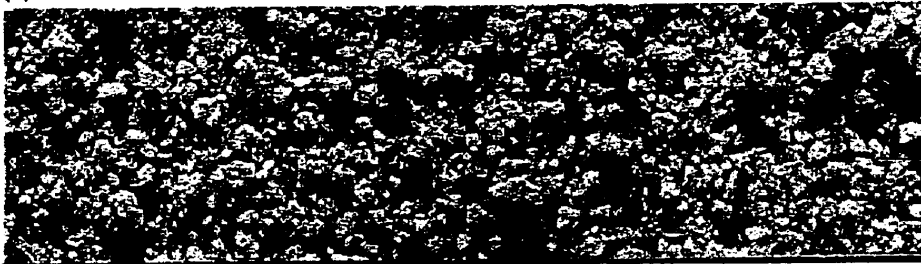


Figure 2.1 Three forms of blast furnace slag: (a) air-cooled; (b) foamed; (c) granulated. Crystals present in air-cooled slags range from microscopic size to 3 mm. Foamed slags range in particle size from <3 mm to 14 mm (Lee, 1974).

desired crystal structure shown in Figure 2.3, the slag was heat-treated at 1273K. The desired structure has primary texture at 10-15 μm and secondary texture at 1-5 μm , and this results in improved aggregate characteristics.

Slowly cooled slag is of lower value, suitable mainly for railway ballast, road construction material, roofing tiles, and weak soil improvement materials. Fairly rapidly cooled slag is more suited for lightweight concrete aggregates, backfill, and thermal insulation. Rapidly cooled slag is usually in granulated form, and has the highest value of the three types. It can be used in Portland cements, as a raw material for cement clinkers, as a weak fertilizer, in filters, and as a raw material for the ceramics industry (Lee, 1974). Heat recovery is a viable option in the latter two cases.

However, heat recovery from blast furnace slag is a difficult task. The molten slag, when tapped, is highly viscous ($0.3\text{-}2\text{ N/m}^2\text{s}$) and is difficult to handle. Once solid, the thermal conductivity of the material is low, thus hindering energy recovery. As mentioned, rapidly cooled slag is the most valuable, and therefore the most desirable to produce. However, rapid cooling requires high air velocities; this reduces the efficiency of the energy recovery and the quality of heat recovered. Despite the difficulties involved, many technologies have been developed in an attempt to recover the energy stored in slag while simultaneously manufacturing a high value product. These processes are described below.

Broadbent and Warner performed one study of particular interest using a water-glycerol system to simulate the physical properties of blast furnace slag. The premise of their concept was that slag break-up (ie. atomization) could be achieved by a self-



Figure 2.2 Scanning electron micrograph of untreated slag aggregate at 1000X magnification (Lee, 1974).

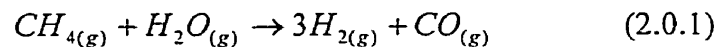


Figure 2.3 Scanning electron micrograph of slag aggregate treated at 1000°C at 3000X magnification. The primary and secondary textures have been coarsened via heat treatment to improve the aggregate value of the slag (Lee, 1974).

impinging jet mechanism without the need for additional gas flow and without appreciable cooling (Broadbent and Warner, 1985). The principles of an impinging jet are shown in Figure 2.4.

A pressurized tank with two 4 mm diameter glass tubes fitted at an angle was used in conjunction with high speed photography to study the effect of process variables on droplet formation and size. The results were extended to trials performed on a blast furnace slag produced from an induction furnace. Jets of slag were established to form a sheet, which subsequently disintegrated completely producing spherical droplets on the order of 3 mm in diameter. The spheres were allowed to fall 1.3 m in a nitrogen atmosphere into a collection bin. More studies were planned to determine parameters relevant to energy recovery.

An imaginative process has been researched in some detail in Japan (Kasai et al, 1997). The system proposes to recover high temperature heat from blast furnace slag using the methane-steam reforming reaction:



which has a reaction enthalpy of 206 kJ/mol. The steam used in the reaction is supplied from the downstream slag granulation process. The sensible heat of the product gases is recovered and used for power generation or steam supply. The gases are subsequently cooled to room temperature, and transported to a destination where the energy can be utilized. Heat is regenerated at this location by the reverse of reaction (2.0.1), which is also known as methanation. Water is removed from the system in a condenser unit and the methane is returned to the site of slag production. A flow sheet of the proposed process is given in Figure 2.5.

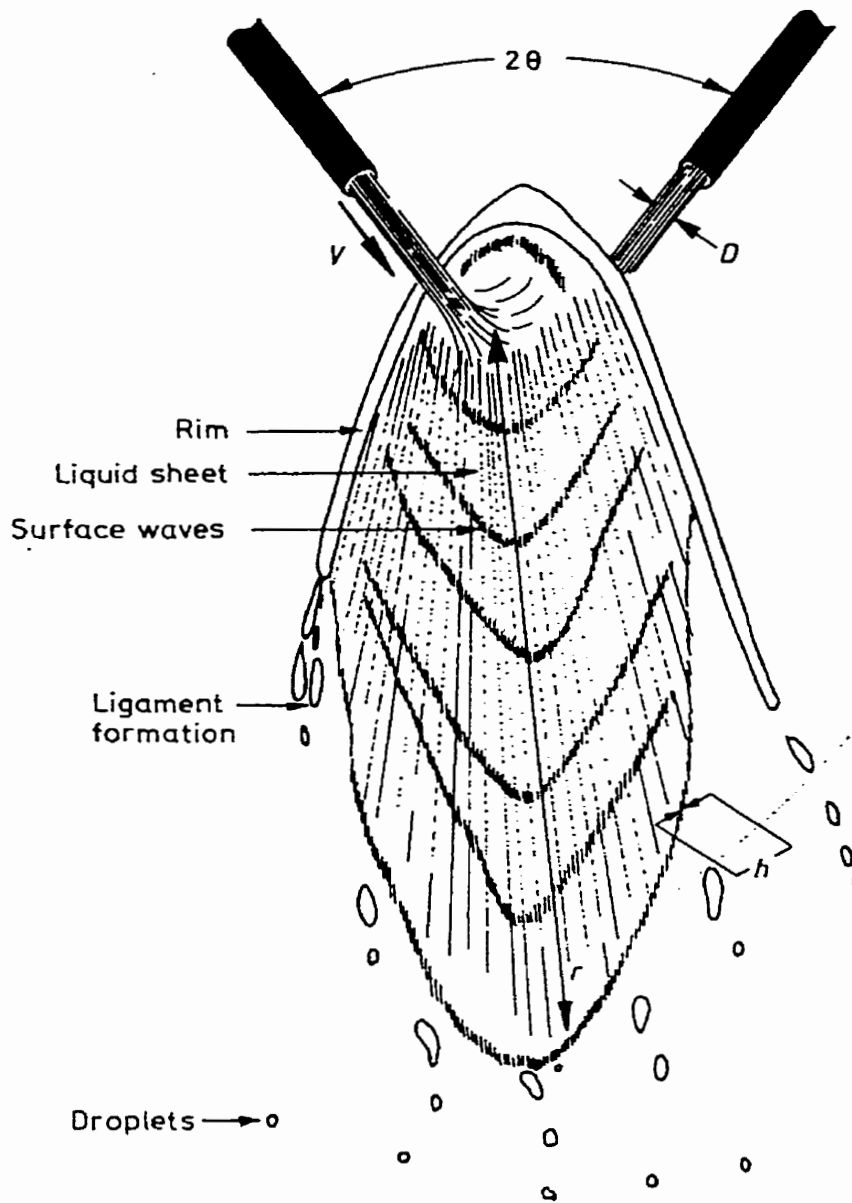


Figure 2.4 Impinging jet atomization (Broadbent and Warner, 1985). (D , jet diameter; h , thickness of sheet; r , radial distance; V , mean velocity; θ , half angle impingement).

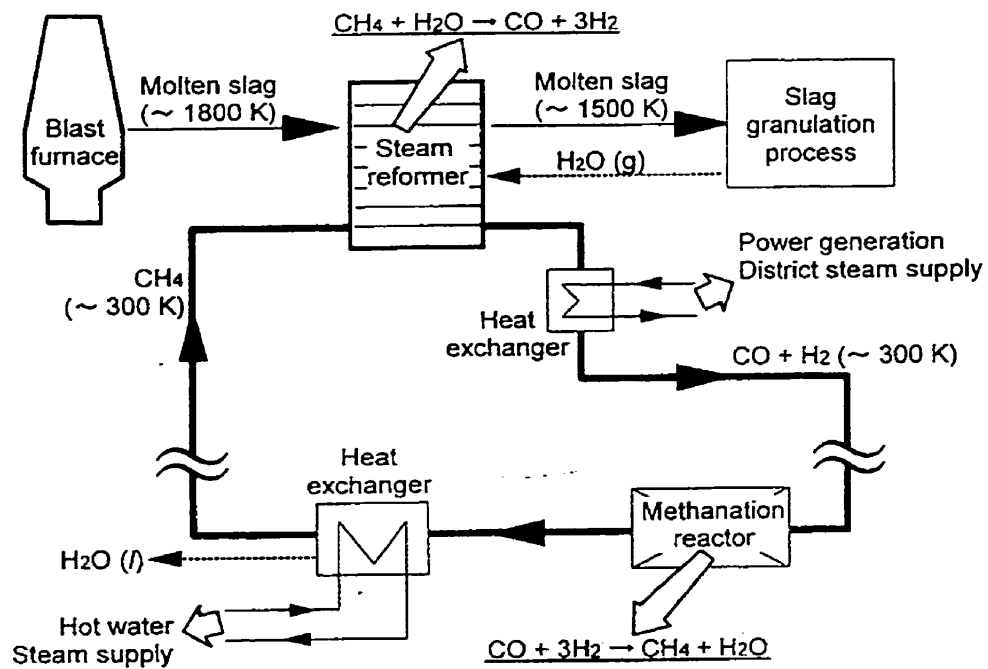
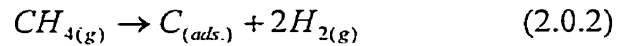


Figure 2.5 Schematic diagram of the methanation-steam reformation process for heat recovery from molten slag (Kasai et al., 1997).

In order to test the concept, a gas supply system complete with a water saturator was linked to a reaction vessel made of fused silica with a 24 mm inside diameter. Slags were inductively heated and a mass spectrometer was used to analyze the inlet and the outlet gas streams. Using the reaction mechanism detailed below, studies were performed to determine the effect of slag composition on reaction rate:



The apparatus used to measure the rates of the reaction is shown in Figure 2.6.

The measured chemical reaction rates were on the order of 10^{-3} to 10^{-1} mol/m²s. The rate of reaction on slag samples containing no sulphur was affected by the concentrations of both CH₄ and H₂O in the feed gas, although the concentration of water was not significant under some experimental conditions.

The reaction rate for slags containing sulphur was smaller, and depended only on the methane concentration. Overall, it can be said that the decomposition of methane is the rate-limiting step for most ranges of sulphur concentrations. The main drawback to this process is the need for a distribution network to carry fuel to the required region, and to transport the recovered methane back to the slag production facility. As well, the problem of granulating the slag and cooling it from approximately 1200 K (the temperature at which the slag would likely exit from the steam reformer) down to room temperature was not discussed.

A number of other Japanese concepts have met with relative success, and have been pursued at the pilot level. In a partnership effort, NKK and Mitsubishi have developed an air granulation plant for converter slag (Bisio, 1997). In this case, slag is

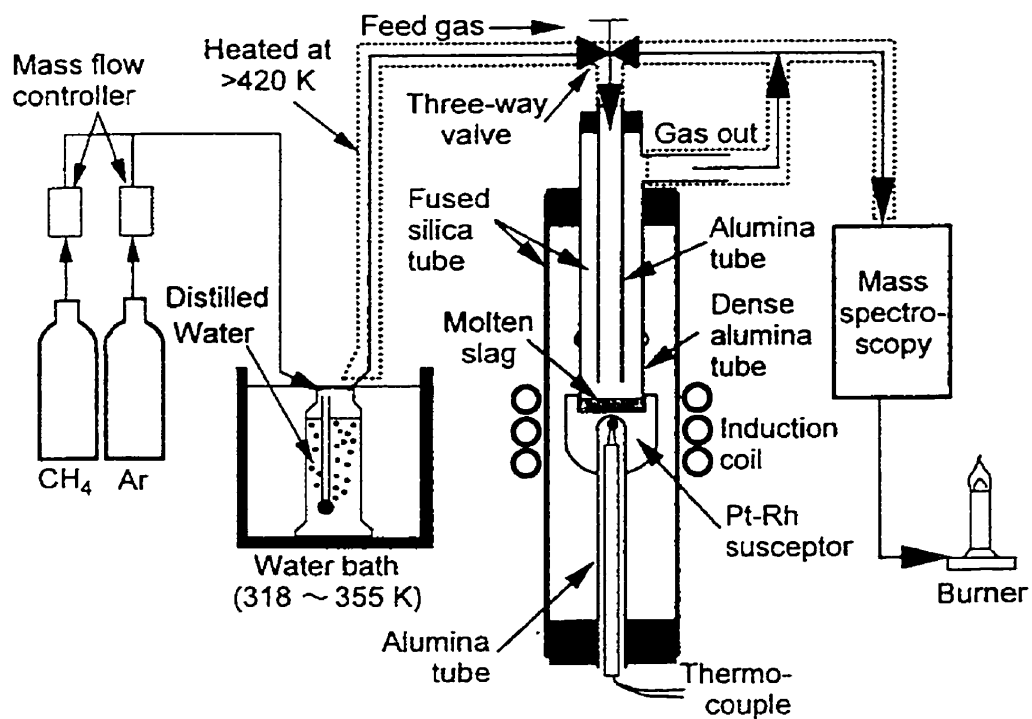


Figure 2.6 Schematic diagram of the experimental apparatus to measure the rate of the $\text{CH}_4\text{-H}_2\text{O}$ reaction (Kasai, et al. 1997).

poured onto a sloped runner, below which is an air blower. As the slag drips off the runner, it is contacted by high velocity air. The slag is subsequently granulated and blown into a boiler, and then transported via a conveyor to storage. In-flight heat transfer occurs due to radiative and convective effects and cools the slag from a feed temperature of approximately 1773K down to 1273K. The boiler cools the slag further, discharging it at an average temperature of 573K; the dominant modes of heat transfer here are conduction and convection. A third opportunity for heat recovery exists in the conveying and storage operations, where air may be heated while further cooling the slag. Energy recovery is in the range of 40-45%. A schematic diagram of the process is shown in Figure 2.7.

A second technology developed by NKK uses drums cooled internally by a low-boiling organic fluid (Bisio, 1997). Slag is poured between the two drums to form a film, which cools quickly on the drum surfaces. A heat exchanger is used to recover the energy from the organic material to produce electricity. One main drawback to this process is that the slag film must be removed from the drums using a stripping tool; failure to do so would result in a dramatic decrease in heat transfer efficiency. The solidified glassy slag layer on the drum is analogous to mineral build-up inside boiler tubes, which is known as fouling. The fouled layer causes significant increases in the resistance of the system to heat transfer. The process is illustrated in Figure 2.8.

Kawasaki Steel, in order to remain competitive in the Japanese market, has developed another heat recovery process. Liquid slag is granulated to particles no larger than 100 mm in a stirrer. Water pipes recover the heat through radiative effects, and the slag is cooled from its feed temperature to 1273K; steam is produced at maximum values

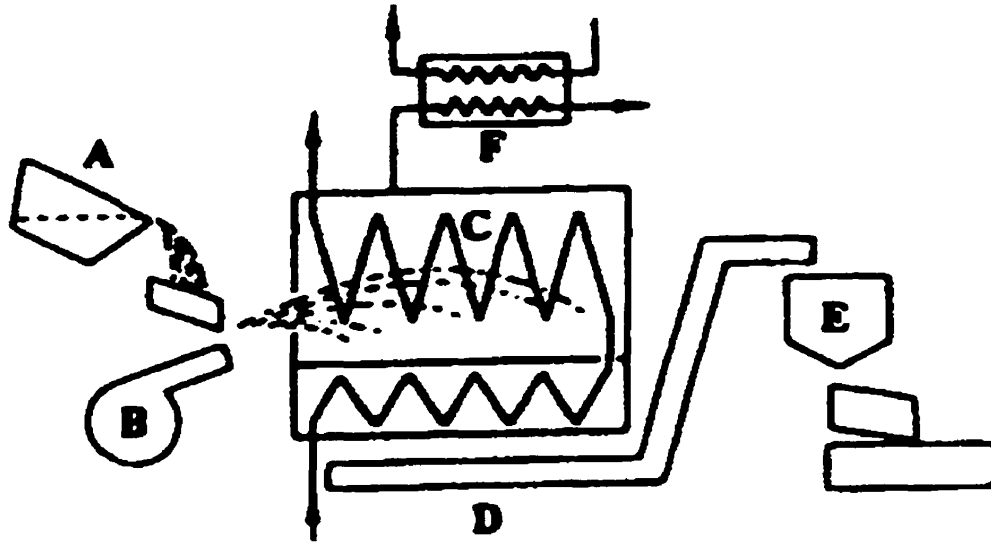


Figure 2.7 Lay-out of the NKK/Mitsubishi air granulation plant (Bisio, 1997.). (A, liquid slag ladle; B, blower; C, hood boiler; D, conveyor; E, slag container; F, dryer).

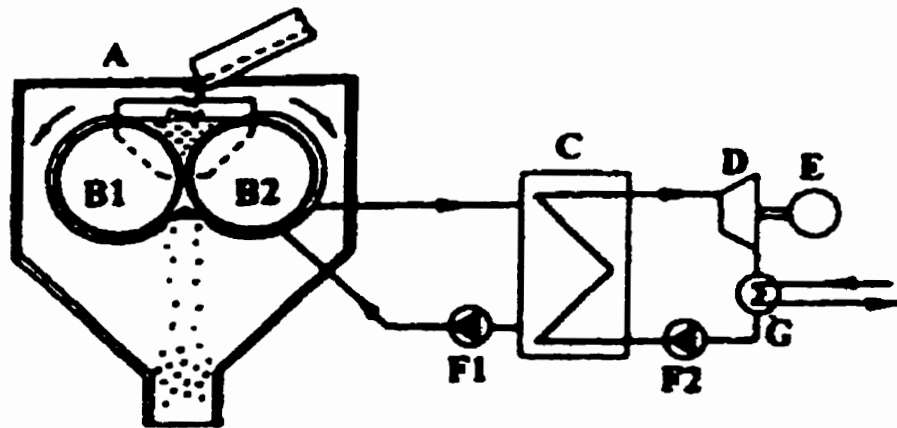


Figure 2.8 Lay-out of the NKK cooling drum process (Bisio, 1997). (A, slag cup; B1 and B2, cooling drums; C, heat exchanger; D, turbine; E, electric generator; F1 and F2, pumps; G, condenser).

of 50 bar and 723K. The granulated slag then falls through a tower where it cools to 523K while the air is heated. The energy recovery is approximately 76%.

A dry granulation process employing fluidized bed technology has been developed by Kvaerner Metals (Featherstone et al., 1998). The technology consists of two distinct operations: the atomization of the slag, and the recovery of heat from the slag granules. Atomization of the molten slag is achieved using a variable-speed rotating cup. Slag is delivered to the centre of the cup from a runner or refractory-lined pipe. When the cup is rotated at a sufficiently high speed, physical forces cause the slag to be ejected from the cup, where it encounters a lip that is designed to enhance atomization. The slag droplets cool as they travel through the air from the cup to the wall of the reactor. In-flight heat transfer ensures that the slag is solid so that the material does not stick to the reactor wall, which is water-cooled. Upon falling to the bottom of the reactor, the granules encounter a modified fluidized bed. The outer portion of the bed is sloped towards the centre of the reactor which contains an annular fluidized section. Cooling occurs in both fluidized sections: the hot air is recovered from the top of the reactor unit and sent to a baghouse for dust removal. In addition, some of the smaller particles in both sections are entrained by the fluidizing air and intercept the molten slag travelling from the atomizing cup to the reactor wall. In this way, the small particles further ensure that sticking of molten material to the wall does not occur, since the small particles are cold relative to the molten material and thus are effective heat sinks. A schematic diagram of the granulation process is given in Figure 2.9.

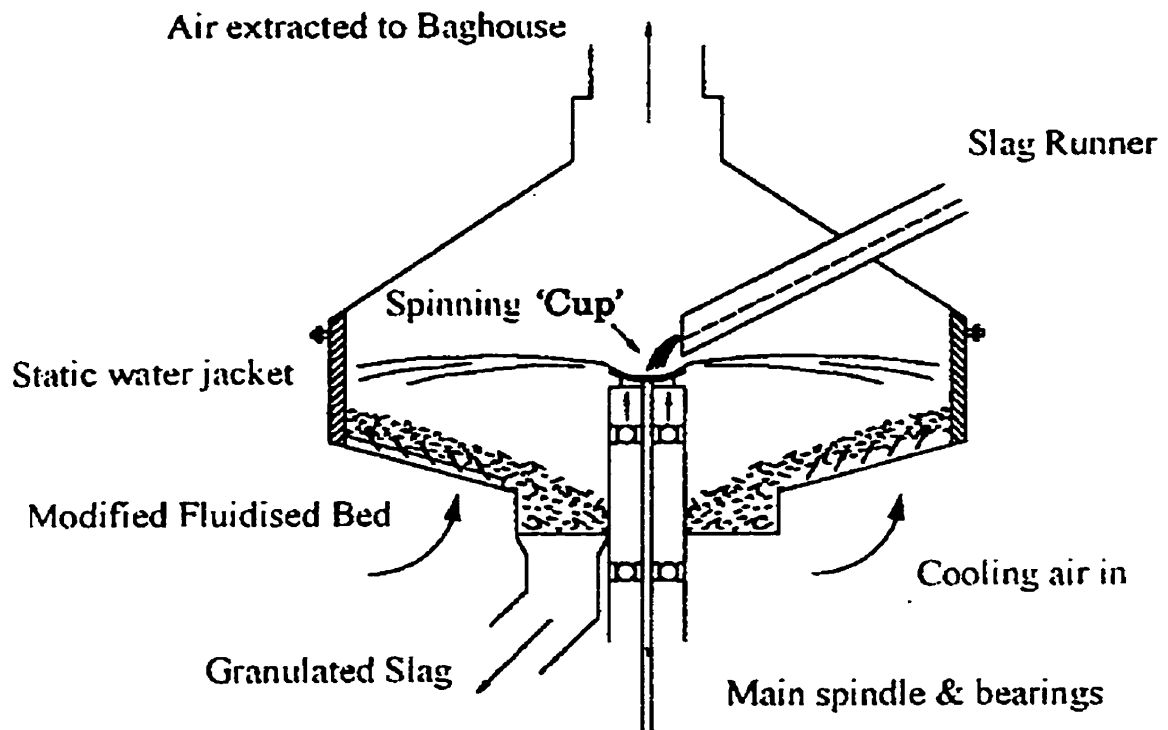


Figure 2.9 Dry slag granulation by Kvaerner Metals (Featherstone, 1998).

The above process was tested at the pilot plant level, and atomizing cups capable of handling molten flowrates up to 6 ton/min at 1823K were developed. The rotational speed of the cup at maximum loading was approximately 1500 rpm. The test facility contained two DC furnaces to supply the slag feed to the cup and the fluidized bed reactor. However, the fluidized bed reactor represented a process bottleneck, requiring downsizing of the atomizing cup from a discharge rate of 6 ton/min to 20 kg/min. Dry granulation of slag has been successfully completed with blast furnace slags, as well as basic oxygen furnace slag, electric arc furnace slag, stainless steel slag, several nonferrous slags, and even one nonferrous matte. Plans currently exist to scale the operation up to a larger pilot plant capable of handling 300 kg/min of molten slag feed. No heat recovery data for this technology was presented.

A British proposal, which has received some interest, is similar to the process described above. Here, the goal is to atomize the molten slag and then cool the particles rapidly to produce a glassy slag (Pickering et al., 1985). The atomization process used is similar to that already described: it operates by spinning out a thin film of slag, which extends radially from the cup lip. As the film extends beyond the lip, atomization of the slag occurs. This atomization process has one added feature: the presence of an annular air jet, which assists in the break-up of particles by inducing unstable waves in the film. The main effect of the air blast is to produce particles with a smaller size distribution, as well as to deflect the particles slightly upwards to produce a cone-shaped spray. In-depth studies have been performed to determine the mean diameter and spray trajectory of the molten material as a function of the process variables including:

- Cup diameter;
- Cup speed;

- Slag flowrate;
- Air blast flowrate;
- Air blast velocity;
- Slag Reynolds number;
- Pressure, velocity, momentum, and mass ratios of molten slag to air.

The atomizing equipment is illustrated in Figure 2.10.

Heat is recovered via four distinct mechanisms. As the atomized molten material travels from the cup to the reactor wall, heat is lost by convection to the air passing up from below the fluidized bed through to the stack above. Also, heat is transferred through radiative effects to the reactor wall. The molten material experiences a temperature drop of approximately 100K to 200K in the atomization and flying stages, which represents nearly 15% of the total heat recovery. The second stage of heat transfer involves impacting the particles on the reactor wall. The wall is kept cool (presumably by a water jacket) to prevent sticking, and the molten material decreases in temperature by approximately the same amount as the first stage. Almost one-quarter of the total heat recovered is transferred in this step. As the semi-cooled slag particles fall from the wall, they enter the primary fluidized bed. Heat is extracted from the fluidized particles by fluidizing air or additionally by immersed boiler tubes. Heat recovery in the primary fluidized bed is 43% of the total. As the primary fluidized beds grow, particles begin to overflow the bed and feed into the secondary fluidized bed. The heat recovery in this section represents 20% of the total heat recovered in the operation. The heat recovery equipment and atomizing granulator are shown in Figure 2.11.

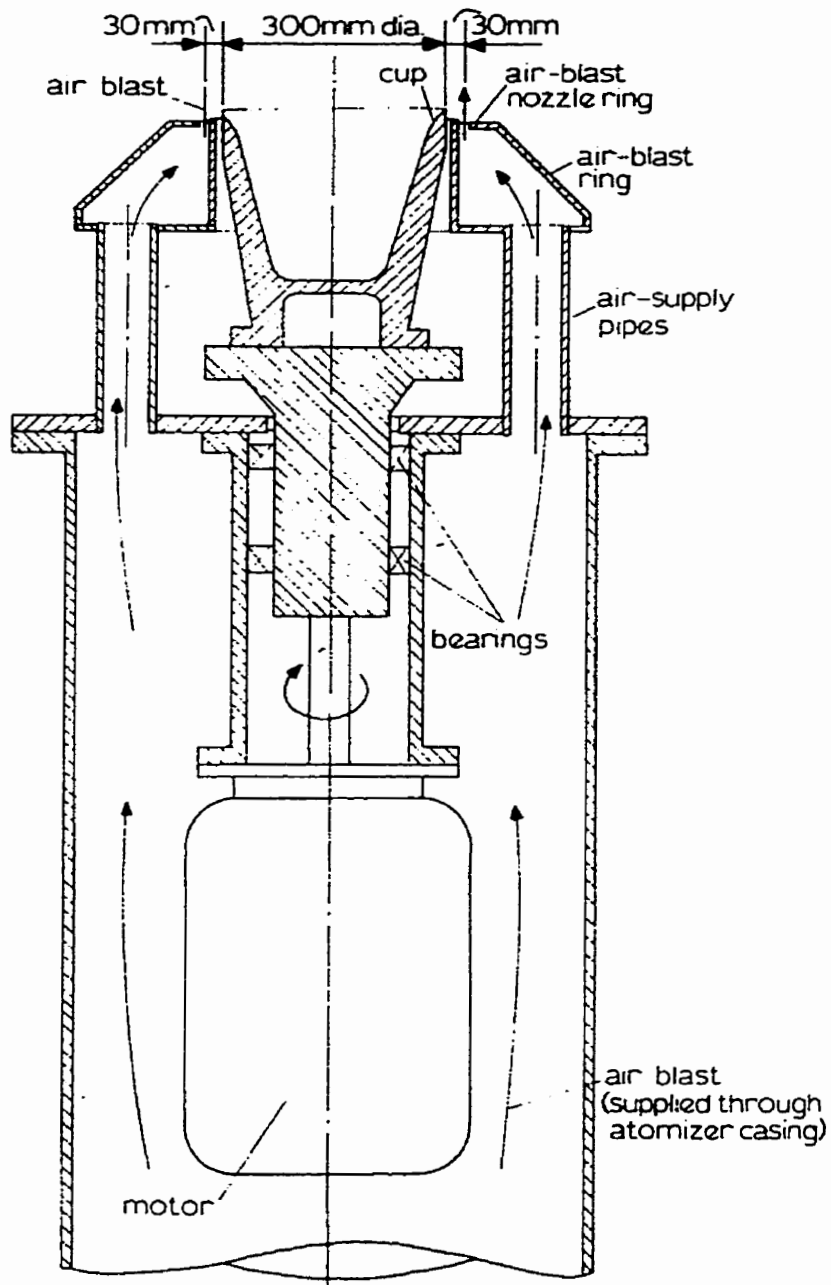


Figure 2.10 Rotary-cup, air-blast atomizer (Pickering, 1985).

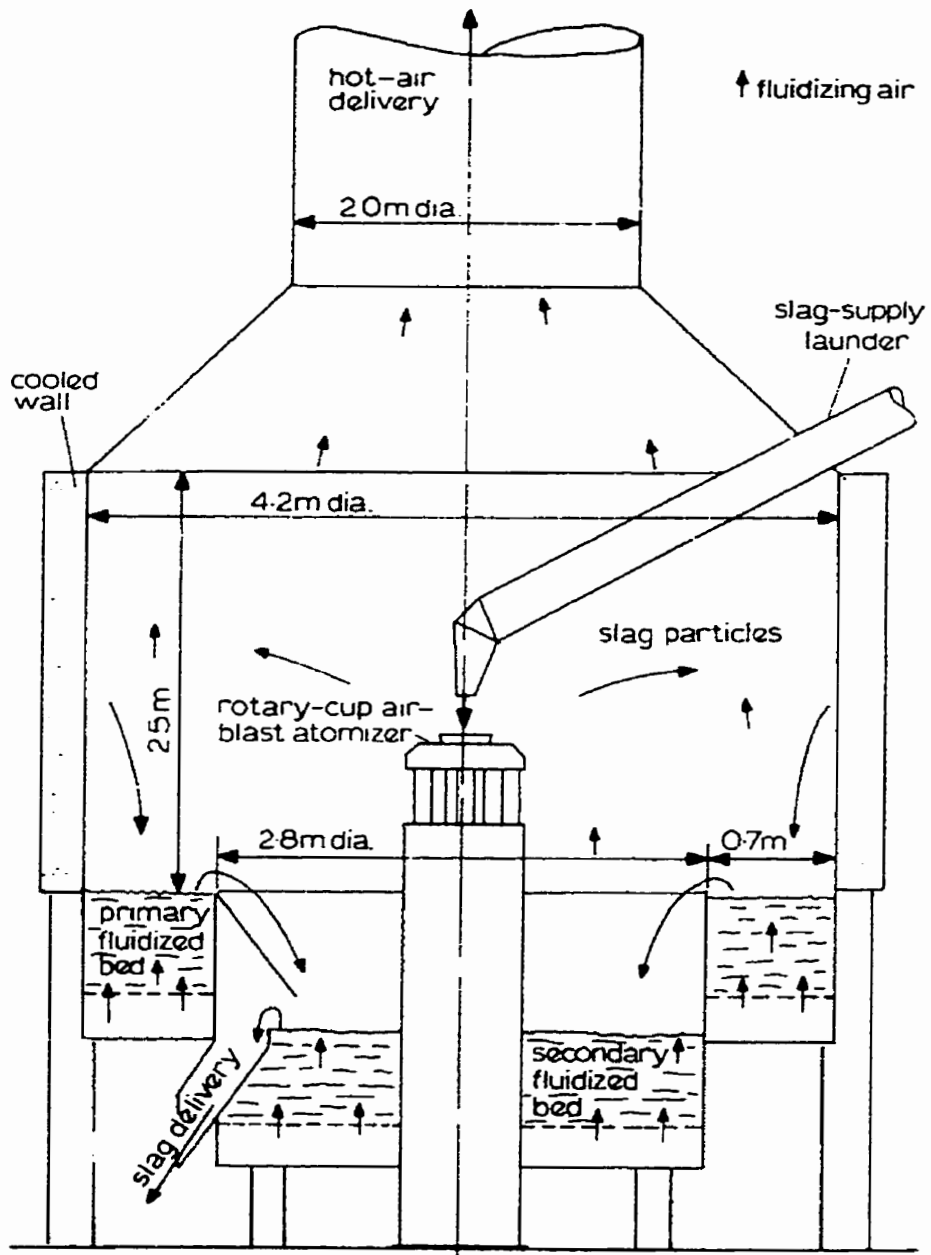


Figure 2.11 Molten slag granulation and fluid bed heat recovery plant (Pickering, 1985).

The authors did not discuss process specifics. However, slag particles with a mean diameter of 2 mm were said to be produced by the atomizer, so the final product, which was reported to have greater than 95% glassy content, would likely be in the range of 3-5 mm. The atomizer operated in the range of 500-1500 rpm and had a diameter of 100 mm. Slag flowrates of 0.2-0.5 kg/s were used to feed the atomizer with air blast flowrates on the order of 1 kg/s corresponding to velocities of approximately 120 m/s. Scale-up figures were given for the fluidized beds, although no detailed analysis was available.

A heat recovery scheme designed by German Kawasaki (Schmidt, 1998) is shown in Figure 2.12, and operates as follows. Molten slag is transferred to the heat recovery plant in a transfer car at a temperature of 1573 to 1773K. The slag is poured into an insulated container and stirred mechanically. The slag mixture is stirred intensely in the insulated container while it cools slowly to a temperature of 1273 to 1373K via radiative heat losses. The insulated vessel slides and dumps granules of 100 mm diameter at 1273K into the skip hoist. The granules are dumped from the skip into the top of an expanded bed cooling shaft, which transfers heat from the granules to the air blown into the bed via the fan. Cooled granules are discharged through the bottom of the bed, and the hot air passes through a cyclone to remove and recirculate slag fines. Hot air at 1123K is fed to a downdraft boiler, which produces steam at 503K and 20 bar.

The capacity of the heat recovery plant is 40 ton/hr, and is capable of producing 16.5 ton/hr of steam at 503K and 20 bar. The overall conversion of heat is 0.37 tons of steam per ton of slag, with 80% of the heat recovered in the cooling bed, and 20% of the

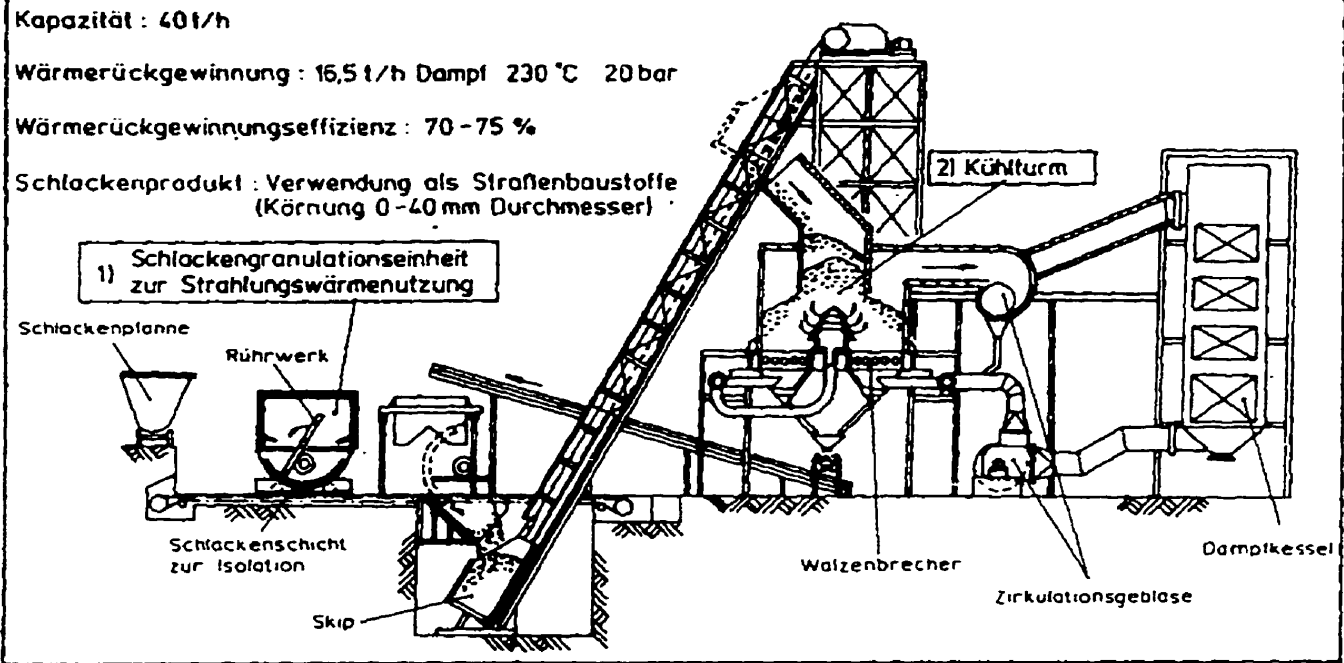


Figure 2.12 Heat recovery from molten blast furnace slag to produce steam (Schmidt, 1998).
 (Schlackenplanne=transfer car; Schlackenschicht zur Isolation=insulated container;
 Ruhrwerk=mechanical stirrer; Walzenbrecher=expanded bed cooling shaft;
 Zirkulationsgebläse=fan; Dampfkessel=down-draft boiler)

heat recovered in a water-cooled slag product collection bin. All the slag product is granular with a size less than 40 mm, and the overall thermal efficiency of the unit is 70-75%.

Overall, recovering heat from molten blast furnace slag is difficult. Each of the processes described above has advantages as well as drawbacks. Some concepts have been tested at the pilot scale, but none have been employed industrially. New processes are needed to fulfill heat recovery requirements at the industrial level while yielding a high value slag product.

3.0 Theory

Fluidization is the operation by which solid particles are transformed into a fluid-like state through suspension in a gas or liquid. In this study, solid glass beads will be fluidized by air. Then, molten slag or salt droplets will be fed onto the top of the bed thereby coating the solid bed particles and causing their diameters to increase. Since heat transfer in fluidized beds is excellent, then this will greatly aid in the heat recovery process.

3.1 Fluid Mechanics

Fluidization of bed particles results from the frictional force exerted on the particle by the air. At the point where this force just equals the gravitational force acting on the particles, the pressure drop across a given section of bed is equivalent to the weight of the air and the particles in the same section. In this case, the bed is incipiently fluidized. As the velocity of the fluid is increased, the bed expands slightly from the minimum fluidized height, and gas channeling and bubbling is observed. If the velocity of the fluid is increased sufficiently, the bed particles will become entrained in the air stream and carried out of the bed. This is known as pneumatic transport, and the air velocity at which it occurs corresponds roughly to the terminal velocity of the bed particles.

As the air velocity is increased, the pressure drop across the bed will vary. For example, the pressure drop across the bed will be approximately proportional to the air velocity until the minimum fluidization velocity is reached. When the minimum fluidization velocity is reached, the physical forces described are such that the bed becomes fluidized, and the voidage between the particles allows the pressure drop to

decrease. Further increases in air velocity have little effect on pressure drop. However, when the air velocity is subsequently decreased, an operational hysteresis is observed. When the velocity is decreased in the region just above that of incipient fluidization, frictional forces do not have to be overcome. In this way the pressure drop across the bed is lower when approaching the limit of the minimum fluidization velocity from the right as compared to the left, as shown in Figure 3.1

Determination of the minimum fluidization velocity is important for proper and predictable fluidized operation of the bed, and many predictive correlations are available. In the early stages of experimentation, the minimum fluidization velocity was observed for a number of conditions. Using these data, different correlations from the literature (Davidson et al., 1985) were employed in an attempt to find one suitable to the experimental situations encountered in this project. The correlations provided by these sources were unable to accurately predict the minimum fluidization velocity observed. A mathematical expression was finally found to be accurate and is given below (Davidson,1985.):

$$u_{mf} = \frac{\mu_f}{\rho_f d_M} \left((33.7^2 + 0.0408 Ga Mv)^{0.5} - 33.7 \right) \quad (3.1.1)$$

where

$$Ga = \frac{d_M^3 \rho_f^2 g}{\mu_f^2} \quad (3.1.2)$$

$$Mv = \frac{\rho_M - \rho_f}{\rho_f} \quad (3.1.3)$$

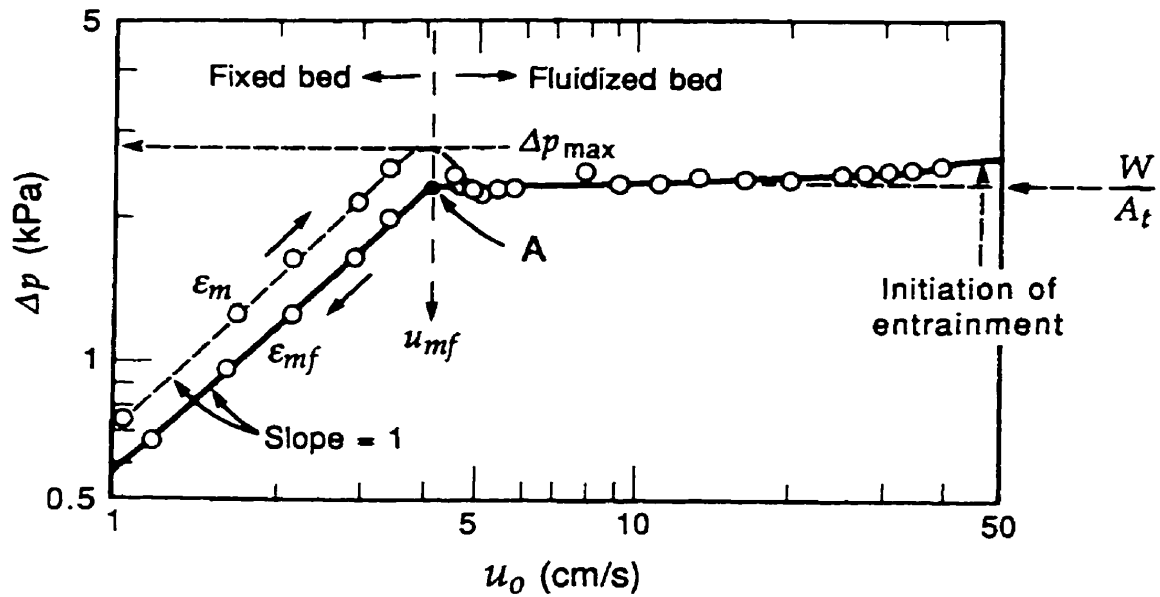


Figure 3.1 Pressure drop versus velocity for a fluidized bed of sand (Kunii and Levenspiel, 1991). As the velocity is increased, the pressure drop across the bed increases linearly until the minimum fluidization velocity (u_{mf}) is reached. At this point the volume of space between the bed particles increases from ϵ_m to ϵ_{mf} , which is the point at which the bed "unlocks" and becomes incipiently fluidized. The ratio W/A_t is the mass of solids per unit of cross-sectional bed area, and has little significance to this discussion.

Equation (3.1.1) was derived for mixtures, and the parameters are defined by the following equations.

$$d_M = \frac{R_0}{R_1} d^P d^F \quad (3.1.4)$$

$$\rho_M = \frac{x_F}{\rho_P^F} + \frac{(1-x^F)}{\rho_P^P} \quad (3.1.5)$$

$$R_0 = (1-x^F) \rho_P^F + x^F \rho_P^P \quad (3.1.6)$$

$$R_1 = (1-x^F) \rho_P^F d^F + x^F \rho_P^P d^P \quad (3.1.7)$$

However, in the case of a pure material the mole fraction term x^F is unity, and Equations (3.1.1) through (3.1.3) become functions of the particle diameter d_p rather than the weighted average particle diameter d_M , and therefore Equations (3.1.4) through (3.1.7) become unnecessary. This modified form of Equation (3.1.1) was used by Wen and Yu (Davidson, 1985), and is recommended for coarse particle systems (particle diameter > 1mm).

The above discussion assumes that the fluidizing medium is air. If the fluidizing medium is a liquid, then the description of fluidization phenomenon would be somewhat different. The same argument holds for different types of bed particles. In order to predict the type of fluidization that will occur with different particles, a descriptive scheme has been developed, which is known as the Geldart Classification of Particles. The classification system is outlined graphically in Figure 3.2.

Two types of particles were examined in this study: the bed material used for experimentation was comprised of Type A particles, whereas slag particles would likely border between Type B and Type D.

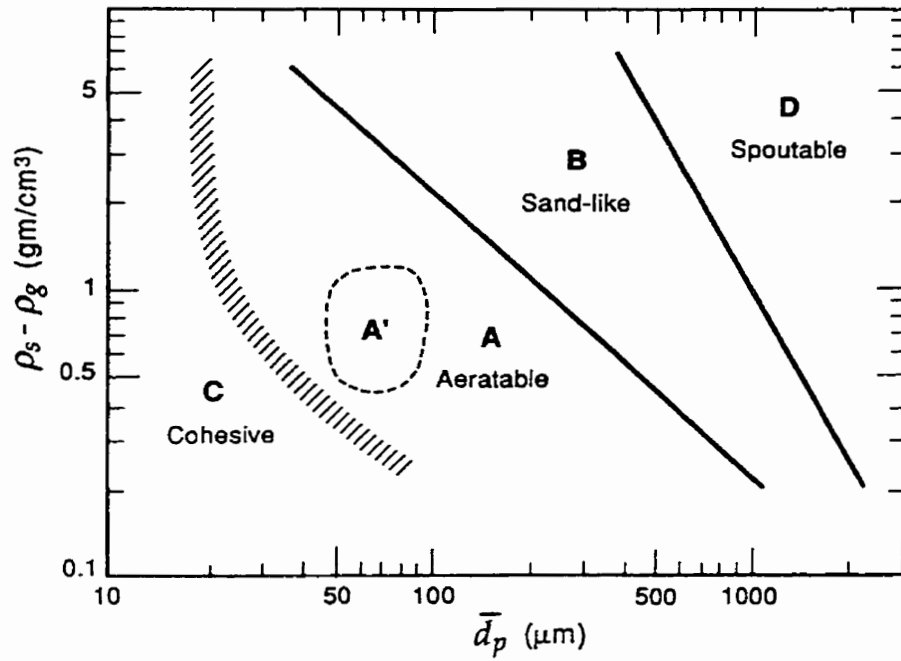


Figure 3.2 The Geldart classification of particles for air at ambient condition (Kunii and Levenspiel, 1991). The fluidization behaviour of different particle types are classified according to densities and the size ranges of the particles.

Type A particles allow for considerable bed expansion prior to the appearance of bubbles. Once in the bubbling regime, the bubbles of gas rise much more quickly than the rest of the gas, which allows for gross circulation of solids even when only a few bubbles are present within the bed. Overall, excellent heat and mass transfer characteristics are observed in beds of this nature.

Beds composed of Type B particles form bubbles of gas as soon as the gas velocity exceeds the minimum fluidization velocity. The bubble size increases linearly as the velocity is increased beyond the minimum fluidization velocity, although the bubble size is independent of the particle size in the bed. Bubbling is the main mechanism for mixing and circulation. The majority of metallurgical fluidized beds operate within this regime. Beds made of Geldart Type D particles allow bubbles to coalesce leading to spouting. Spouting is common in agglomeration applications where large particle sizes are unavoidable. In a spouted bed, a high velocity spout of gas punches through the bed of solids, thereby transporting particles to the top of the bed. The rest of the solids move downward slowly around the spout and through gently upward-percolating gas (Kunii and Levenspiel, 1991). However, regardless of classification, when no internal equipment is present in a bed of coarse particles, bubbles can grow quite large (Davidson et al., 1985).

Overall, the study of fluid mechanics in fluidized beds is extensive. Research on coarse particle systems includes slugging behaviour, bed expansion characteristics, the effect of internal structures, gas flow and mixing, and solids circulation. Slugging can be present in a variety of forms in the bed. For larger Geldart D particles, the bed separates into slices of emulsions separated by the gas. The slices of gas and emulsions rise up in the bed, matched by a continuous raining of solids from slice to slice. Eventually the

topmost slice disappears, being unreplenished with raining solids; new slices and slugs simultaneously form at the bottom of the bed. This pattern is especially common in a tall and narrow fluidized bed (Kunii and Levenspiel, 1991), and the slugs produced tend to be flat. A detailed analysis of fluid flow in the fluidized bed is not within the scope of this study, and so the remainder of the discussion on fluidized bed theory will focus on heat transfer. Specific emphasis will be placed on the mathematical model used to predict heat transfer coefficients for the experimental system.

3.2 Model Description

The fluidized bed apparatus is primarily comprised of two sections: the reactor freeboard region into which molten droplets are fed, and the fluidized bed region where the bulk of the heat recovery occurs. Modeling of the heat transfer was thus conveniently divided into these two discrete regions. Furthermore, three separate heat transfer coefficients were important in this study. The first involved the transfer of heat from a falling molten droplet to the passing air stream. The second coefficient related the heat given up by the droplet entering the reactor to the fluid bed, while the third gave an indication of heat losses from the bed to the reactor wall and the internal equipment.

3.2.1 Heat Transfer from a Falling Molten Droplet

In the reactor freeboard region, air exiting the fluidized bed passes by molten drops of material (either salt or slag) of a diameter determined by the aperture size in the bottom of the heated holding vessel. The molten material falls with a characteristic velocity, which allows for calculation of the Reynolds number of the droplet via:

$$\text{Re} = \frac{\rho_A D_D v_{A \rightarrow D}}{\mu_A} \quad (3.2.1)$$

where the velocity is the relative velocity between the air and the falling droplet, the subscript A refers to the parameters of the air, and the subscript D refers to the parameters of the molten droplet. The following correlation for falling droplets may be applied to solve for the Nusselt number (Incropera and DeWitt, 1996; Kunii and Levenspiel, 1991):

$$\overline{Nu} = 2 + 0.6 Re_D^{1/2} Pr_A^{1/3} \quad (3.2.2)$$

Then the convective heat transfer coefficient can easily be determined using Equation (3.2.3).

$$\overline{h}_D = \frac{k_A \overline{Nu}}{D_D} \quad (3.2.3)$$

The bar notation in the preceding two equations indicates that the parameters are evaluated at the approximate temperature of the surroundings (in this case, the passing air stream). A heat balance may then be performed on the freeboard region, and assuming negligible heat loss to the surroundings, the balance takes the form of Equation (3.2.4).

$$\dot{m}_A c_p (T_{A,exhaust} - T_{bed}) = h_D \dot{N}_{drops} A_D t_{fall} \left(\frac{T_{S,m} + T_{S,bed}}{2} - T_{A,exhaust} \right) \quad (3.2.4)$$

where T_{bed} is assumed to be equal to that of the air exiting the bed (but not the temperature of the air exiting the reactor);

\dot{N}_{drops} is the flowrate of the molten droplets;

t_{fall} is the free-fall time experienced by the droplet as estimated by Equation (3.2.5) below;

$T_{S,bed}$ is the temperature of the droplet as it completes the free-fall and enters the fluidized region of the reactor. This temperature is estimated via Equation (3.2.6).

The free-fall time is calculated using a basic physical kinetics equation, which ignores the effect of drag coefficients and other aerodynamic considerations:

$$t_{fall} = \sqrt{\frac{2d_{fall}}{g}} \quad (3.2.5)$$

The estimation of the free-fall time allows for the determination of the droplet temperature as it enters the fluidized region (Incropera and DeWitt, 1996):

$$T_{S,bed} = \left(\frac{T_{S,m} - T_{\infty}}{\exp\left(\frac{h_D A_D}{\rho_D V_D c_p} t_{fall}\right)} \right) + T_{\infty} \quad (3.2.6)$$

Equation (3.2.6) is based on the lumped capacitance model, which assumes a negligible temperature gradient within the surface through which heat is transferred. Thus, convective heat transfer is assumed the rate-limiting step. The quantitative measure to ensure that this condition is met, and that Equation (3.2.6) is valid, is the dimensionless Biot number as shown below:

$$Bi = \frac{h_D V_D}{k_D A_D} \quad (3.2.7)$$

Therefore, Equation (3.2.7) is the ratio of the convective to the conductive heat transfers, and for $Bi \ll 0.1$, Equation (3.2.6) holds true. If the condition is not met, a more detailed analysis may be performed using the general transport equation.

3.2.3 Gas to Particle Heat Transfer

For a known $T_{S,bed}$, a heat balance may be performed for the fluidized region of the reactor. This calculation requires the determination of a second convective heat transfer coefficient; this will determine the heat transferred from the bed particles to the fluidizing air. The correlation used for the heat transfer coefficient of the bed is given below (Kunii and Levenspiel, 1991).

$$Nu_{Bed} = \frac{h_{Bed} D_P}{k_A} = 0.03 Re_p^{1.3} \quad (3.2.8)$$

In this case, the subscript P refers to the parameters of the bed particles.

The heat transfer system relating heat transferred from the molten particle to the bed particles (and hence the fluidizing air) can be viewed as one involving primarily hot solids and cold gases. This analysis relies heavily on the assumption that the molten droplet cools extremely quickly upon entering the bed and efficiently gives up its latent and sensible heat to passing air as well as other bed particles that are encountered. This assumption is an excellent one to make, if one considers the following two points.

1. If the molten material did not cool extremely quickly, the hot droplet would encounter a number of cold bed particles, which would agglomerate upon the eventual freezing of the hot feed. This would stop bed operation almost immediately via defluidization (This phenomenon will be discussed in detail later).
2. Previous research indicates that there is a large discrepancy between the overall bed coefficient given in Equation (3.2.8), and a single particle coefficient describing local heat transfer between an individual particle and a passing air stream (Kunii and Levenspiel, 1991). The overall coefficient should be used if the air stream is to be heated or cooled to the temperature of the bed. In this case, assumptions regarding

the pattern of air flow through the bed become very important and strongly govern the conclusions of the analysis. A local coefficient should be used in cases involving a particle of a given temperature being fed to a bed of similar particles at a much different temperature. At low Reynolds numbers, h_{bed} can be as much as three orders of magnitude lower than $h_{particle}$. In the present research, it is estimated that if the bed heat transfer coefficient correlation had been used, then the predicted heat transfer coefficient would have been 2.5-3.5 times lower. The deviation is enough to result in erroneous predictions of system temperatures and heat transfer in the bed.

In an in-depth review of heat transfer in fluidized beds, Davidson concluded that if a conduction-dispersion model were used to interpret the heat transfer measurements, Nusselt numbers of the correct order of magnitude could be obtained at low Reynolds numbers. More recent work on the problem, as discussed by Davidson, indicates that axial conduction within the bed is significant and has been for the most part ignored in previous works. The details of the analysis are not important here, but it was concluded that low values of the gas-particle Nusselt number for $Re_p < 100$ were due to the fact that axial conduction had been neglected. Experimental work performed in this study lies within this regime of Reynolds numbers, and thus these conclusions were extremely important in estimating the correct gas-particle heat transfer coefficient for use in the model. In the end, the correlation used was summarized by Davidson and developed by Wakao (Davidson, 1985; Wakao et al., 1979), and was of the form:

$$Nu_{gp} = 2 + 1.1 Re_p^{0.6} Pr^{1/3} \quad (3.2.9)$$

with the only limitation that $Re_p > 15$. Equation (3.2.9) is well within the suggested range of estimation of Kunii and Levenspiel, who expected the Nusselt number to be described by the following equation

$$Nu_{gp} \cong 2 + (0.6 - 1.8) Re_p^{1/2} Pr^{1/3} \quad (3.2.10)$$

For a known bed heat transfer coefficient, a heat balance can be written for the bed region:

$$\dot{m}_S c_p (T_{S,bed} - T_{bed}) + \dot{m}_S \Delta H_{fusion} = h_{gp} A_{eff,bed} (T_{Bed} - T_{A,in}) + losses \quad (3.2.11)$$

Two assumptions are implicit to this balance:

1. Although the salt droplet enters the bed at a temperature much higher than that of the bed, it cools quickly, and transfers all the heat to the bed;
2. The reactor wall temperature is such that negligible heat losses are encountered from the bed to the wall.

The calculation of the effective bed area, $A_{eff,bed}$ presented some difficulty. The minimum area available to heat transfer can be assumed to be the cross-sectional area of the bed. The maximum area available to heat transfer can be assumed to be the surface area of a bed particle multiplied by the approximate number of particles present in the bed. It is unlikely that either case is realistic: the small area provided by the minimal estimation does not account for the presence or the number of bed particles; the maximum area would never be encountered by a single gas particle moving through the bed. Information regarding calculation of effective bed areas is lacking, and so an indirect approach to calculating this value was taken. In the computer algorithm, the maximum effective bed area was calculated based on system parameters. The effective

bed area used by the algorithm was a multiple of the maximum value, within bounds set by the user. The value used was typically 10% of the theoretical maximum value.

In addition to the difficulty of selecting the correct correlation, problems arise when it is desired to measure system temperatures in order to validate the heat transfer coefficient prediction. The main obstacle to measuring the relevant thermal driving force is the relatively large surface area present within the bed and the rapid approach to equilibrium between the low heat capacity gas and the bed of particles (Botterill, 1985). As well, it is difficult to determine whether it is the particle or bed temperature which is being measured by a thermocouple inserted into the bed, although altering the system configuration can provide some insight. Also, a thermocouple inserted into the fluidized region will undoubtedly interfere with the free movement of particles through the bed, which in turn will affect the temperature distribution within the bed.

The consequence of this discussion is that if the temperature within the bed is measured incorrectly, a gas-particle heat transfer coefficient which is calculated based on these measurements will certainly have a degree of error associated with it. Furthermore, this coefficient is to be compared to that already calculated using the above correlations, which have an associated error. Therefore, a comparison of the calculated and the observed gas-particle heat transfer coefficients is difficult to make due to the inherent problems associated with the processes involved in evaluating each quantity.

A second heat balance which does not rely on heat transfer coefficients was performed on the bed, and is shown below.

$$\dot{m}_S c_p (T_{S,Bed} - T_{Bed}) + \dot{m}_S \Delta H_{fusion} = \dot{m}_A c_p (T_{Bed} - T_{A,in}) + losses \quad (3.2.12)$$

The loss terms in Equations (3.2.11) and (3.2.12) are explained below in Section 3.2.4, and the significance of these equations is discussed in Section 3.2.4.

3.2.4 Bed to Wall Heat Transfer

As mentioned, three heat transfer coefficients are important in the system analyzed in this work, although only two are important to fluid bed operation. The first coefficient of importance and its intrinsic properties were discussed above. The second coefficient describes the heat losses from the fluid bed to the surroundings via convection.

The convective heat transfer between a fluidized bed and an immersed surface involves two components:

1. The particle convective component, h_{pc} which describes heat transfer to the random motion of particles throughout the bed;
2. The gas convective component, h_{gc} , which allows for heat transfer to occur from the bed to the gas and to the gas bubbles.

The theory behind the particle convective component is somewhat complex, and its evaluation requires a number of physical parameters of the system that were not available and that could not be readily measured. As well, for heat transfer to vertical surfaces, heat transfer to the gas percolating through the particulate phase and to gas bubbles becomes significant in beds of large particles when particles greater than 3 mm are fluidized (Davidson, 1974). Since the initial size of the bed material was 1 mm, and considerable growth of the particles was expected, then the assumption was made that the majority of system losses could be quantified using the gas convective component, h_{gc} . The correlation selected has been suggested by Davidson and is of the form (Davidson, 1985):

$$Nu_{gc} = 0.009 Ar^{1/2} Pr^{1/3} \quad (3.2.13)$$

Although Equation (3.2.13) has been shown to give good agreement with experimental values, it has the drawback of not accounting for surface size or shape. In this way, the selection of this correlation is somewhat inappropriate since the geometry of the reactor wall is markedly different from that of the thermocouple sheath inserted into the bed. Nevertheless, after an exhaustive literature search, it was felt that Equation (3.2.13) would best represent the actual heat losses of the system. In Equations (3.2.11) and (3.2.12), the loss terms are identical, and are solved for using the following equations:

The total area of losses is determined by:

$$A_{losses} = A_{int,ernals} + A_{surf,reactor} \quad (3.2.14)$$

where the heat loss term is quantified below:

$$Q_{losses} = h_{losses} A_{losses} (T_{bed} - T_{wall}) \quad (3.2.15)$$

and h_{losses} is determined from the solution of Equation (3.2.13). The wall temperature was assumed to be equal to that of the incoming gas.

3.2.5 Normal Model Operation

A routine was programmed using the Solver utility in Excel, which varied T_{Bed} , $T_{A,exhaust}$, $A_{eff,bed}^*$ (via a correction factor and $A_{eff,bed}$) in order to satisfy the heat balances in Equations (3.2.4), (3.2.11), and (3.2.12). Constraints were placed on the correction factors to ensure that the final parameters were within the appropriate ranges, as discussed above. Finally, an overall heat balance was performed on the reactor as a check:

$$\dot{m}_S c_p (T_{S,in} - T_{Bed}) + \dot{m}_S \Delta H_{fusion} = \dot{m}_A c_p (T_{A,exhaust} - T_{A,in}) \quad (3.2.16)$$

Solution sets typically converge so that the heat balances are accurate to $\pm 5\%$. This normal operation of the model was used to predict the heat transfer coefficients and both the bed and exhaust temperatures for steady-state operation of the fluidized bed system. The deviations between actual and predicted temperatures are examined in Section 5.1. Unfortunately, no equipment exists that allows for the direct measurement of the actual heat transfer coefficients in a system. Instead, measured temperatures had to be used in conjunction with the procedure outlined below.

3.2.6 Reverse Model Operation

The procedure outlined below describes how the actual heat transfer coefficient of the observed system was back-calculated using experimentally obtained values. Since the original model detailed the method of calculating the predicted heat transfer coefficient based on temperatures determined simultaneously to satisfy thermal balances, then it seems fitting that the discussion below be considered a reverse operation of the model previously described.

The heat transfer coefficient of prime importance in all the experiments was that of gas to particle heat transfer, h_{gp} . Also important was the heat lost to the surroundings via convection to the internals and the reactor wall. Therefore, the governing equation to be examined is logically the heat balance described in Equation (3.2.11), which can be rearranged to the form shown below:

$$h_{gc,actual} = \frac{\dot{m}_s^E (c_{p,s} (T_{s,b}^M - T_{bed}^E) + \Delta H_{f,s}) - losses^{M,E}}{A_{bed}^M (T_{bed}^E - T_{Air,m}^E)} \quad (3.2.17)$$

The superscript on a given term denotes the source of the value used in the back-calculation of h_{gc} i.e. the experimental or the model. Furthermore, Chapter 5 refers to a gas to particle heat transfer coefficient in the bed, which is the same as the gas convective

coefficient, h_{gc} , used here. The change in moniker is for convenience only: to remind the reader of the specific nature and the direction of heat transfer occurring in the bed.

In order for Equation (3.2.17) to yield a value that closely represents the actual heat transfer coefficient in the fluidized bed, it is desirable to use as many experimentally derived quantities as possible. All non-constant parameters were given experimental values with the exception of the temperature of the salt entering the bed, the area of the bed, and the heat loss term. The temperature of the salt entering the bed, $T_{s,b}$ was assigned the value predicted for it by the Excel model. The reason for this was twofold:

1. The actual temperature of a molten droplet is very difficult to measure, especially if the goal is to allow it to fall freely without impedance from a thermocouple or other temperature-measuring device;
2. The temperature at which the salt entered the bed was always only slightly less than the feed temperature of the salt, and always within ten degrees. Further, $T_{s,b}$ was approximately constant over a wide range of operating conditions.

The effective bed area was also difficult to measure, and for lack of a better value or reasonably good evaluation procedure, this parameter was assigned the value calculated by the Excel model.

The heat loss term required more careful consideration. If the loss correlation given by Equation (3.2.13) is employed, then any deviation from this prediction must be due to additional losses encountered by the system because of the failure of Equation (3.2.13) to exactly analyze the thermal system. In this instance, the heat loss term for Equation (3.2.17) can be represented by:

$$Q_{losses,actual} = \dot{m}_A c_p (T_{bed} - T_{A,in})_{Model} - \dot{m}_A c_p (T_{bed} - T_{A,in})_{Experimental} + Q_{losses,model} \quad (3.2.18)$$

which can be rewritten as:

$$Q_{losses}^E = \dot{m}_A c_p (\Delta T_{bed}^M - \Delta T_{bed}^E) + Q_{losses}^M \quad (3.2.19)$$

In this sense, the inclusion of Equation (3.2.19) in the calculation of Equation (3.2.17) renders Equation (3.2.19) an absolute error term. Theoretically, the value given by Equation (3.2.19) may be taking into account more than just heat losses to bed internals and the reactor wall: it could compensate for errors in the calculation of other parameters, errors in the experimental work, as well as poor assumptions made in the process of developing the model. Assuming that these other sources of error are minimal, the value of Equation (3.2.19) should represent the actual heat losses from the system.

The error described above is absolute. If no heat losses had been considered in the model, then the predicted temperature, T_{bed} , would have an inflated value. Although the second term in Equation (3.2.19) would become zero and therefore unnecessary, the first term would increase to compensate for the loss of the second term. The absoluteness of the loss term is important since it is being subtracted from the enthalpy terms, which being state functions, are inherently absolute.

4.0 Apparatus

As previously mentioned, the aim of this study was to:

1. Design a fluidized bed system which would recover heat from a molten material, and extend the results to industrial conditions;
2. Use a low temperature slag analogue consisting of a LiCl/KCl eutectic mixture to determine the effect of molten feedrate, air temperature, air velocity, and bed particle size on the heat recovery and the heat transfer coefficients;
3. Predict the heat recovery and the heat transfer coefficients of the eutectic system using mathematical models and the Excel Solver routines and compare the calculated values to those obtained experimentally.

The latter two objectives were achieved exclusively using computer models; the logic for the algorithm was already described in Section 3.2. The remainder of this section will deal with the materials required to achieve the first objective, which was the experimental portion of the work.

4.1 Feed Material

The first step in the experimental work was to select a material to act as a low temperature analogue of blast furnace slag. The desired properties of the material were:

1. Low viscosity. Blast furnace slag has a tap viscosity of the order of 0.3-2 N/sm². It was decided to choose a material with a lower viscosity in order to avoid flow problems.
2. Low melting temperature. Low temperatures are easier to achieve than high temperatures. Also, at temperatures above approximately 700°C, radiative heat transfer becomes significant and must be accounted for in modeling routines. In

addition, low temperature systems are easier to handle when dealing with a new system such as this.

After investigating a number of molten salt systems, it was decided that a molten LiCl/KCl with the eutectic composition was most suitable. The viscosity of the mixture can be calculated using the following two equations if an ideal solution of the components is assumed, and the rule of mixtures is employed:

$$\mu_{LiCl} = 0.10888 \times 10^{-3} \exp\left(\frac{2295.5}{T}\right) \quad (4.1.1)$$

$$\mu_{KCl} = 0.06168 \times 10^{-3} \exp\left(\frac{3012.4}{T}\right) \quad (4.1.2)$$

For all the feed temperatures employed, the viscosity of the mixture was calculated to be of the order of 10^{-3} Pas, which is approximately an order of magnitude greater than that of room temperature water, and much below that of blast furnace slag. On the other hand, the binary eutectic met the low melting temperature criterion; the eutectic temperature can be seen in the phase diagram in Figure 4.1 to be approximately 352°C.

4.2 Equipment

The design of the feed equipment required considerable development and refinement. The problems arose mainly from two sources:

1. Although the LiCl/KCl met the design requirements stated in Section 4.1 (low viscosity and melting temperature), the molten salt was extremely corrosive. The corrosiveness can be attributed mainly to the LiCl, which is present in the eutectic mixture at 45 %mol or 31.8 %wt. The chloride mixture was extremely hygroscopic when solid; absorption of water onto the salt produced hydrochloric acid.

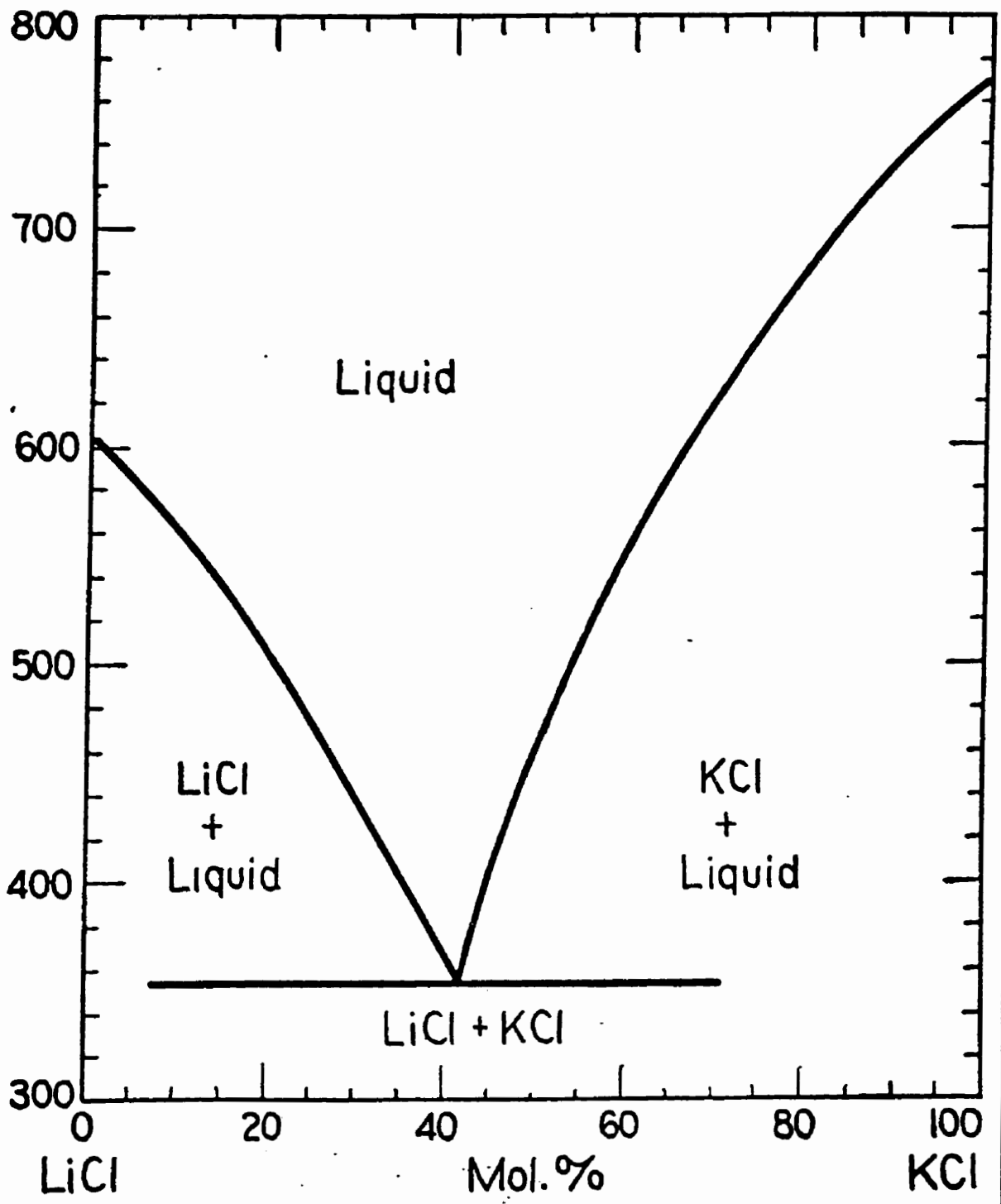


Figure 4.1 Phase diagram of the KCl-LiCl system in degrees Celsius (Elchardus and Laffitte, 1932).

2. Much larger volumes of air are required to fluidize the bed than to adequately recover heat from the system. It was desired to develop a fluid bed that was top fed. As a result, the surface area of the bottom of the molten salt feeder was minimized to prevent excessive convective heat transfer from the feeder to the fluidizing air. If this goal was not achieved, great difficulty would have been encountered when trying to maintain the molten feed temperature. In some cases, it proved impossible to keep the salt molten.

In the initial design, it was decided to heat a magnesia crucible externally using a pair of 145W ceramic tube heaters. A hole was drilled in the crucible using a 1/32" (0.79375mm) masonry drill bit. The molten flow was excessive and non-dropwise. A nipple, which was manufactured from mortar cement, was attached to the bottom of the crucible to reduce the flow and to create droplets in a consistent manner. Non-dropwise flow was undesirable since it led to quick defluidization of the bed. The flowrate remained too large to achieve operation of the bed for even a few seconds. The surface area of the crucible exposed to the fluidizing air was excessive, thus cooling occurred, and a thin layer of solidified salt was observed to form along the inside bottom surface of the crucible

A second design attempted to utilize hypodermic needles. In this case, the needle was attached to the bottom of a magnesia crucible using a stainless steel adapter and mortar cement. The needle portion was heated with a small length of Nichrome wire (using a variac) wrapped around a quartz tube in which the needle was centred. The crucible was heated using the original pair of tube heaters. The mortar cement proved to be porous to the molten salt and shorted out the heaters. As a result, the heaters were destroyed.

A third design was a modification of the second; a stainless steel vessel was used in place of the magnesia crucible so that the needle adapter could be welded to the crucible. This alternative was proposed in order to avoid the leaks encountered with the use of mortar cement. The crucible was heated to 973K by a long length of Nichrome wire wrapped around a ceramic tube which was connected to a variac and a temperature controller. However, the stainless steel crucible or its oxide reacted with the eutectic salt melt, rendering this design inadequate. On the other hand, the hypodermic needle (made of stainless steel and a Ni/Cr alloy) and the stainless steel adapter were not significantly corroded.

A fourth design was based on a longer heater, which was similar in construction to that described above, and was used to heat a glass syringe. During the initial heat tests, the needle adapter fell off the syringe due to the different thermal expansivities of the two materials in the syringe (glass and stainless steel). A corrosion-resistant, non-porous cement made of zirconia was used to attach the adapter to the syringe. The cement worked well; no leaks of the molten salt occurred. However, the low softening temperature of the glass syringe would not allow enough heat to be applied to the feed mechanism to ensure a constant flowrate; the needle would periodically clog with frozen salt. Furthermore, upon dismantling the apparatus, it was found that the syringe had cracked, possibly due to local overheating of the glass, the inability of the glass to accommodate the salt as it solidified and expanded, or the thermal stresses created by having 'cold' air exhausted from the fluidized bed to the bottom of the hot syringe. As well, the needle and the needle adapter were corroded by the salt, and both were deemed inappropriate for further test work.

The fifth and final design employed the use of a quartz feeder. Quartz was found to be very suitable for this application because of its inert behaviour towards the eutectic salt melt. Quartz is also resistant to the thermal stresses created by the heating coil and the fluidizing air. Since quartz can be easily formed, then it was possible to design a feeder of reasonable capacity with a minimal surface area exposed to the fluidizing air. The data were collected on the system shown in Figure 4.2.

The feed system needed to provide a slow, dropwise, yet continuous flow of molten eutectic to avoid premature defluidization of the bed. A quartz feeder with a height of 15cm and an inside diameter of 4.5cm that narrowed to a 700 μ m aperture at the bottom was used. Approximately 75mL of molten material could be contained within the feeder. The quartz feeders are shown in Figures 4.3.

The feeder was shouldered on the top surface to allow it to rest on an alumina tube of 52mm inner diameter, 5mm thick, and 245mm length. Around the alumina tube was wound 14 gauge Nichrome wire, which was connected to a variac in series with 120V power. The heating element was well insulated with an approximately 60mm thick layer of insulative blanket. A Type K thermocouple in a ceramic sheath was connected to a temperature controller (Model ORF 4228) that monitored power to the variac. The feeder was situated 200mm from the top surface of the reactor so that the heat cycle of the feeder would not affect the reactor temperature measurements.

The fluid bed reactor tube was 4cm inner diameter, 100cm long, and of stainless steel construction. A bed support consisting of 65 mesh copper screen was located

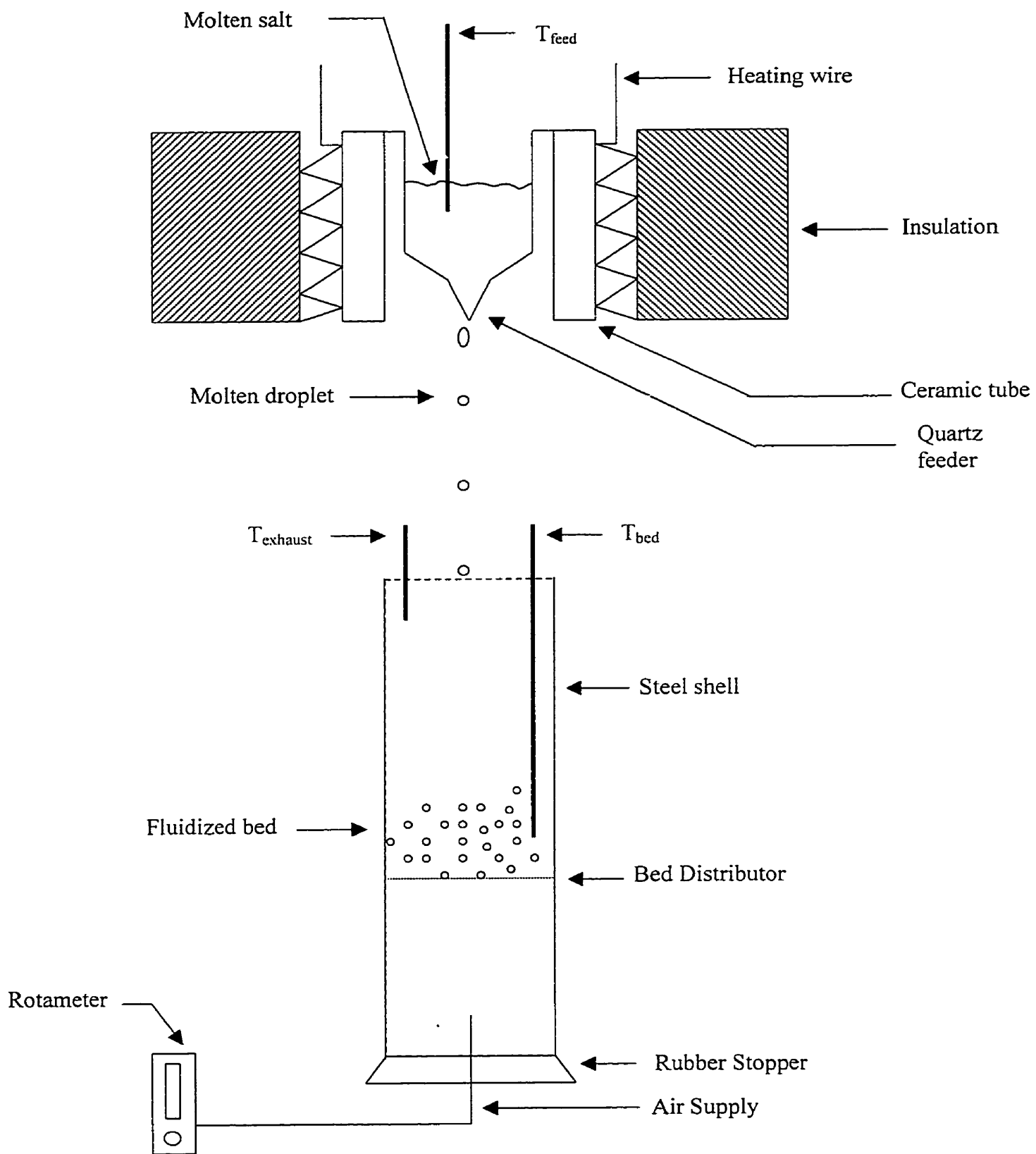


Figure 4.2 Fluidized bed and molten salt feeder configuration.

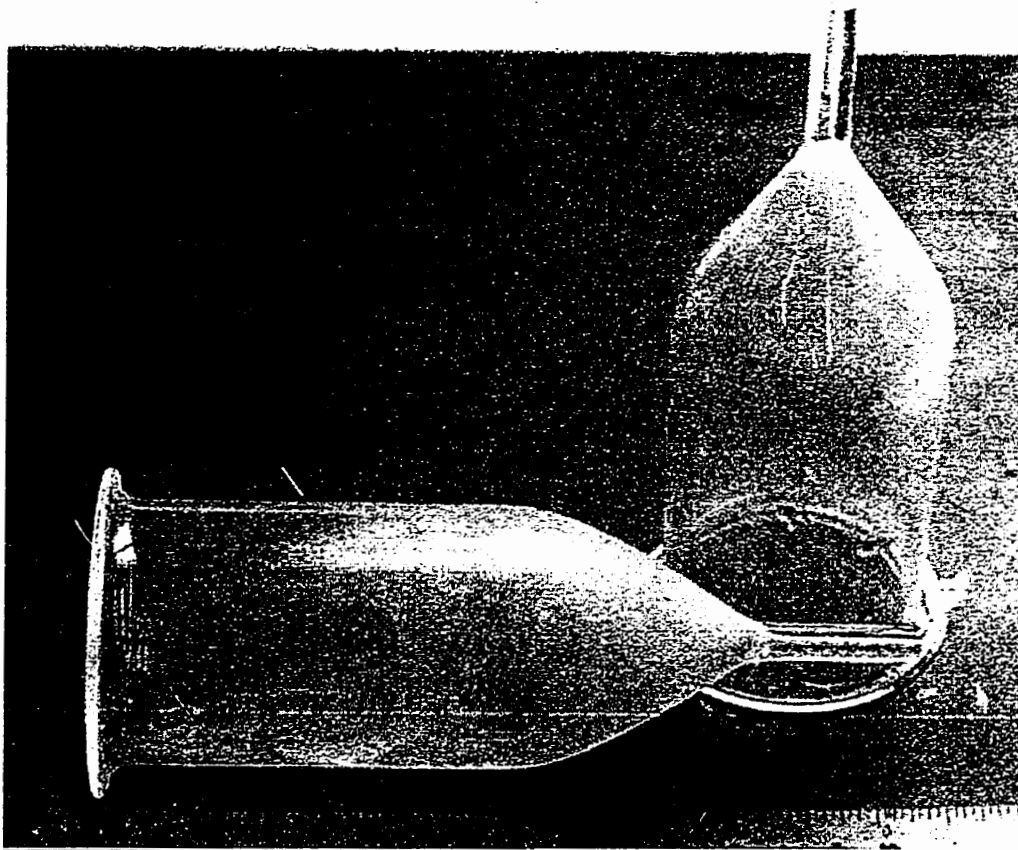


Figure 4.3 Quartz feeders used for fluid bed heat recovery in this study. The shouldered edge allowed the feeders to rest on a ceramic tube externally heated with Nichrome wire. The scale is in inches.

35.5cm from the top surface of the reactor. This provided the physical support to the 1mm glass beads, which formed the initial bed material and had good fluidization characteristics. Immersed at a location approximately halfway between the bed support and the top of the fluidized bed was a sheathed 1/8" Type K thermocouple to record the bed temperature. A bare wire Type K thermocouple located 25mm from the top surface of the reactor measured the exhaust air temperature. These thermocouples were connected to an Omega temperature recorder (Model RD114-T).

Air was introduced to the system by 1/4" stainless steel tubing inserted through a rubber stopper, which formed an airtight seal with the reactor bottom. The volumetric flow of air was measured with an Union Carbide (Model 01050) rotameter. The air pressure was measured with a pressure gauge on the incoming air to the rotameter.

The eutectic mixture was prepared using Fisher laboratory grade LiCl, and industrial grade KCl obtained from Reheis, Inc. The mixture was melted and superheated in a 220V 22A muffle furnace (Model TH-37 MG-91P) manufactured by Pottery Supply House; once the desired temperature was achieved, the molten feed was transferred to the quartz feeder. In this way, the heater on the feeder was required only to maintain a given temperature, and did not have to provide the energy to melt the mixture.

4.3 *Experimental Design*

Initially, the variables of importance to this study were thought to be:

- Salt feed temperature;
- Salt flowrate;
- Salt composition;
- Molten droplet diameter;

- Bed particle density;
- Bed particle size;
- Bed mass;
- Air flowrate;
- Air preheat temperature;
- Air pressure.

After some preliminary experience with the system, the above list was refined to the following three variables:

- Air flowrate;
- Salt flowrate;
- Mass of bed.

In practice, the molten content of the bed at temperatures for salt feed temperatures above 773 K was too great, and this caused the bed to defluidize. Since the eutectic temperature of the salt melt is 625 K, and at least 50 degrees of superheat are required to maintain a uniformly molten feed, then there is little opportunity for experimental design with this variable. For this reason the salt feed temperature was kept constant for all trials at 723 K.

In Figure 4.1, it can be seen that the liquidus temperature increases substantially with deviation from the eutectic composition. Consequently, the feed temperature would have to be increased to keep the salt molten. As previously discussed, any increase in the salt feed temperature would adversely affect bed operation. For this reason, the eutectic composition was used in all the experiments.

The diameter of the molten droplets was governed by the size of the quartz feeder. This could have been altered, but only if the apparatus was increased in scale. For example, in order to change the diameter of the molten droplets, it would be necessary to change the diameter of the quartz feeder tube. The feeding tube was made as small as possible by a professional glass blower. Any increase in the diameter of the tube would cause too much molten material to enter the system, causing defluidization. Alternatively, multiple quartz feeding tubes could be used to provide the molten feed. In a reactor of this scale, multiple tubes would be impossible to arrange, and the overall flowrate of molten material would be too great. The only option would be to design a much larger fluidized bed system capable of handling higher maximum molten feedrates.

Prior to obtaining a system capable of stable fluidization, many bed materials were tried. Bubble alumina provided a material with a large diameter and relatively low density, but the radial mixing in the bed was insufficient and defluidization occurred rapidly with the introduction of the molten salt. Also, silicon carbide particles of approximately 10 mesh size did not fluidize sufficiently. Two different mixtures of glass beads were used: one with a bimodal size distribution (0.75mm and 2.5mm), and another with fine (< 1mm) glass beads. Neither material worked well in practice. Finally, 1mm glass beads proved to be the material of choice. Due to the lack of a number of suitable bed materials, the density and the particle size were not varied in the experiments.

Air pressure could not be varied: the air source was the pilot plant compressor, which served a number of users and could not be altered.

Since the behaviour of the bed could not be accurately predicted from a fluid mechanics standpoint, then it was difficult to design an experimental matrix in advance of the actual experiments. Instead, it was decided to gather as much data as possible, and to

investigate the limits of operation for the three parameters mentioned above. However, the majority of the trials were conducted within the boundaries given in the table below.

Table 4.1. Bounds of experiments conducted in this study.

Variable	Minimum	Maximum
Bed Mass	100 g	150 g
Salt Flowrate	0.65 g/min	4.9 g/min
Air Flowrate	0.064 m ³ /min	0.099 m ³ /min

5.0 Results and Discussion

The effects of various factors on the convective droplet and gas to particle heat transfer coefficient are discussed in this chapter. The experimental results are compared to the values obtained from the modeling work as described in Chapter 3.

5.1 *Model Predictions*

The scope of this project included a study of the effect of various parameters on the gas to particle heat transfer coefficient. The model predictions were determined for the following factors:

- Salt feed temperature;
- Salt flowrate;
- Molten droplet diameter;
- Bed particle density;
- Bed particle size;
- Bed mass;
- Air flowrate;
- Air preheat temperature;
- Air pressure.

The control conditions in the model were similar those used in the experiments; these are given in Table 5.1.

Table 5.1. Modeling conditions for the Excel algorithm.

Parameter	Baseline Value	Minimum Value	Maximum Value
Salt feed temperature	973 K	773 K	1173 K
Salt flowrate	5 g/min	1 g/min	50 g/min
Molten droplet diameter	2 mm	0.1 mm	5 mm
Bed particle density	1600 kg/m ³	800 kg/m ³	2400 kg/m ³
Bed particle size	1 mm	0.6 mm	2.2 mm
Bed mass	150 g	25 g	200 g
Air flowrate	$U_o/U_{mf} = 1.5$ m/s	$U_o/U_{mf} = 1.0$ m/s	$U_o/U_{mf} = 3.0$ m/s
Air temperature	298 K	273 K	448 K
Air pressure	1.5 atm	1 atm	3 atm

In addition to the gas to particle heat transfer coefficient, a number of other values were calculated by the model including system temperatures and recovered heat from both the atomizing and the fluidizing sections. The convective heat transfer coefficient between the falling molten droplet and the passing air stream was also modeled.

5.1.1 Analysis of Model Data

The computer model was used primarily as a theoretical screening study to determine the importance of process variables to the fluidized bed heat recovery system. It must be stressed that because the model contained only basic fluid mechanic considerations, the results must be taken with a degree of caution. The exact fluidization regime was not accounted for in the algorithm, and it will be shown in Section 5.2 that this effect was significant. Furthermore, modeled interaction effects would be completely unrepresentative of the system, and were therefore not included. Table 5.2 summarizes the results predicted by the computer model: the response of the gas to

particle heat transfer coefficient, bed temperature, air exhaust temperature, and total recovered heat.

Table 5.2. Modeled response of the fluidized bed heat recovery system to changes in system parameters.

Main Effect	Response of Heat Transfer Coefficient	Response of Bed Temperature	Response of Exhaust Temperature	Response of Recovered Heat
Salt Feed Temperature	0.0	33.4	34.9	173.9
Salt Feedrate	-32.5	425.7	431.6	487.4
Molten Droplet Diameter	-6.7	48.6	-0.23	0.08
Density of Bed Particles	132.2	-73.3	-74.2	7.7
Diameter of Bed Particles	51.6	-128.8	-130.4	12.0
Bed Mass	0.0	0.0	0.0	0.0
Dimensionless Velocity U_o/U_{mf}	187.0	-70.6	-71.6	7.4
Air Preheat	-52.1	189.2	189.1	-17.8
Air Pressure	90.2	-65.3	-66.5	6.2

Varying the salt feed temperature from 773 K to 1173 K yielded a horizontal line when this parameter was plotted against the heat transfer coefficients. This result can be seen in Figure 5.1. This implies that both heat transfer coefficients are unaffected by the feed temperature of the salt. Although the feed temperature affects the total heat recovered by the system, and therefore the heat recovery efficiency, the heat transfer coefficients are not affected.

The effect of salt flowrate on both of the heat transfer coefficients is illustrated in Figure 5.2. Initially, both curves monotonically decrease slightly; beyond approximately 5 g/min the curves are horizontal. This is consistent with the results given

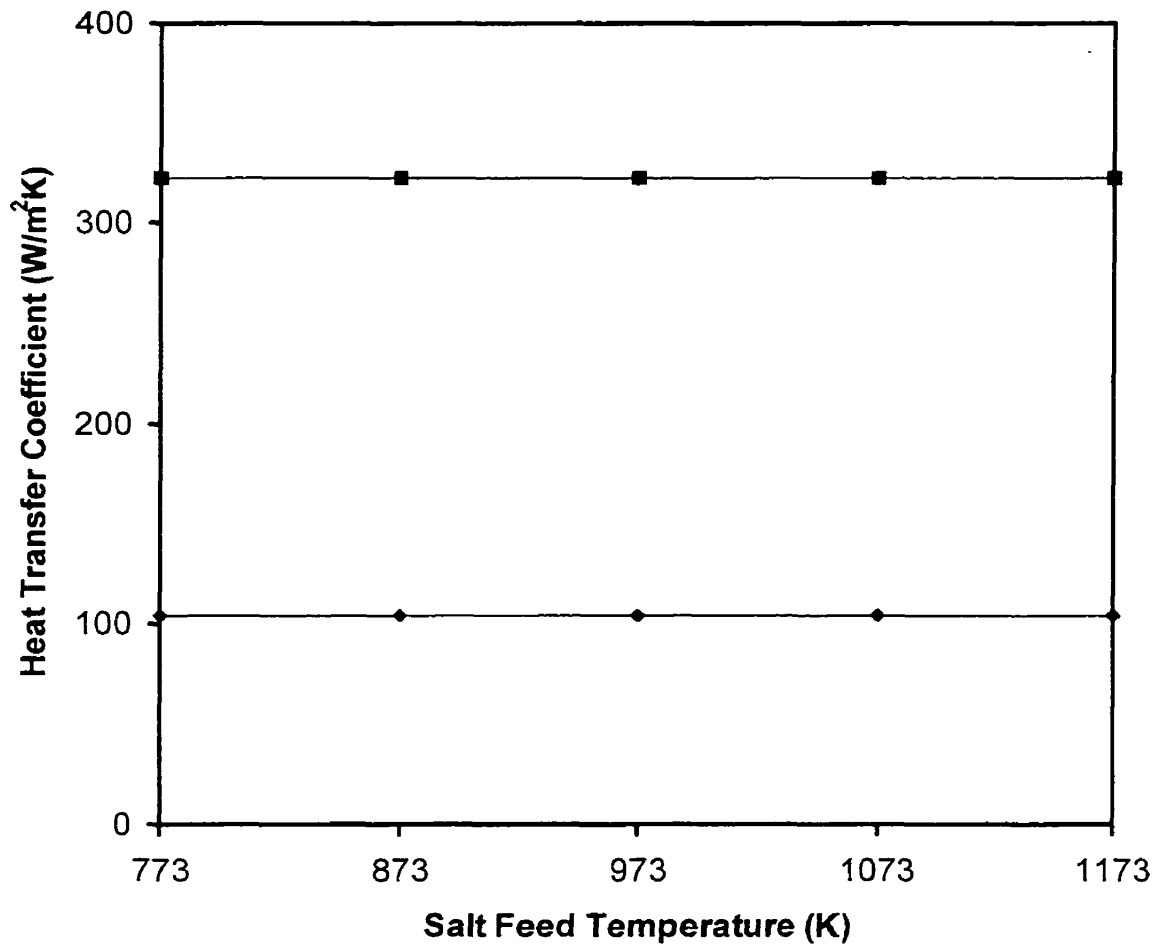


Figure 5.1 Effect of salt feed temperature on the droplet and gas to particle heat transfer coefficients. As the feed temperature was varied, the remainder of the parameters were fixed at their baseline values (◆ indicates the heat transfer coefficient between the falling molten droplet and the surrounding air; ■ indicates the gas to particle heat transfer coefficient in the fluidized bed)

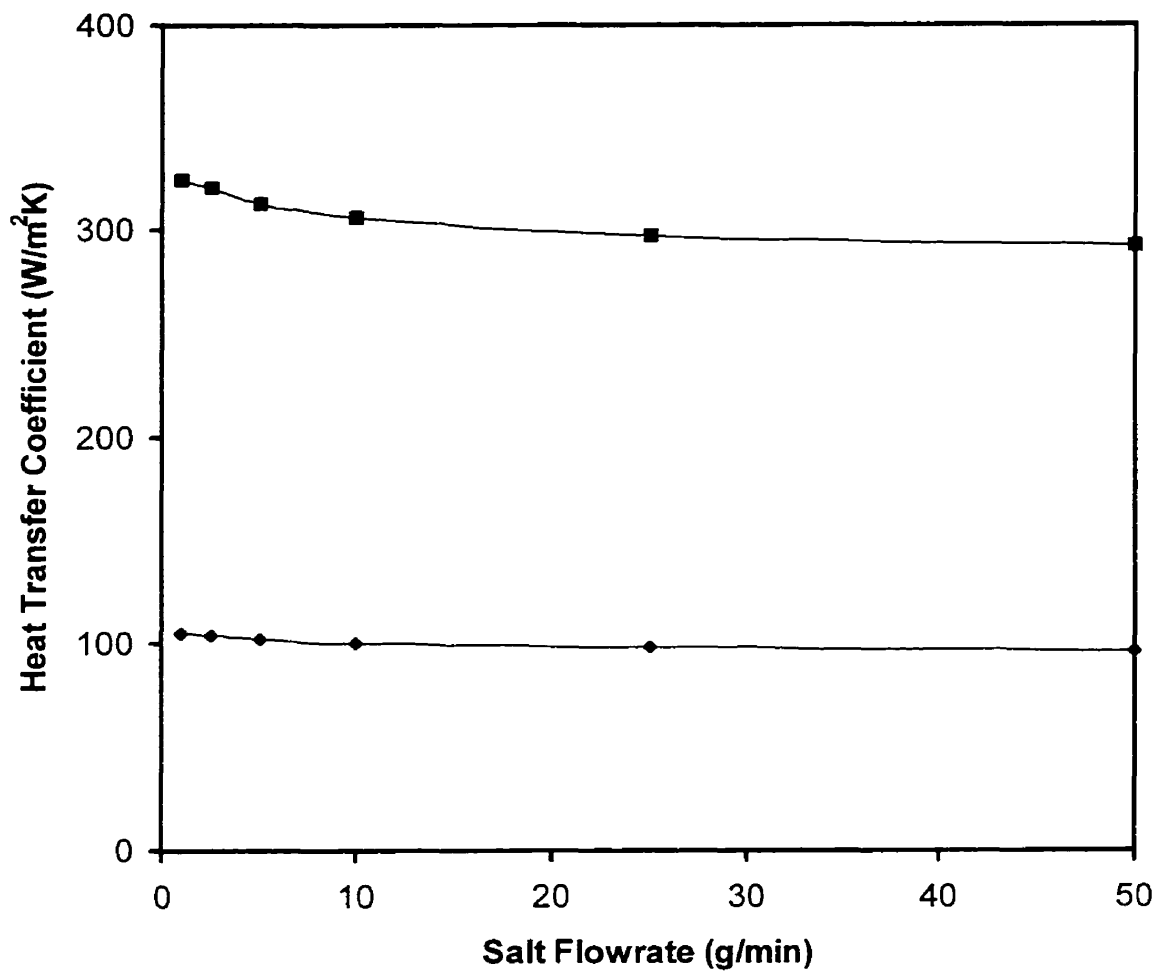


Figure 5.2 Effect of salt feedrate on the droplet and gas to particle heat transfer coefficients. As the salt feedrate was varied, the remainder of the parameters were fixed at their baseline values (◆ indicates the heat transfer coefficient between the falling molten droplet and the surrounding air; ■ indicates the gas to particle heat transfer coefficient in the fluidized bed).

in Figures 5.13 to 5.15, which predicted only a slight dependency of the gas to particle heat transfer coefficient on the salt feedrate. At low feedrates, the proportion of molten material to bed material is low, and there exists a great opportunity for heat transfer to occur. As the feedrate increases, this ratio decreases, and there is less opportunity for heat transfer in the bed, and the coefficient drops accordingly. The heat transfer coefficient of the falling droplet is independent of the feedrate, since it is dependent on the volume of the droplet and the speed with which it falls; for a constant feeding tube diameter, these parameters do not change.

The diameter of the falling molten droplet in the atomizing section had no effect on the gas to particle heat transfer coefficient. However, as the droplet size was increased, the heat transfer coefficient between the droplet and the passing air decayed exponentially. These effects can be seen in Figure 5.3 below. The model does not account for complex fluid mechanics, and assumes that the molten droplet breaks up upon entering the bed. As a result, the diameter of the falling droplet has no effect on the gas to particle heat transfer coefficient in the fluidized bed. However, the heat transfer coefficient between the falling droplet and the air is dependent mainly on the surface area to volume ratio of the droplet as well as the air velocity. By increasing the droplet diameter, the area to volume ratio is decreased, hampering heat transfer and decreasing the coefficient of heat transfer between the droplet and the air.

As the density of bed particles was increased, both heat transfer coefficients increased monotonically as shown in Figure 5.4. As the density of the bed particles is increased, the minimum fluidization velocity is also increased. In order to keep the air flowrate (U_o/U_{mf}) at 1.5 m/s, the air flowrate had to be increased. The droplet heat

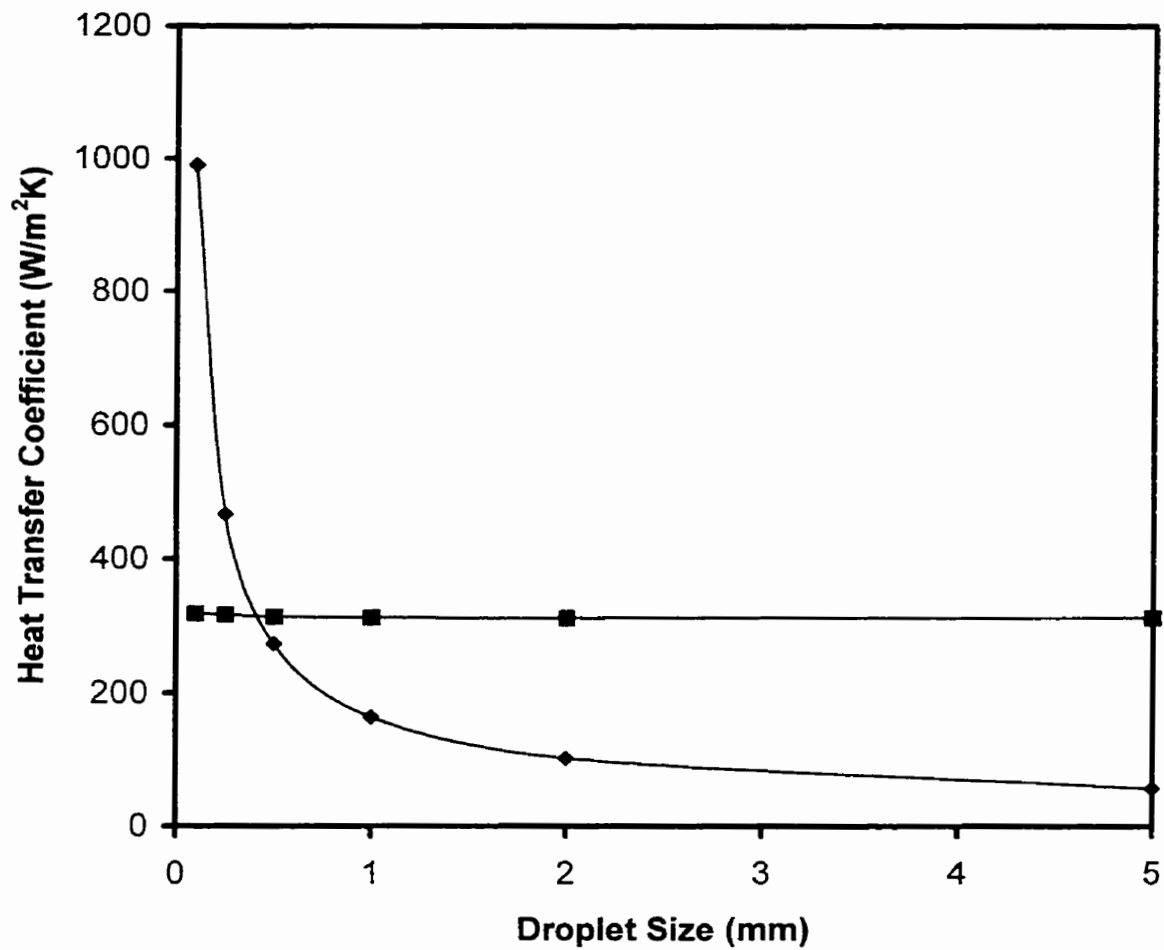


Figure 5.3 Effect of droplet size on the droplet and gas to particle heat transfer coefficients. As the droplet size was varied, the remainder of the parameters were fixed at their baseline values (◆ indicates the heat transfer coefficient between the falling molten droplet and the surrounding air; ■ indicates the gas to particle heat transfer coefficient in the fluidized bed).

transfer coefficient is convective, and with an increase in external velocity, an increase in the coefficient is expected. The gas to particle heat transfer coefficient also increased with bed particle density. The effect of increasing the particle density is biased with the increase in air flowrate to keep the hypothetical system fluidized. The additive effect is notable; the droplet heat transfer coefficient increased by 37.1% while the gas to particle coefficient increased by 56.1 %.

As the bed particle size was increased, both heat transfer coefficients increased. The droplet heat transfer coefficient increased via the same phenomenon as when the bed particle density was increased. The effect of the increased air velocity on the droplet coefficient was much greater than the combined effect of increased particle size and air velocity on the gas to particle coefficient. This statement can be quantified by an 83% increase in the droplet coefficient as compared to a 17.8% increase in the gas to particle coefficient over the same range of increasing particle size. The corresponding data is shown in Figure 5.5.

Varying the bed mass from 25g to 200g had no effect the heat transfer coefficients. The lack of relationship is due to the exclusion of the reliance of the heat transfer on the fluidization regime within the model algorithm. This is apparent in Figure 5.6.

Figure 5.7 shows the effect of the gas velocity on the heat transfer coefficients. The gas velocity was increased from $U_o/U_{mf} = 1$ to $U_o/U_{mf} = 3$. Over this range, both heat transfer coefficients increased linearly: the droplet coefficient by 47.9%; the gas to particle coefficient by 72.8%. These observations are evident in Figure 5.7. Since both heat transfer coefficients are convective, then an increase in both coefficients is expected

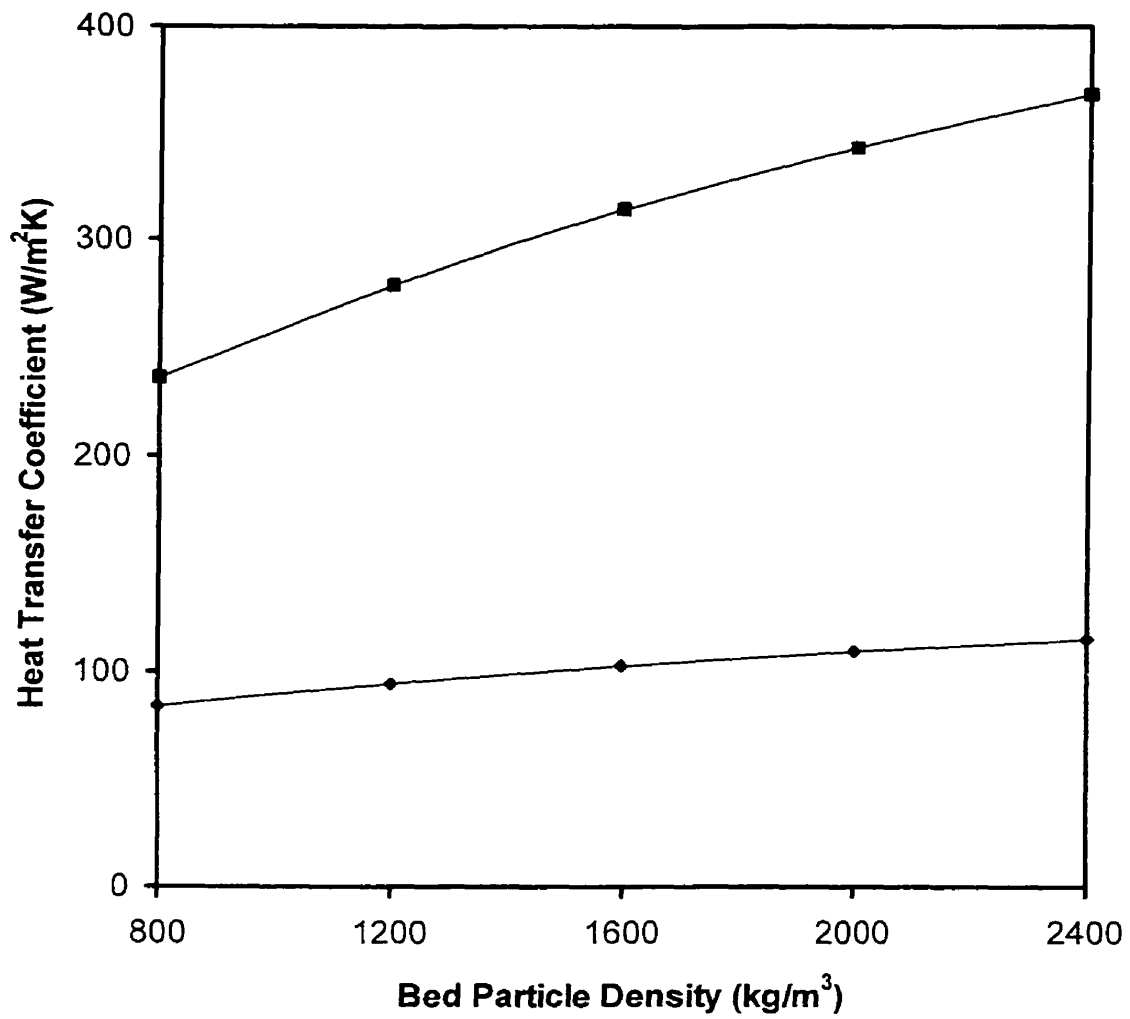


Figure 5.4 Effect of bed particle density on the droplet and gas to particle heat transfer coefficients. As the bed particle density was varied, the remainder of the parameters were fixed at their baseline values (◆ indicates the heat transfer coefficient between the falling molten droplet and the surrounding air; ■ indicates the gas to particle heat transfer coefficient in the fluidized bed).

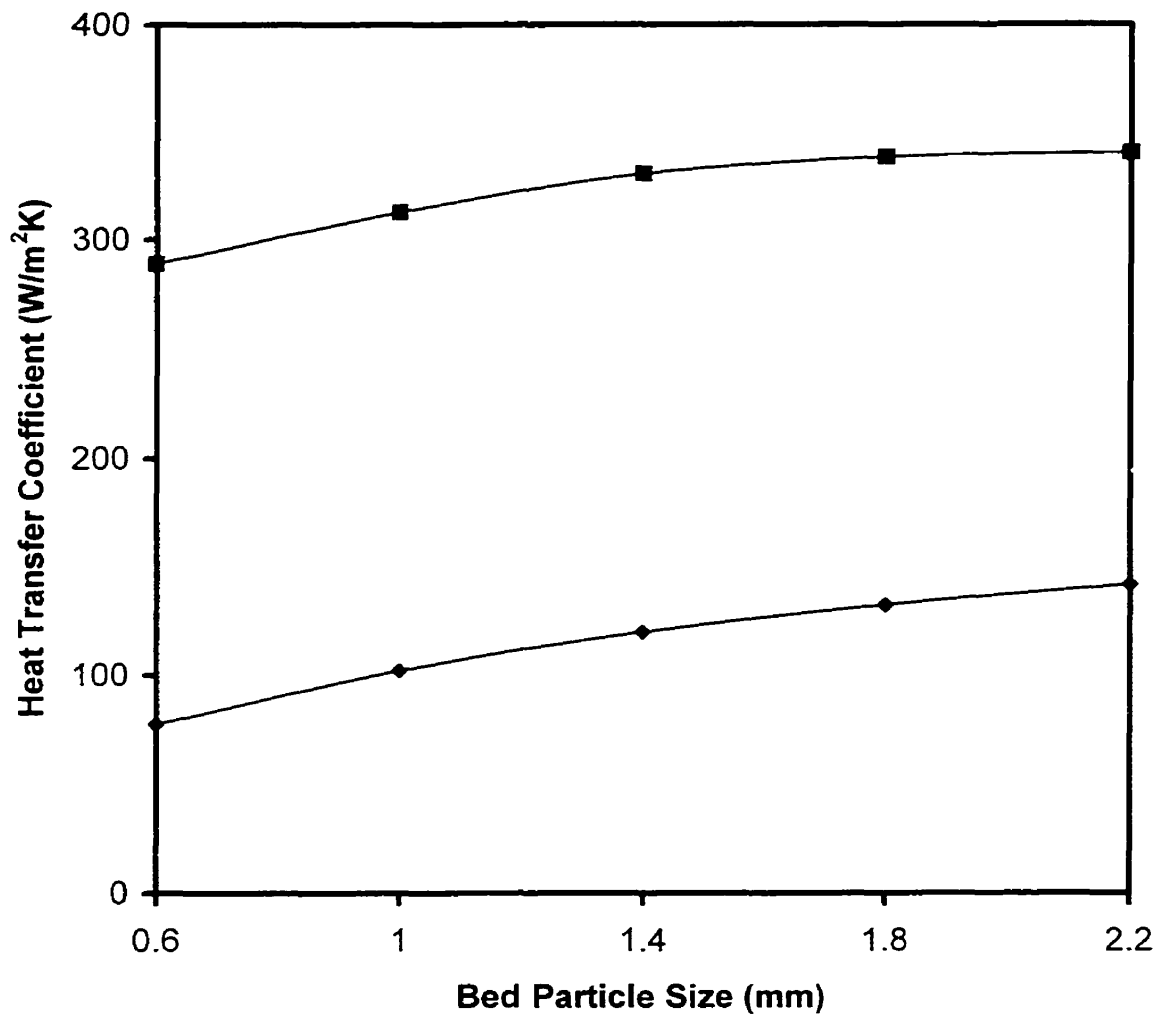


Figure 5.5 Effect of bed particle size on the droplet and gas to particle heat transfer coefficients. As the bed particle size was varied, the remainder of the parameters were fixed at their baseline values (◆ indicates the heat transfer coefficient between the falling molten droplet and the surrounding air; ■ indicates the gas to particle heat transfer coefficient in the fluidized bed).

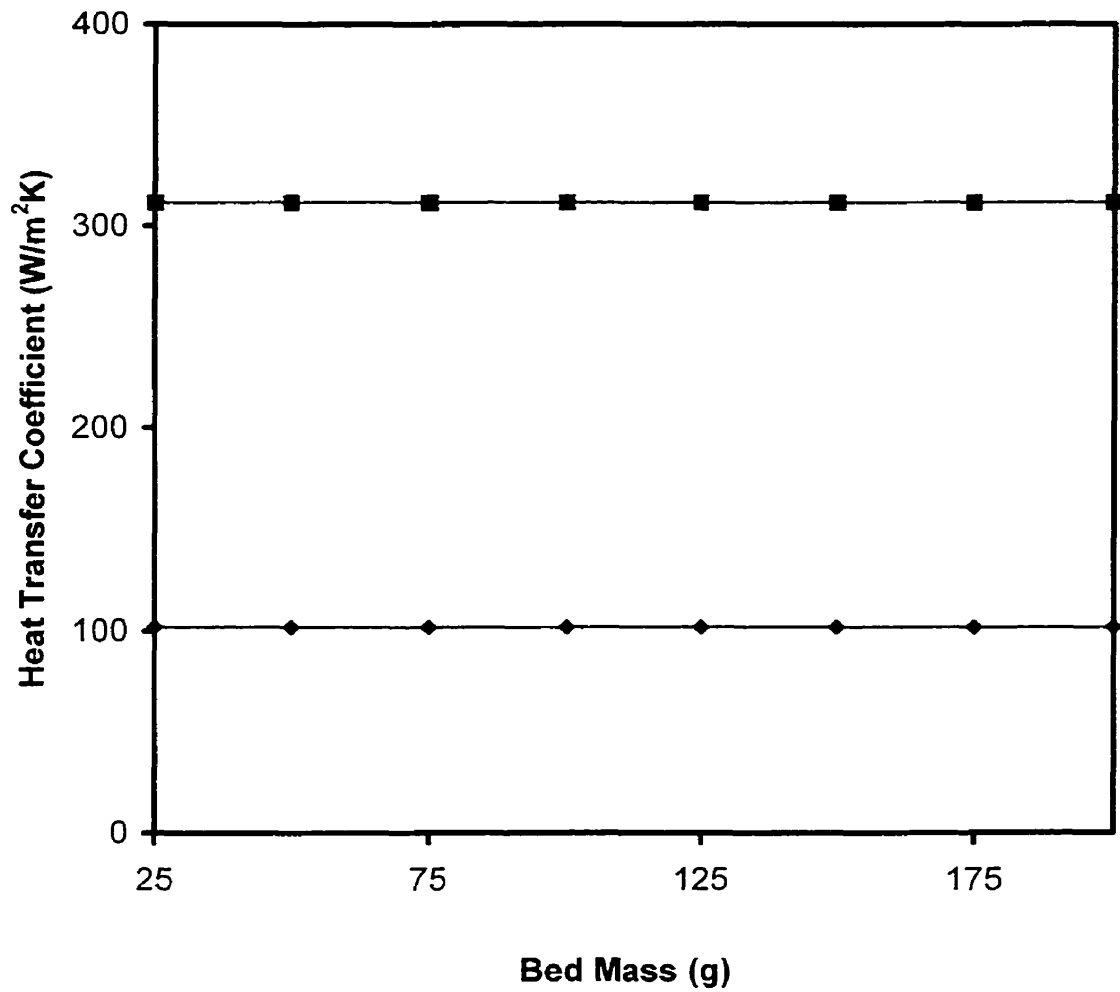


Figure 5.6 Effect of bed mass on the droplet and gas to particle heat transfer coefficients. As the bed mass was varied, the remainder of the parameters were fixed at their baseline values (◆ indicates the heat transfer coefficient between the falling molten droplet and the surrounding air; ■ indicates the gas to particle heat transfer coefficient in the fluidized bed).

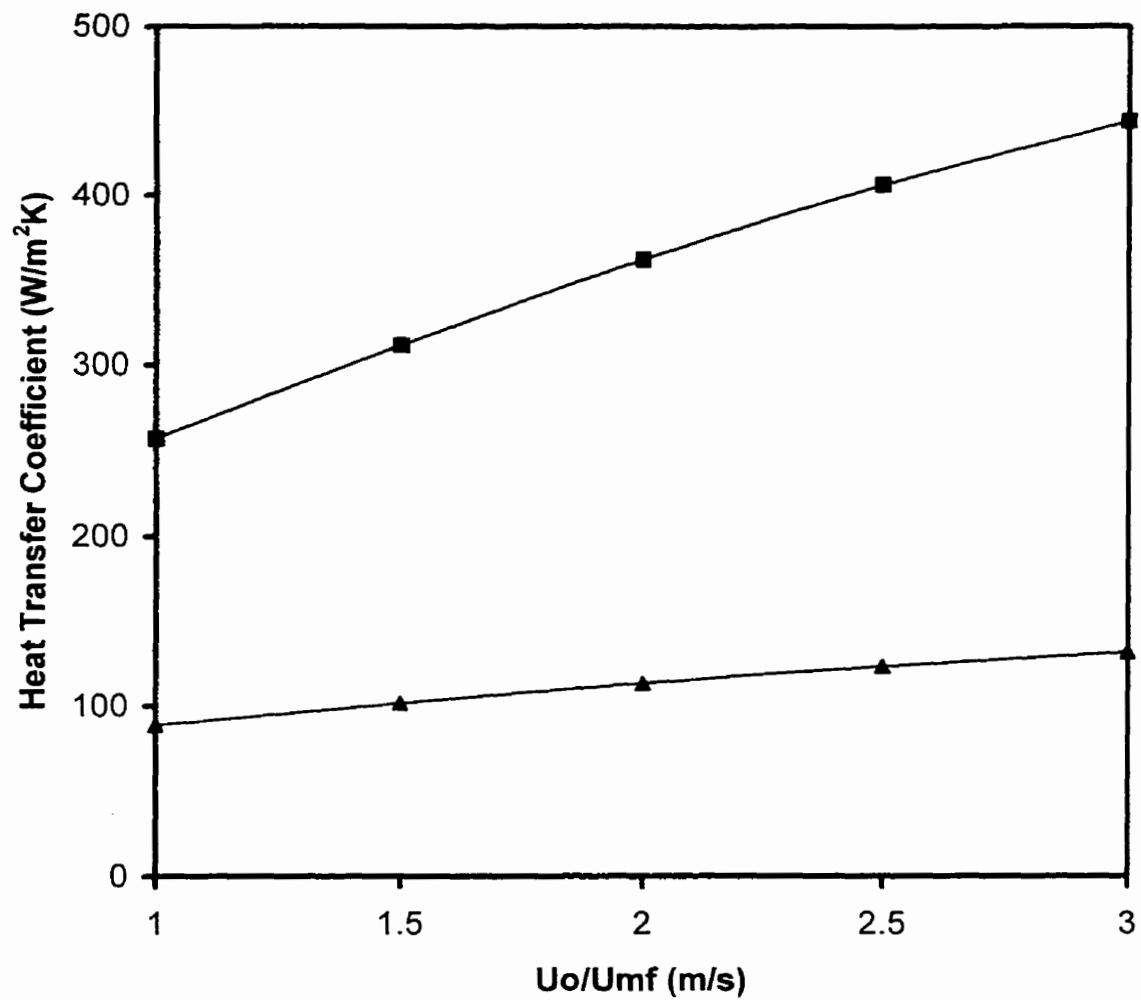


Figure 5.7 Effect of air flowrate on the droplet and gas to particle heat transfer coefficients. As the air flowrate was varied, the remainder of the parameters were fixed at their baseline values (◆ indicates the heat transfer coefficient between the falling molten droplet and the surrounding air; ■ indicates the gas to particle heat transfer coefficient in the fluidized bed).

for an increase in the air velocity. The magnitude of the increase is directly dependent on the correlation used for the Nusselt number as shown in Equation 3.2.9.

Increasing the air preheat temperature resulted in a slight depression of the droplet heat transfer coefficient, and there was a linear relationship over the range of air temperatures studied. The gas to particle heat transfer coefficient also decreased with increasing air preheat temperature, although the relationship was not exactly linear. The droplet coefficient decreased by 11.7% while the gas to particle coefficient was reduced by 16.2%. The results can be seen in Figure 5.8. The main result of increasing the inlet air temperature is a decrease in the available thermal driving force for heat transfer. This is manifested by a decrease in the heat transfer coefficients. Changing the inlet air temperature had a much greater effect than the molten salt feed temperature because of the relative amounts of each in the fluidized bed system. Furthermore, altering the air feed temperature changes the physical properties of the air, which affects the heat transfer coefficient according to the Nusselt number correlation.

The effect of air pressure on the heat transfer coefficients can be seen in Figure 5.9. The heat transfer coefficients increased nearly linearly with air pressure. Increasing the pressure by a factor of three increased the heat transfer coefficient of the droplet by 21% and the gas to particle heat transfer coefficient by 30.5%. An increase in pressure results in an increase in the gas to particle heat transfer coefficient since the fluidization quality is improved with an increase in the static pressure in the bed. As a result, a more even flow of gas through the particulate phase is obtained. Furthermore, changing the pressure may change the flow regime, which may affect the heat transfer. This will be shown in the next section.

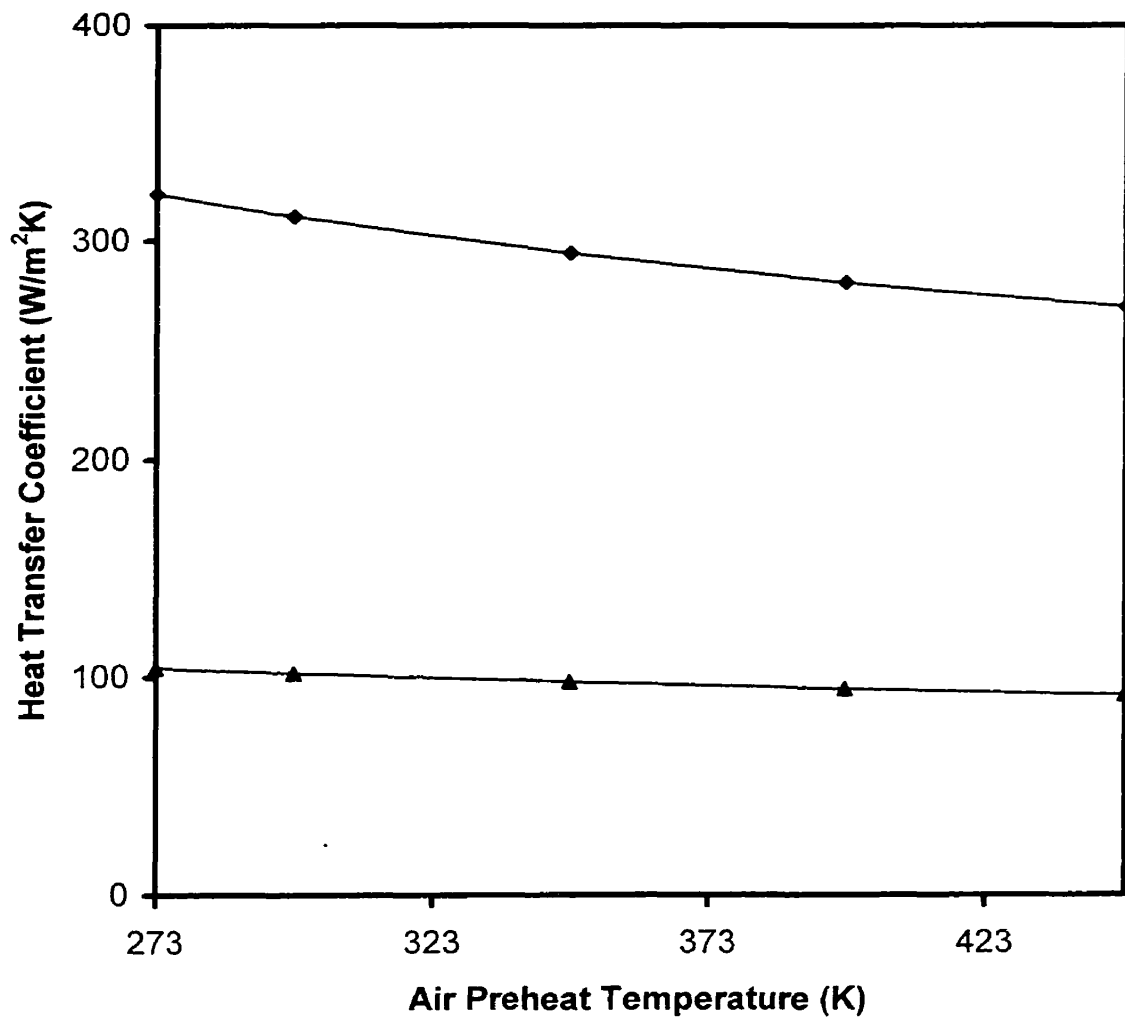


Figure 5.8 Effect of air preheat temperature on the droplet and gas to particle heat transfer coefficients. As the temperature was varied, the remainder of the parameters were fixed at their baseline values (◆ indicates the heat transfer coefficient between the falling molten droplet and the surrounding air; ■ indicates the gas to particle heat transfer coefficient in the fluidized bed).

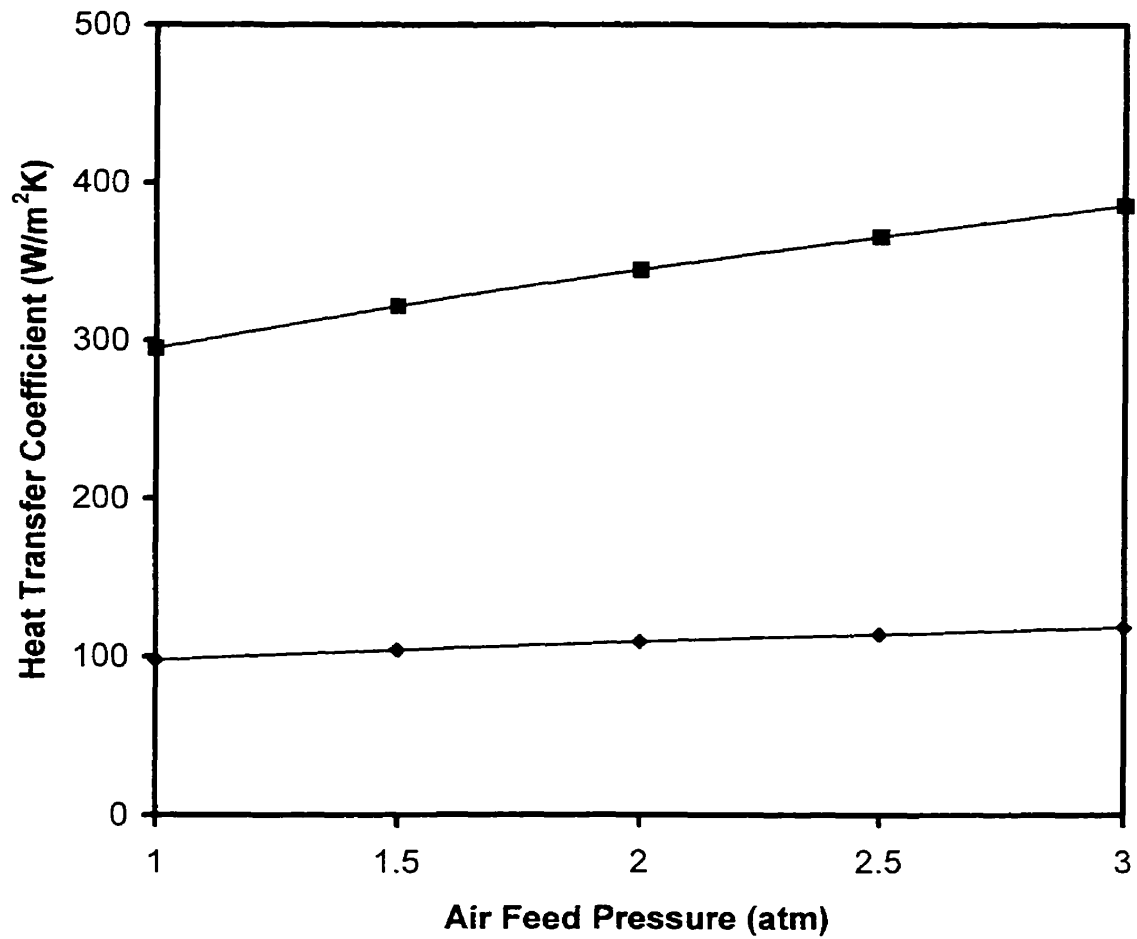


Figure 5.9 Effect of air pressure on the droplet and gas to particle heat transfer coefficients. As the air pressure was varied, the remainder of the parameters were fixed at their baseline values (◆ indicates the heat transfer coefficient between the falling molten droplet and the surrounding air; ■ indicates the gas to particle heat transfer coefficient in the fluidized bed).

Overall, the trends present in Figures 5.1 to 5.9 and in Table 5.2 are reasonable, and confirm that the model algorithm was logical. The variables of greatest importance to the gas to particle heat transfer coefficient directly relate to the air and bed properties, and include:

- The dimensionless air velocity;
- The density of bed particles;
- The air pressure.

It should be stressed that in order to maintain baseline conditions, the air flowrate had to be changed as the bed density was varied. As a result, the effect of bed density given in Table 5.2 is biased with air velocity. This biasing was necessary in order to maintain fluidization of the simulated bed as the density of the particles was varied.

The most significant variables included the salt feedrate, the air preheat, and the diameter of the particles in the bed. Increasing the salt feedrate or the air preheat temperature results in a greater heat load to the system and higher operating temperatures. Increasing the bed particle diameter decreases the effective area of the bed, hindering heat transfer, which results in lower operating temperatures.

The total heat recovered is a strong function of the salt feedrate and the temperature; if more heat is added to the system, then more is available to be recovered. This is true for the modeled system, which assumed no heat losses to the surroundings. This scenario is contrasted with modeling the experimental conditions, which attempted to model heat losses to the surroundings via the reactor wall and the reactor internals.

5.2 Experimental Data

In Chapter 4, a list of variables to be studied was presented. The parameters were air flowrate, salt flowrate, and bed mass. The figures included in the present section provide a comparison between the heat transfer coefficients obtained through experimentation and the use of the procedure outlined in Section 3.2.6, and specifically Equation (3.2.17) and the heat transfer coefficients predicted by the Excel model described in Sections 3.2.1 through 3.2.5.

5.2.1 Bed Mass

The first variable studied was the initial mass of the particles charged to the fluidized bed. The data presented below in Figures 5.10 and 5.11 are at constant air flowrates and for various salt feedrates, and show the effect of bed mass. The model predicted that the salt feedrate should have little impact on the gas to particle heat transfer coefficient. In this way, variable biasing with bed mass is minimized.

The model data, when plotted in this manner yields a horizontal line, while the majority of the experimental data exhibits a linear behaviour with a negative slope. As well, some data in both figures have significant parabolic character. Furthermore, agreement between the experimental and the predicted values increased as both the air flowrate and the bed mass increased. At $0.078\text{m}^3/\text{min}$ air, the percentage difference between the actual and the predicted gas to particle heat transfer coefficients decreased from 17.0% at a bed mass of 100g to 7.8% at a bed mass of 150g. With an air flowrate of $0.085\text{m}^3/\text{min}$, the percentage difference drops from 7.9% to 1.4% as the bed mass was increased from 100g to 150g. The data presented in Figures 5.10 and 5.11 are each at constant air flowrates and for various salt feedrates. During experimentation, fine control of the molten salt feedrate proved difficult; it was impossible to replicate a given salt

flowrate for a variety of bed masses and air flowrates due to the batch nature of the process. Therefore, comparisons at different bed masses while holding the salt feedrate constant could not be performed. As a result, data points were selected for different bed masses with similar salt feedrates (designated as low, medium, and high in Figures 5.10 and 5.11); thus, the effect given in the results is biased. The computer model predicted that the salt feedrate would have little effect on the heat transfer coefficient, and variable biasing in this way would be minimized. Low to high salt feedrates span the range 0.9-4.9 g/min.

The computer simulation was primarily a thermal balance. Fluid mechanics was used in the model to calculate the minimum fluidization velocity, and the parameters on which it depended. No method was provided to determine the minimum required bed mass or other mechanical parameters.

It was believed that a critical bed mass would exist below which fluidization with a molten feed would be impossible. At low bed masses, the pressure drop across the bed is too low to allow fluidization to occur. As a result, the gas can percolate between the solid particles and between the particle and the reactor wall without fluidizing the system. In order to determine this mass, the quartz feeder was operated with a very low molten feedrate, and the mass of the bed was varied. It was found that bed masses of 50g and 75g were inoperable even with minimal molten feedrates and high air flowrates. The raw data for these runs is included in Appendix A.

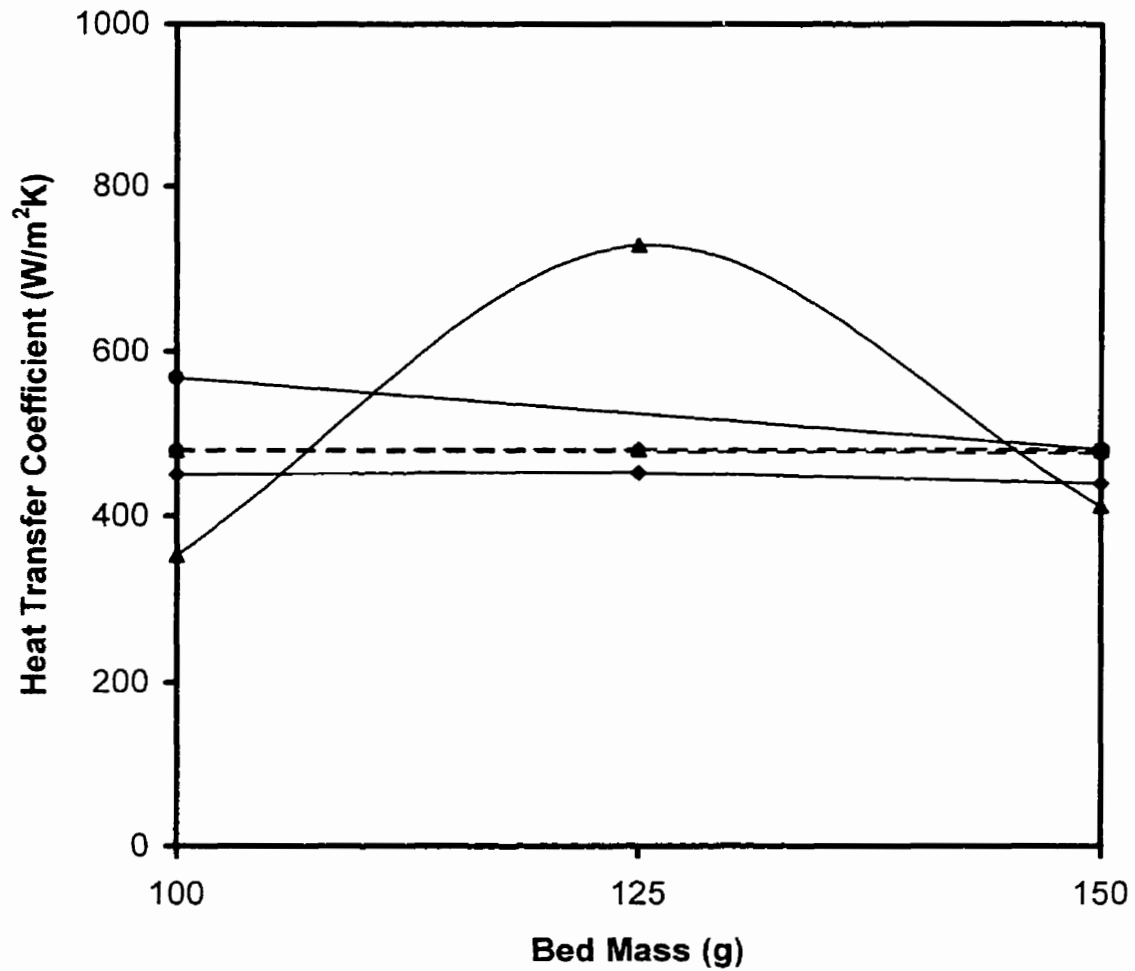


Figure 5.10 The gas to particle heat transfer coefficient as a function of the bed mass for various molten salt feedrates. The air flowrate in all cases is 0.078m³/min. The solid curves represent experimental data while the dashed curves are the values predicted by the Excel algorithm. The molten salt feedrate is indicated by low (◆), medium (▲), and high (●).

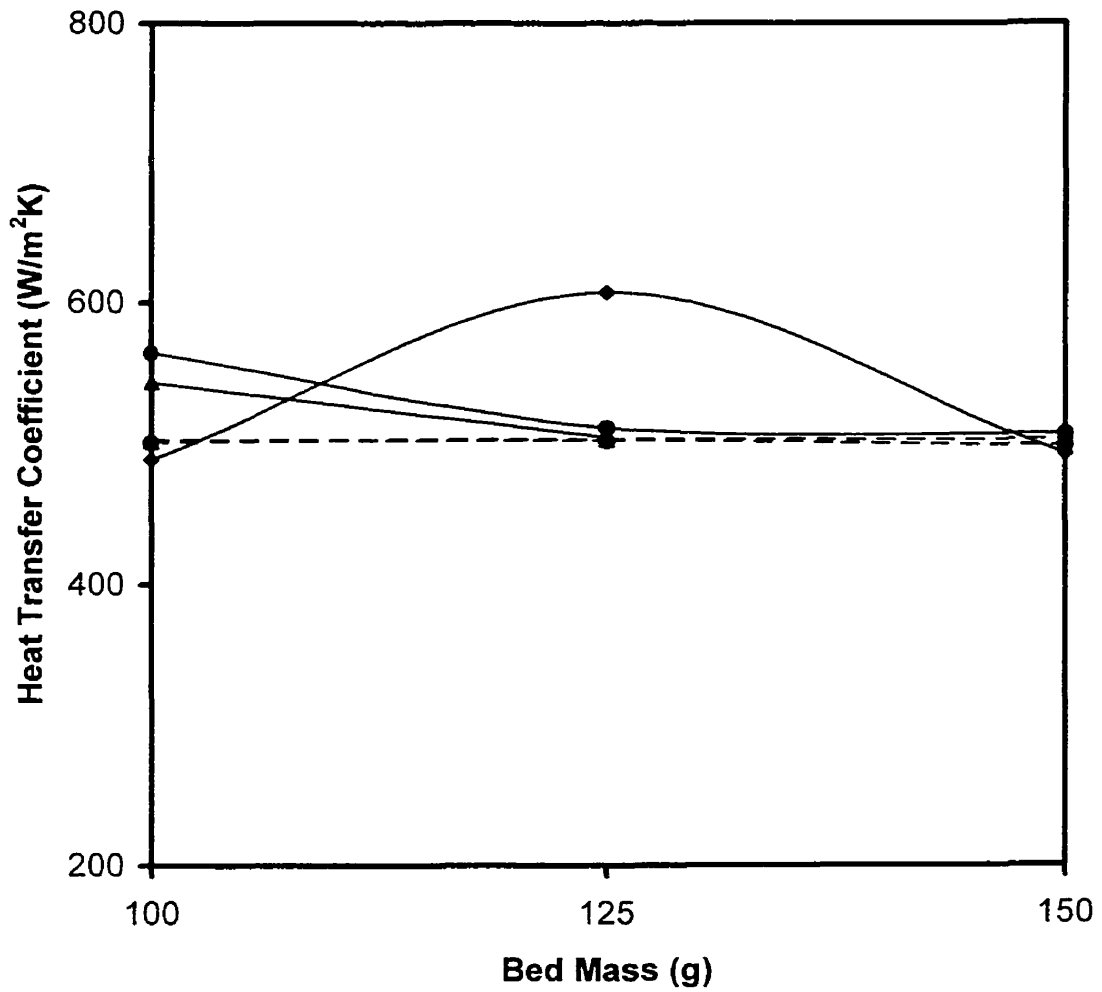


Figure 5.11 The gas to particle heat transfer coefficient as a function of the bed mass for various molten salt feedrates. The air flowrate in all cases is $0.085\text{m}^3/\text{min}$. The solid curves represent experimental data while the dashed curves are the values predicted by the Excel algorithm. The molten salt feedrate is indicated by low (\blacklozenge), medium (\blacktriangle), and high (\bullet).

In Chapter 3, a description was given of the Geldart Classification of Particles. Clearly, the system employed in the present experimental study was in the Class D regime, which is spoutable. According to Kunii and Levenspiel, bubbling can be made to occur if the bed is shallow, has sufficient diameter, and the gas velocity is not much more than the minimum required. It is evident that at masses below 100g (the minimum bed mass used successfully), fluidization of the bed was incomplete and bubbling was the predominant mode of gas transfer throughout the bed. As the air flowrate increases, the bed bubbles more violently, and eventually begins to slug. This pattern is evident in Figure 5.12.

During experimentation, it was observed that a bed mass of 100g produced a uniformly and smoothly fluidized bed when compared with masses of 125g and 150g. When the bed mass was increased to 125g, the system behaved unpredictably: sometimes bubbling, sometimes slugging. Bed masses of 150g slugged considerably, but in a stable and predictable manner. Also, as the bed mass was increased from 100g to 125g to 150g, the maximum air flowrate was decreased from $0.099\text{m}^3/\text{min}$ to $0.092\text{m}^3/\text{min}$ to $0.085\text{m}^3/\text{min}$, and the minimum from $0.078\text{m}^3/\text{min}$ at 100g and 125g to $0.064\text{m}^3/\text{min}$ at 150g. The decreased air flowrate with increased bed mass is consistent with statements made by Kunii and Levenspiel, who observed that an enormous amount of gas is needed to fluidize Geldart D solids, often far more than required for the physical or chemical operation. In such situations, spouted beds are recommended, since they need much less gas (Kunii and Levenspiel, 1991).

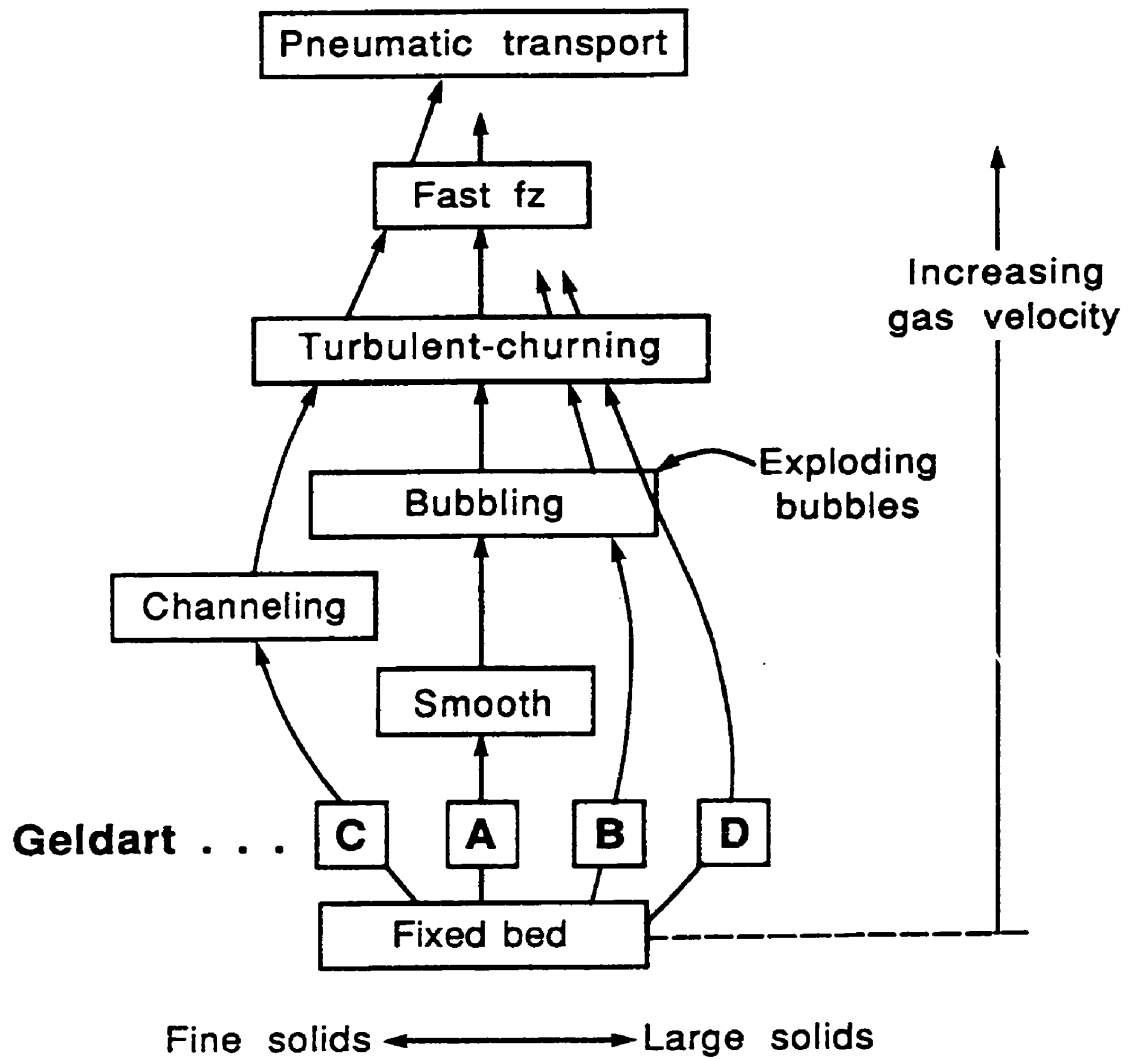


Figure 5.12 Change in fluidization regimes with solids type and gas velocity (Kunii and Levenspiel, 1991). The abbreviation fz refers to fluidization.

The decreasing air requirements for bed operation as the bed mass was increased, in light of the above quotation, suggests that a transition in fluidization regimes occurred as the bed mass was increased from 100g to 150g. The unstable operation observed at 125g indicates that the transition point was at approximately this mass. Another consequence of the decreased air requirements for increased bed masses is that the gas to particle heat transfer coefficient in the bed will be reduced, and as a result, so too will the heat recovery efficiency.

Furthermore, Figures 5.10 and 5.11 illustrate results from the experimental work, and compare them to predicted values. From these figures the following may be inferred:

1. The percentage difference between the actual and the predicted gas to particle heat transfer coefficients decreases with increasing air flowrate and bed mass;
2. The actual heat transfer coefficient appears to be a function of bed mass. Although this seems to be the case from examination of Figures 5.10 and 5.11, it actually is not the case as will be seen in the following discussion.

As mentioned, the curves presented in Figures 5.10 and 5.11 are each at a constant air flowrate and for various salt feedrates. During experimentation, fine control of the molten salt feedrate proved difficult; it was impossible to replicate a given salt flowrate for a variety of bed masses and air flowrates due to the batch nature of the process. Therefore, comparisons at different bed masses while holding the salt feedrate constant could not be performed. As a result, data points were selected for different bed masses with similar salt feedrates (designated as low, medium, and high in Figures 5.10 and 5.11); thus, the effect given in the results is biased. The computer model predicted that the salt feedrate would have little effect on the heat transfer coefficient, and variable biasing in this way would be minimized. The alternative was to bias bed mass with air

flowrate, which was predicted by the model to have a significant effect on the gas to particle heat transfer coefficient. Due to unforeseen phenomena described in the next section, the salt feedrate did have an effect on the heat transfer coefficient. The variable biasing, although necessary, gave results that were not totally representative of the system.

The misrepresentation of the effect of the bed mass on the gas to particle heat transfer coefficient can be quantified as follows. The average difference between the actual and the predicted heat transfer coefficients when the salt feedrate was varied, was in the range of 10.8% - 11.5%. The data in Figure 5.10 illustrate an average difference of 12.5% for bed masses of 100g. Furthermore, the average difference for bed masses of 150g with a variable salt flowrate is 4.9%, while a difference of 4.6% for systems with a bed mass of 150g was shown in Figure 5.11. This information is summarized in Table 5.3 below.

Table 5.3. Comparison of the difference between the actual and the predicted gas to particle heat transfer coefficients when expressed as a function of salt feedrate and bed mass.

Conditions	% Difference as a Function of Salt Feedrate	% Difference as a function of Bed Mass
100g bed and 0.078m ³ /min air	17.0	17.0
100g bed and 0.085m ³ /min air	7.9	7.8
150g bed and 0.078m ³ /min air	14.4	7.8
150g bed and 0.085m ³ /min air	1.8	1.9

Based on the information in Table 5.3 and the discussion above, it is evident that the apparent reliance of the gas to particle heat transfer coefficient on bed mass was a result of the variable biasing. Overall, the bed mass did not have a direct influence on the heat transfer coefficient. Rather, varying the bed mass changed the operational

characteristics of the bed from smoothly fluidized and bubbling to unstable slugging to stable slugging. Therefore, altering the bed mass altered the fluidization regime of the bed, which in turn affected the heat transfer coefficient. Since the computer model excluded advanced fluid mechanics calculations, then these effects were not accounted for in the predicted values given as dashed lines in Figures 5.10 to 5.11 and 5.13 to 5.18.

5.2.2 Salt Feedrate

The effect of the molten salt feedrate on the gas to particle heat transfer coefficient is illustrated in Figures 5.13 to 5.15. For all cases, the feed temperature of the salt was 723 K. The curves predicted by the Excel model are horizontal, indicating a weak relationship between the heat transfer coefficient and the molten salt feedrate. No consistent pattern is discernible for the experimental values, except that as the molten salt feedrate is increased, the deviation between the actual and the predicted conditions is, for the most part, reduced. If all the data is accounted for, the average error between the actual and the predicted values is reduced from 11.5% at low salt flowrates to 10.8% at high flowrates. At a bed mass of 150 g, this difference is more marked: the percentage difference between the actual and the predicted gas to particle heat transfer coefficients is reduced from 8.8% at 0.89 g/min to 0.97% at 4.46g/min and 4.9g/min.

Figures 5.13 to 5.15 indicate that the modeling algorithm predicts no reliance of the gas to particle heat transfer coefficient on the molten salt flowrate. This result is consistent with Equation (3.2.9), which was used to calculate the heat transfer coefficient. This relationship indicated that the Nusselt number, and therefore the gas to particle heat

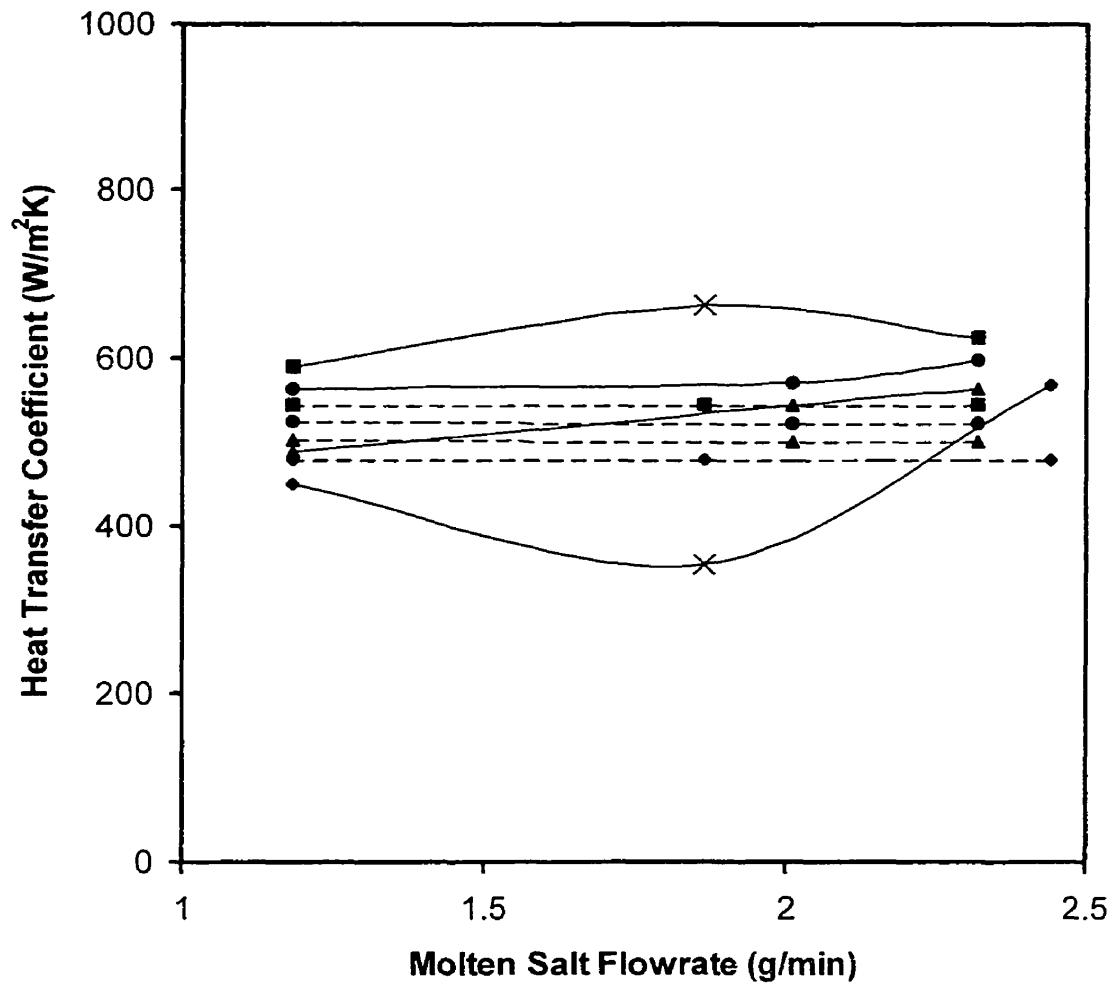


Figure 5.13 The gas to particle heat transfer coefficient as a function of the molten salt feedrate for various air flowrates. The fluidized bed had an initial mass of 100g. The solid curves represent the experimental data while the dashed curves are the values predicted by the Excel algorithm. The air flowrates are 0.078m³/min (◆), 0.085m³/min (▲), 0.092m³/min (●), and 0.099m³/min (■). Data points denoted by a cross were measured near the end of an experiment, and were both recorded for a molten salt flowrate of 1.86g/min and air flowrates of 0.085m³/min and 0.099m³/min.

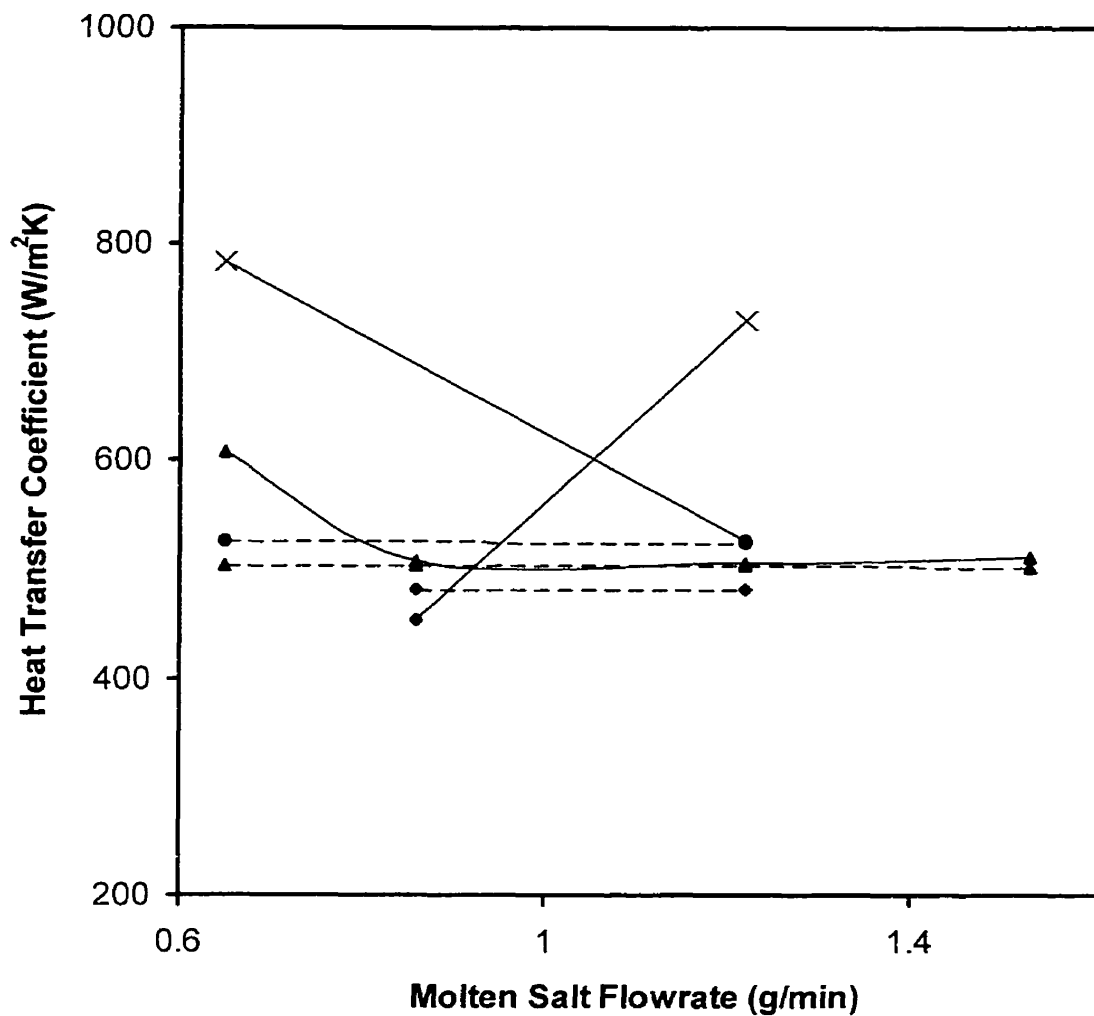


Figure 5.14 The gas to particle heat transfer coefficient as a function of the molten salt feedrate for various air flowrates. The fluidized bed had an initial mass of 125g. The solid curves represent the experimental data while the dashed curves are the values predicted by the Excel algorithm. The air flowrates are $0.078\text{m}^3/\text{min}$ (\blacklozenge), $0.085\text{m}^3/\text{min}$ (\blacktriangle), and $0.092\text{m}^3/\text{min}$ (\bullet). Data points denoted by a cross were measured near the end of an experiment, and were recorded for molten salt flowrates 0.65 g/min and 1.22 g/min $0.092\text{m}^3/\text{min}$ and $0.085\text{m}^3/\text{min}$, respectively.

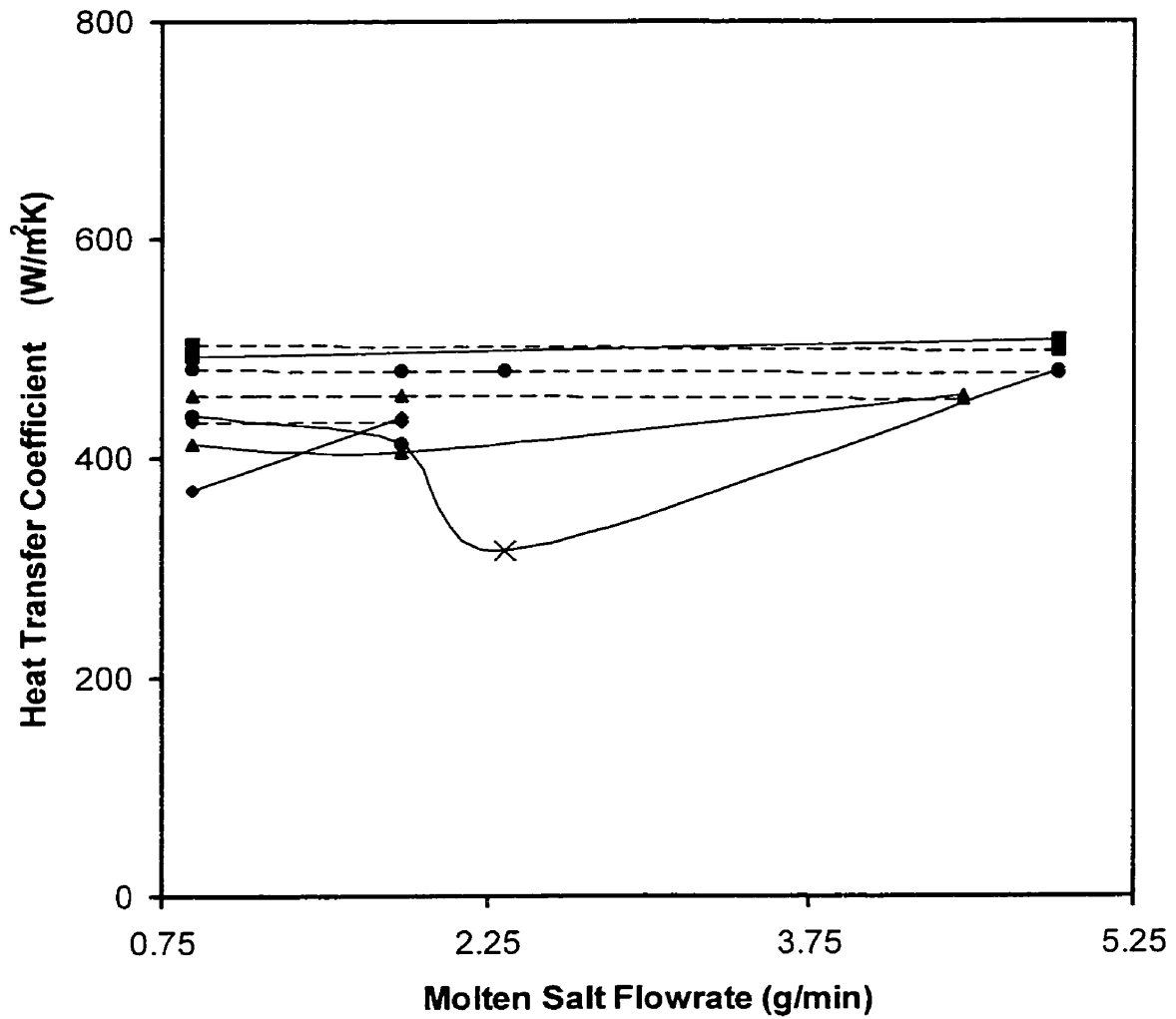


Figure 5.15 The gas to particle heat transfer coefficient as a function of the molten salt feedrate for various air flowrates. The fluidized bed had an initial mass of 150 g. The solid curves represent the experimental data while the dashed curves are the values predicted by the Excel algorithm. The air flowrates are 0.064m³/min (◆), 0.071m³/min (▲), 0.078m³/min (●), and 0.085m³/min (■). The data point denoted by a cross was measured near the end of an experiment, and was recorded for a molten salt flowrate of 2.33 g/min and an air flowrate of 0.078m³/min.

transfer coefficient, was a function of the Reynold's number of the bed particles and the Prandtl number of the fluid passed through the bed.

Since neither of the dimensionless quantities depends on the molten flowrate, then there is no theoretical dependence of the gas to particle heat transfer on the flowrate. However, over a long period of operation it is reasonable to assume that some of the molten salt will coat the original bed particles. As well, a large portion of salt fed to the bed forms discrete particles made purely of the solidified salt. These particles tended to be small and roughly spherical. At the completion of a successful experiment (15 minutes or more depending on the molten flowrate), it is reasonable to assume that the properties of the bed would be significantly different from those at the outset of data collection. The main differences will be an increase in the average density of the bed particles, the average diameter of the bed particles, and the number of the bed particles.

The density of the KCl/LiCl eutectic solid was 2010kg/m^3 whereas the density of the glass beads used as the initial bed material was 1600kg/m^3 . The increase in density of the bed would lead to an increase in the Reynold's number; this would lead to an increase in the gas to particle heat transfer coefficient.

The average diameter of the bed particles would likely decrease with time. Although some molten salt coats some of the bed particles and increases the diameter of such particles, the majority of salt was observed to solidify as discrete particles in the bed. These particles were much smaller than the glass beads used as the initial bed material. A successful size distribution analysis was not performed on the solidified salt particles; the hygroscopic nature of the solids prevented this. However, based on optical measurements, the particles formed in the bed can be assumed to be approximately 20 mesh or $833\mu\text{m}$. This particle size is significantly less than that of the glass beads, which

have a diameter of 1mm. The overall decrease in the average particle size of the bed would decrease the Reynold's number of the bed, and subsequently the gas to particle heat transfer coefficient.

The number of bed particles present in the bed increases due to the production of the 20 mesh salt particles. This parameter has an indirect influence on the heat transfer coefficient. From the third term in Equation (3.2.11), it can be seen that the heat transferred from the particles to the fluidizing air is

$$Q_{gp} = h_{gp} A_{eff,bed} (T_{bed} - T_{air,in}) \quad (5.4.1)$$

Any increase in the number of bed particles will increase the effective area of the bed. In order to satisfy thermal balances, the left-hand side of the equation must remain constant for a given system. However, if the only change in the system is an increase in the number of bed particles and thus the effective area of the bed, then the heat transfer coefficient must decrease.

As a result of the above discussion, it can be concluded that the gas to particle heat transfer coefficient is a function of time. An extension of this observation is that the heat transfer coefficient is a function of the molten salt flowrate. As the molten salt flowrate is increased, the amount of salt per unit time added to the fluid bed system is increased, and thus the bed density, the average particle diameter, and the number of particles increased with time. Therefore, a system with a low molten salt feedrate would be markedly different from one with a high feedrate after a given amount of time. These differences would be manifested in differences in the gas to particle heat transfer coefficient.

The parameters described above could be included in the model. Such an analysis would require an in-depth study of the mechanics of the system, particularly agglomeration and particle granulation phenomenon. These studies were not a part of the original scope of the project, and were left for future research. However, a brief discussion of the possible mechanisms occurring in the system is given in Section 5.1.2.1.

A typical example of the time-dependent situation described above is given in Table 5.4. The data were taken from Figure 5.14, and rearranged in order of increasing time. The table clearly shows that the actual heat transfer coefficient changes with time.

Table 5.4. Difference between the experimental data and the predicted gas to particle heat transfer coefficients as a function of time for a salt flowrate of 1.22 g/min and a bed mass of 125g.

Air Flow (m³/min)	Time Range (min)	% Difference
0.085	3.5-6	0.4
0.092	8-10	0.3
0.078	14-16.5	51.8

For the first ten minutes of experimentation, there is only a small difference between the actual and the predicted heat transfer coefficients. Beyond 14 minutes, a large increase is observed in the actual gas to particle coefficient, which results in a difference of greater than 50%. This increase can be attributed to a considerable change in bed properties resulting in an actual heat transfer coefficient being significantly different from that predicted by the time independent correlation of Equation (3.2.9). A second explanation for the marked increase in the 14-16 minute time range is related to bed mass. In Section 5.2.1, it was proposed that a fluidization transition region was observed to occur near a bed mass of 125g, and that slugging became more predominant as the bed mass approached 150g. For the cases presented in Table 5.4, the bed mass would be nearly

150g for the duration of the final run. It is quite plausible that changes in the fluid mechanics coupled with the altered bed characteristics led to an actual gas to particle heat transfer coefficient quite larger than that predicted by the model algorithm.

The above explanation regarding the time-dependent bed properties is also valid for the data shown in Table 5.5. It can be seen in Table 5.5 that the difference between the actual and the predicted heat transfer coefficients increases with the time of experimentation.

Table 5.5 Differences between the experimental and the predicted gas to particle heat transfer coefficients as a function of time for a salt flowrate of 1.18 g/min and a bed mass of 100g.

Air Flow (m³/min)	Time Range (min)	% Difference
0.078	4-7	-6.2
0.092	10.5-13.5	-7.5
0.085	16-19	-2.7
0.099	22-24	8.4

The increase is lower than that in Table 5.4, but this can be attributed to the change of fluidization regimes, which occurs in Table 5.5. This change of regimes does not occur in Table 5.4. The initial bed mass was 100g, and at the conclusion of experimentation, the bed mass was 128g. This final system is beginning to enter the fluidization transition region at 125g as discussed earlier. The final data point, which is just entering the transition region, experiences an 11.1% change in percentage difference (from -2.7% to 8.4%) from the predicted heat transfer coefficient values: by far the largest in the data set.

Overall, the evidence collected in this study supports the time dependent theory; Table 5.4 provides the strongest evidence. Additionally, the data points in Figures 5.13 to 5.15 with the largest differences from the predicted conditions were always collected

in the latter third of a given experimental trial. As a result of the time-dependent explanation, these data points have the greatest chance of experiencing time-dependent deviation, and are thus indicated in Figures 5.13-5.15 with a cross.

5.2.2.1 Mechanisms of Particle Growth

As mentioned, the bed at the end of an experimental run will be different from that at the beginning. The final bed material will consist of original bed material that has been coated by the molten material. Also present in the bed will be particles of solidified molten material of approximately 20 mesh size.

The presence of the coated particles can be explained by two mechanisms. The first is known as layered growth, and can be modeled in a way similar to the shrinking core model of chemical reactions (Davidson, 1985). The model assumes the initial particles to be spherical and to have a uniform initial diameter. After some amount of contacting time, the diameter of the glass particles has grown, and the volume of the particle now has a core volume and an annular volume. Physically, this type of particle can be represented by an onion ring, with the onion being the initial glass material, and the breading being the molten material. A number of correlations exist to predict the change in diameter with time as a function of the molten salt feedrate and other variables. This mechanism provides a good description of what was observed in this study. Evidence of this type of particle growth can be found in the photographs in Figure 5.16.

A second mechanism for particle growth applies to this system and explains the agglomeration of particles within the fluidized bed. In this case, an agglomerated particle of an overall diameter is made of uniformly spherical bed particles of smaller diameter. The interstitial volume is filled mostly with solidified molten material, giving the resulting large particle a "pebble-dashed" surface (Davidson, 1985). This phenomenon

has been noted to occur with glass powder and wax, a system with notable similarities to the LiCl-KCl eutectic and the glass beads used in this study.

The production of particles made entirely of the salt melt can be explained by granulation processes. The small particles are made nearly entirely of salt particles that separate from either the annular onion ring particle or the pebble particle. The separation occurs via either thermal or mechanical shocks, which are present in the bed. This postulate is consistent with observations made from the photographs in Figure 5.16. It can be seen that there are many discrete salt particles present in systems with bed masses of 150g in Figure 5.16. In these systems, slugging of the bed was more intense than in beds of lesser mass, and the agglomerated particles would have been exposed to greater levels of mechanical stress. As well, the more intense mixing present in the bed implies that heat transfer would be enhanced leading to the greater possibility of thermal shock

In Figure 5.16 (a) and (b), it is evident that for systems with an initial bed mass of 150g, as the salt flowrate is increased, the approximate size and the relative amounts of large agglomerates remain relatively constant. Over the same range of conditions, the number of discrete salt particles in the bed increases. These observations indicate that there is some interaction effect between the molten droplets fed to the fluidized bed and the agglomerated particles already formed as part of the bed. This effect favours the formation of small discrete salt particles and small salt-glass bead agglomerates over the formation of large salt-glass bead agglomerates by limiting the growth of agglomerates already formed in the bed. This phenomenon can be explained in terms of the relative surface areas of the particles present in the bed. Since the free glass beads (free meaning



Figure 5.16 (a) Photograph of 150g of initial bed material operating with a molten salt flowrate of approximately 1.0g/min. Large agglomerates of glass beads and salt are present, as well as a small amount of discrete salt particles and small agglomerates; a large amount of free glass beads is present; (b) Photograph of 150g of initial bed material operating with a salt flowrate of approximately 4.9g/min. Large agglomerates of glass beads and salt are present in the foreground, as well as a very significant amount of discrete salt particles and small agglomerates dispersed throughout the bed; very few free bed glass beads are present; (c) Defluidization of a bed of 100g initial mass due to the formation of large agglomerates in the fluidized zone. The large agglomerate in the foreground is nearly 2.5 cm in diameter. The scale is in inches.

that the glass beads have not yet directly encountered any molten salt) are greater in number and smaller in diameter than the larger salt-glass bead agglomerates, then the free glass beads have a greater collective surface area, and therefore a greater statistical chance of encountering a molten droplet. The result of this collision is either a small salt-glass bead agglomerate or a discrete salt particle, depending on local bed properties such as airflow and temperature. The only time during operation when the free glass beads are not greater in number is when the bed has received a molten feed for a significant amount of time, which in the present study is approximately 15-20 minutes. In this case, the reduced number of free glass beads allows agglomerates to encounter molten feed, resulting in agglomerate growth. Eventually the agglomerate will grow excessively large, and cause defluidization of the bed. Figure 5.16 (c) is a photograph of a bed that has defluidized due to this reason.

5.2.3 Air Flowrate

The third variable studied was air flowrate, and the results are given in Figures 5.17 to 5.19. The model predicted a positive linear relationship between the gas to particle heat transfer coefficient and the air flowrate. The experimental curves generally have positive slopes and some curvature, although two sets of data have negative slopes (1.22g/min salt with 125g bed and 1.86g/min salt with 150g bed), only the former is significantly large. Correlation between the experimental and the predicted values is greater at higher air flowrates and larger bed masses. This trend is seen in Table 5.6.

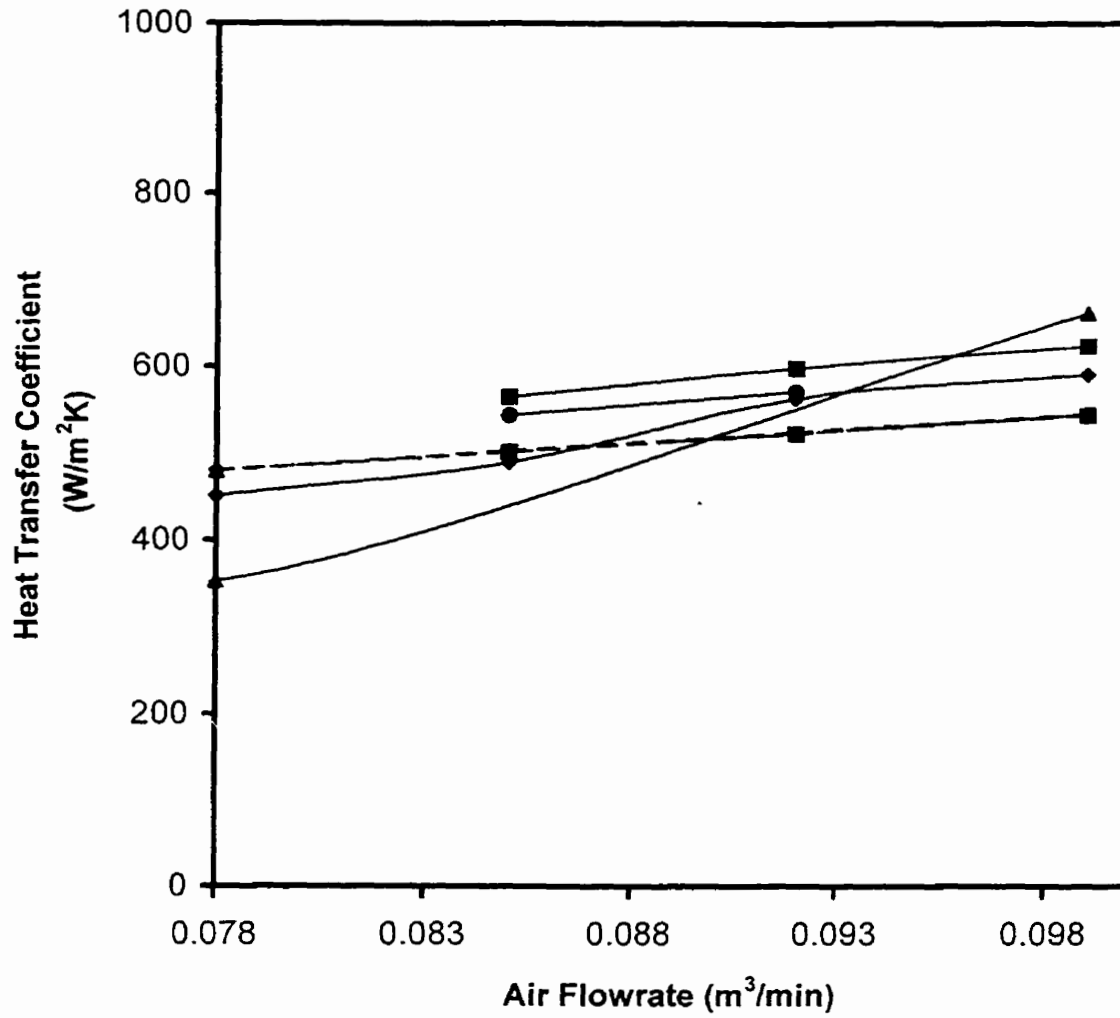


Figure 5.17 The gas to particle heat transfer coefficient as a function of the air flowrate for various molten salt feedrates. The fluidized bed had an initial mass of 100g. The solid curves represent experimental data while the dashed curves are the values predicted by the Excel algorithm. The molten salt feedrates are 1.18g/min (◆), 1.86g/min (▲), 2.01g/min (●), and 2.32g/min (■).

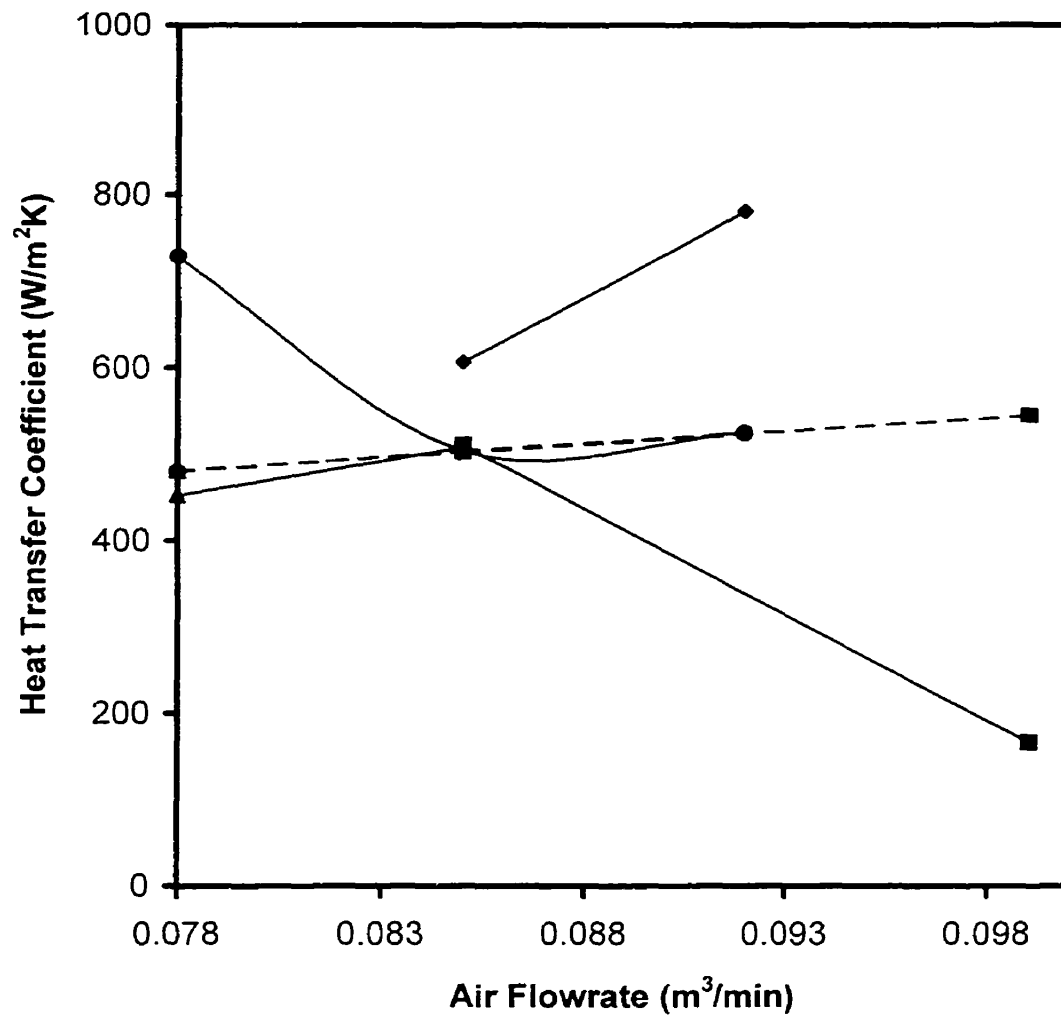


Figure 5.18 The gas to particle heat transfer coefficient as a function of the air flowrate for various molten salt feedrates. The fluidized bed had an initial mass of 125g. The solid curves represent experimental data while the dashed curves are the values predicted by the Excel algorithm. The molten salt feedrates are 0.65g/min (◆), 0.86g/min (▲), 1.22g/min (●), and 1.52g/min (■).

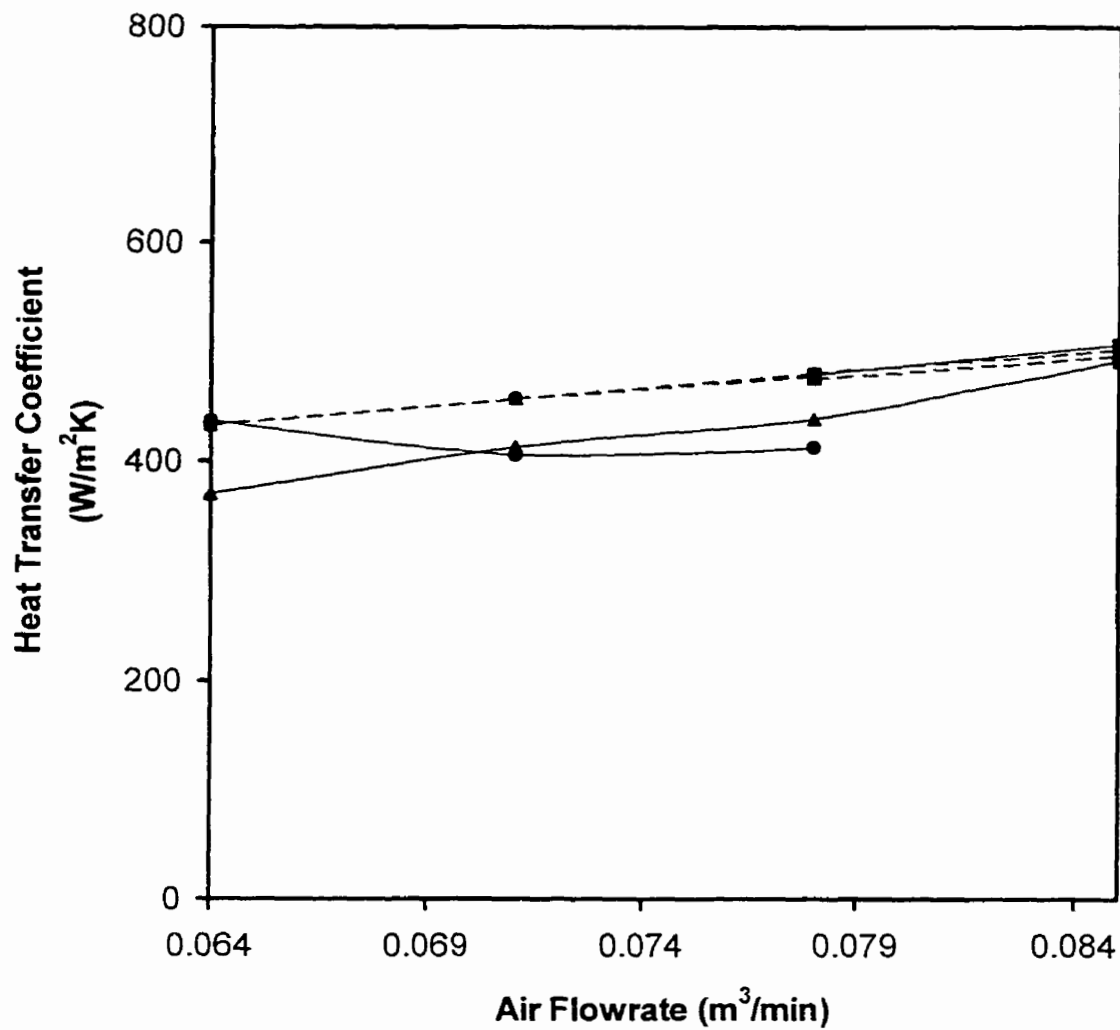


Figure 5.19 The gas to particle heat transfer coefficient as a function of the air flowrate for various molten salt feedrates. The fluidized bed had an initial mass of 150g. The solid curves represent experimental data while the dashed curves are the values predicted by the Excel algorithm. The molten salt feedrates are 0.89g/min (▲), 1.86g/min (●), and 4.9g/min (■).

Table 5.6. Correlation between the actual and the predicted gas to particle heat transfer coefficients. The values shown in the table are the percentage differences between the actual and the predicted values.

Bed Mass (g)	Low Air flowrate	High Air flowrate
100	12.4	13.5
125	26.1	16.7
150	7.8	2.4

The Excel model predicts that the gas to particle heat transfer coefficient will increase with air flowrate. This is consistent with the expression used for the Nusselt number, which is a function of the Reynold's number. The Reynold's number is proportional to the air velocity in the bed, and an increase in air flowrate will result in an increase in the gas to particle heat transfer coefficient. This increase is predicted to be independent of the salt feedrate and bed mass.

Analysis of Figures 5.17 to 5.19 shows that there is better agreement between the actual and the predicted gas to particle heat transfer coefficients at higher air flowrates than at lower air flowrates. This observation can be explained via the following argument. The solidifying molten droplets experience two thermal driving forces upon entering the bed: (1) heat is transferred from the salt to the bed particles and then to the fluidizing air, or directly to the air; (2) heat is transferred from the salt to the bed particles and then to immersed surfaces, or directly to immersed surfaces.

The first driving force represents the gas to particle heat transfer coefficient, while the second represents the heat loss term as discussed in Section 3.2.4. At low air flowrates, the fluidization is complete but less intense than at higher flowrates. The absence of adequate air in the bed reduces mixing. As a result, the total amount of heat removed from the bed by the air is decreased, and the heat removal is not as efficient.

In all the experiments, the position of the molten salt feeder was kept constant so that the impact point of the molten droplets was always at the same location in the bed. This fact combined with the small scale of the reactor and the lack of adequate mixing, leads to the generation of significant thermal gradients along the radial axis of the fluid bed. As a result, the centre of the bed remains hotter than the relatively cooler edges and walls. Consequently, a disparity in thermal driving forces results, which causes heat to be preferentially transferred radially outwards from the impact point of the molten salt to the wall of the reactor. This heat is lost to the surroundings. At higher air flowrates, the bed is fluidized more intensely, which enhances mixing. The temperature gradient becomes less steep, and the thermal driving forces equilibrate. Overall, less heat is lost to the reactor wall and the other internals, and more heat is recovered by the fluidizing air. According to Equation (5.4.1), if the gas recovers more heat, then the gas to particle heat transfer coefficient must increase if all other parameters are kept constant. Alternatively, if more heat is lost to the surroundings, then the air absorbs less heat and the gas to particle heat transfer coefficient is reduced.

Figure 5.20 shows the correlation between the gas to particle heat transfer coefficient and the heat recovery efficiency, which is defined as the ratio of total heat recovered by the fluidizing air to the total heat released by the molten salt expressed as a percent. A smaller value is indicative of greater heat losses. The slight offset in heat recovery efficiencies in Figure 5.20 is due to small differences in the salt feedrates for the two cases.

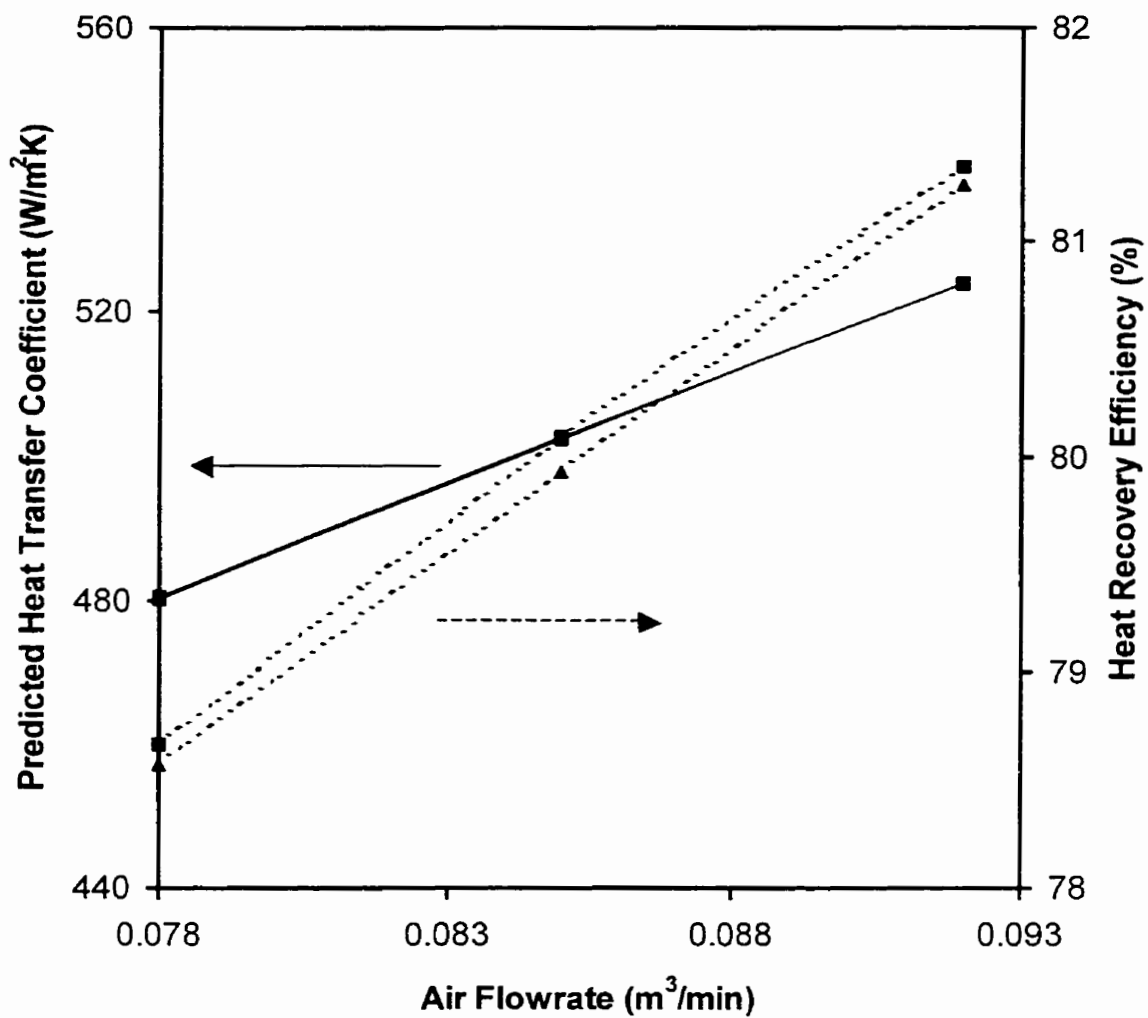


Figure 5.20 Correlation between the predicted gas to particle heat transfer coefficient (solid lines) and the heat recovery efficiency (dashed lines) (■ indicates 100g bed and 1.18g/min salt feedrate; ▲ indicates 125g bed and 1.22g/min salt feedrate).

Since the thermal driving force for heat transfer from the molten salt to the walls decreases rapidly with an increase in the fluidization intensity and the overall mixing in the bed, then it would be expected that the heat recovery efficiency would increase as the fluidization intensity increased. These conditions can be achieved with a high bed mass to promote slugging (as discussed in Section 5.4.1) and by increasing the air flowrate, as shown in Figure 5.21.

In Figure 5.21, the heat recovery is correlated with the gas to particle heat transfer coefficient, which are both functions of air flowrate. At higher air flowrates, the heat recovery is enhanced since the losses are minimized. Thus the measured heat transfer coefficient at higher air flowrates is more accurate, and thus the actual and the predicted coefficients are in better agreement at higher air flowrates. Furthermore, the results presented in Figure 5.21 agree with the information presented by Levenspiel, who observed that heat transfer is more efficient in spouted bed systems than in moving and slightly bubbling beds (Kunii and Levenspiel, 1991). This observation is clearly shown in Figure 5.21. When the air flowrate is increased by 9%, the spouting nature and mixing intensity of the 150g bed is greatly increased, and this results in a 9% increase in the heat transfer efficiency.

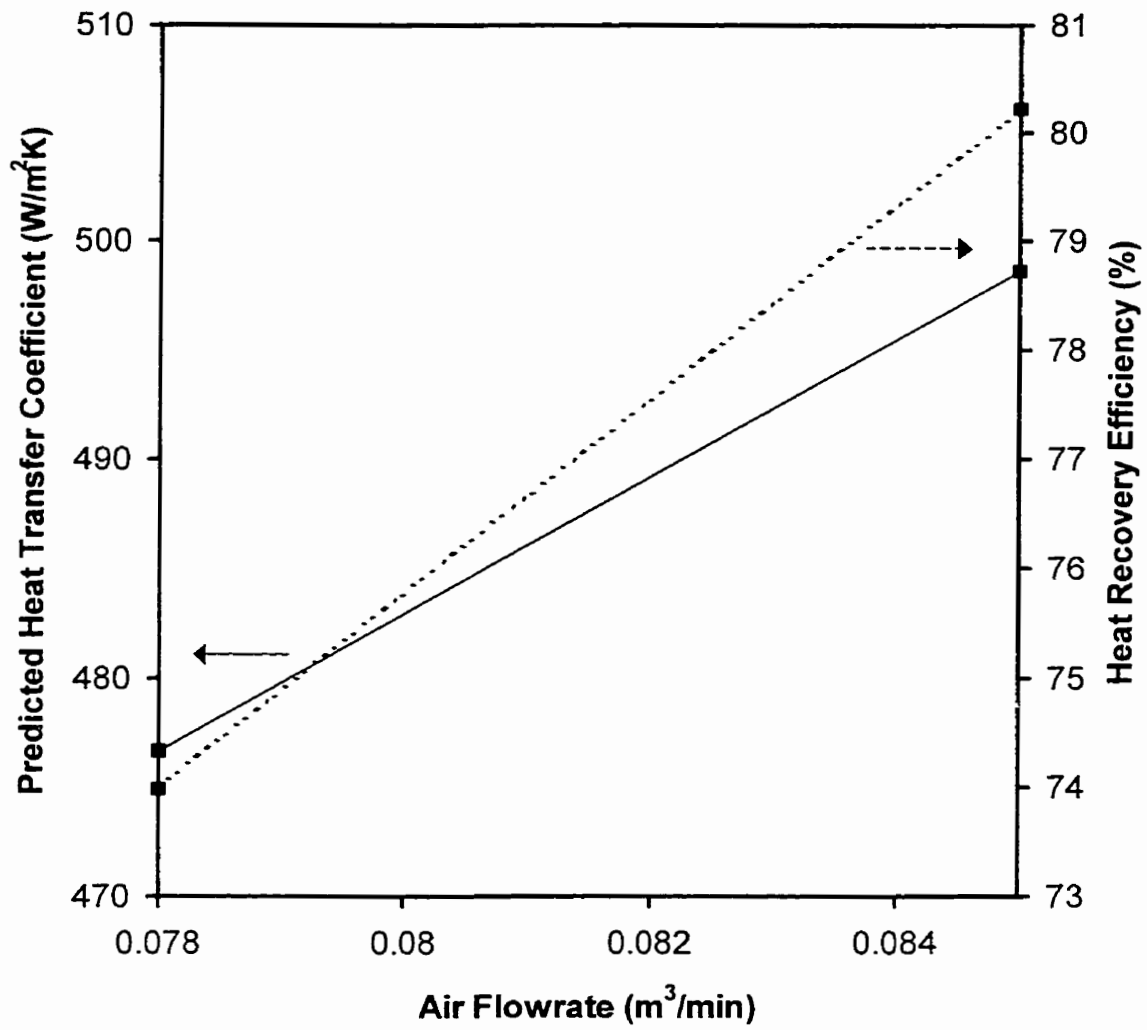


Figure 5.21 Correlation between the predicted gas to particle heat transfer coefficient (solid line) and the heat recovery efficiency (dashed line) for a slugging bed.

5.3 Industrial Considerations

The amount of heat available for recovery from blast furnace slag is large. A typical 4 Mt/yr integrated steel mill uses approximately 24 GJ per ton of steel produced, 2-3% of which is transferred to the blast furnace slag. If all this heat is recovered, then it can be used as an alternative source of energy. This means that emissions reductions can be realized with a simultaneous economic gain. Figure 5.22 depicts this scenario assuming that the recovered heat reduces the amount of natural gas fired in the steelmaking facility (commercially available at \$296/ton).

Taken in the context of the 4 Mt/yr facility, Figure 5.22 indicates that the total carbon dioxide emissions can be reduced by $10^4 - 10^5$ ton/yr. The emissions are reduced because the recovered heat can be substituted for heat which otherwise would have to be generated by burning a carbon-based fuel (assumed in this discussion to be natural gas). This reduced fuel requirement has an economic benefit in the range of $\$10^6 - \10^7 annual monetary savings. Recovered heat can be used to preheat combustion gases, or to drive turbines providing a constant and competitive source of electricity.

The recovery of heat from blast furnace slag is advantageous both economically and environmentally. However, the results of this study into fluidized bed heat recovery from blast furnace slag have shown that the process needs more development. Throughputs in this research range from $0.5 \text{ kg/m}^2\text{min} - 3.9 \text{ kg/m}^2\text{min}$, depending on the air flowrate and the initial bed mass. These values do not compare favorably with other fluidized bed operations in the metallurgical field that achieve throughputs on the order of $15 \text{ kg/m}^2\text{min}$.

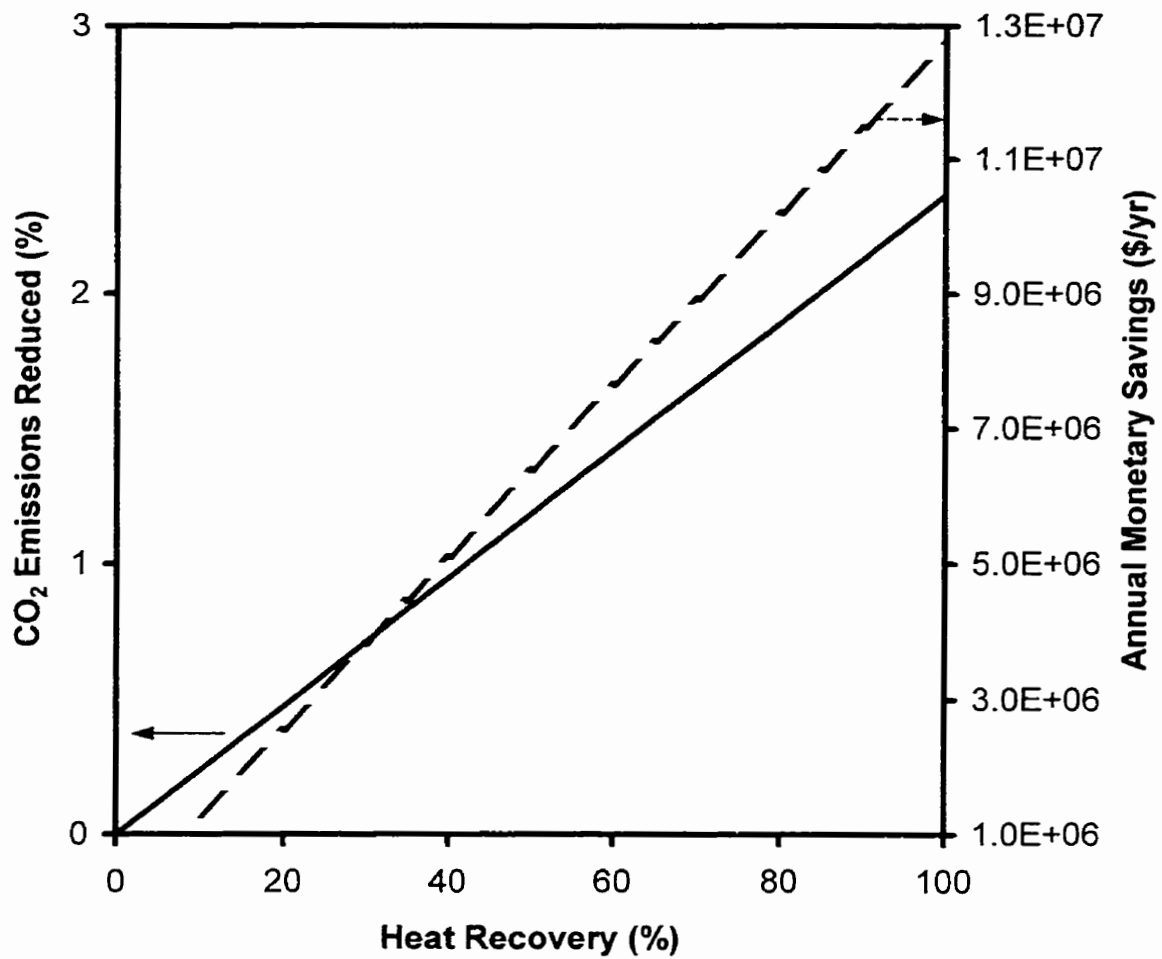


Figure 5.22 Emission reductions and economic gain with heat recovery from blast furnace slag. The dashed line represents annual monetary savings, and the solid line represents carbon dioxide emission reductions.

Industrial production rates of blast furnace slag are on the order of 1 ton of slag for every 3 tons of steel. A facility such as the one mentioned above producing 4 Mt/yr of steel would produce approximately 2500 kg/min of blast furnace slag. In order to handle this flowrate, nearly 5000 m² of reactor area would be required at a throughput of 0.5 kg/m²min. This value would be substantially reduced to 650 m² of reactor area at the high end of the throughputs observed in this study. If the fluidized bed system was operating with an industrial throughput of 15 kg/minm², 170 m² of reactor area would be required. Clearly, the throughput of the fluidized bed system used in this study needs to be increased before useful applications can be made.

The main parameter limiting the throughput of the fluidized bed was the ratio of the amount of molten salt feed material to bed solids. This is evident by examining the maximum molten flowrate possible for different systems: 2.44g/min for 100g beds, 1.52g/min for 125g beds, and 4.90g/min for 150g beds. If the value for 125g beds is ignored based on the fluidization transition zone theory, it can be seen that the proportion of molten material increases from 2.5% in the 100g bed to 3% in the 150g bed. Industrial fluidized beds can operate with 5-7% molten material in the reactor, which leads to an increased throughput. In this study, it was not possible to have enough bed mass to allow for 5-7% molten material in the bed due to the reactor size. For masses greater than 150g, the slugging nature of the fluidized bed would cause significant bed material and product to overflow the top of the reactor. In this regard, a 100mm or 200mm fluidized bed would have been suitable. Even with a larger size reactor, it would be necessary to process material continuously rather than batch. This would allow for higher throughputs, as well as for continuous removal of material. As a result, a bed with a larger mass could be operated in a slugging mode, and the overflow of material would be

handled using a cyclone and other downstream gas-handling equipment. Large slag particles could be captured and cooled in a hopper, while the fines would be recycled to the reactor for further agglomeration.

Furthermore, in order to feed sufficient molten material into the reactor to achieve higher throughputs, it is advantageous to use multiple feeding ports. In this way, the chance of defluidization due to the overloading and the solidification of molten material in one area of the bed is minimized. This is difficult to achieve in the reactor used in this study. In order to avoid defluidization of the bed due to local molten solidification, the feeding tube diameter had to be extremely small. The quartz feed tube used in this study was approximately 700 μm in internal diameter, and could not be made smaller. If multiple tubes were to be used, the total flow would become too large, and the bed would defluidize. Industrially, the diameter of the feeding tubes could be adjusted, but due to the scale in this study, this could not be done. In addition, there was physically not enough room around the top of the reactor to allow for multiple feeding tubes. The use of a 100mm or 200mm fluidized bed would alleviate both of these problems.

Thirdly, the use of a larger fluidized bed would eliminate the thermal and the fluid mechanical wall effects. In the studied system, the bed diameter was sufficiently small and therefore the heat losses through the wall were significantly large. As well, despite the high degree of mixing in a fluidized bed, there always exists an air velocity profile. The velocity of air is zero at the walls, reaches a maximum in the center. The small reactor used in this study most likely had only a small fraction of the bed fluidized by air at the maximum velocity. The fluidization characteristics of the bed would have been greatly affected by the proximity of the particles to the wall, and thus a lowered air velocity. This problem would not occur to such a drastic degree in a 100mm or 200mm

fluidized bed, which could employ tuyeres to ensure even air distribution across the diameter of the bed.

Alternatively, if the throughput and the heat recovery of the fluidized bed is limited by the amount of molten material that can be present in the bed, then the feed to the bed could be pre-cooled so that hot solids instead of molten material are fed to the bed. This possibility raises a number of design issues. The throughput of the heat recovery system would definitely be increased. The molten content of the bed would no longer be the limiting factor, and the solids fed to the bed would experience high rates of efficient heat transfer. Levenspiel has demonstrated that small, cold spherical particles, when dropped into a fluidized bed, will quickly heat to the temperature of the bed. For example, particles of 100 μm diameter will reach a temperature within 1% of that of the bed in less than 0.4 s residence time. Although the particles of molten material would be much larger, the required time to reach thermal equilibrium remains small (it is unimportant whether a cold sphere is to be heated or a hot sphere to be cooled). Figure 5.23 below depicts a relationship modeled in Excel between particle size and the time required for a hot particle to cool to within 1% of the bed temperature.

Despite the efficient and fast heat transfer between the solid sphere and the fluidized bed system, there is a fundamental problem creating solid spheres from molten material. In this study, the heat of fusion of the salt represented approximately 43% of the total heat available for recovery. The remaining 57% was represented by the sensible heat of the salt; 23% of this due to cooling above the liquidus to the eutectic point, and

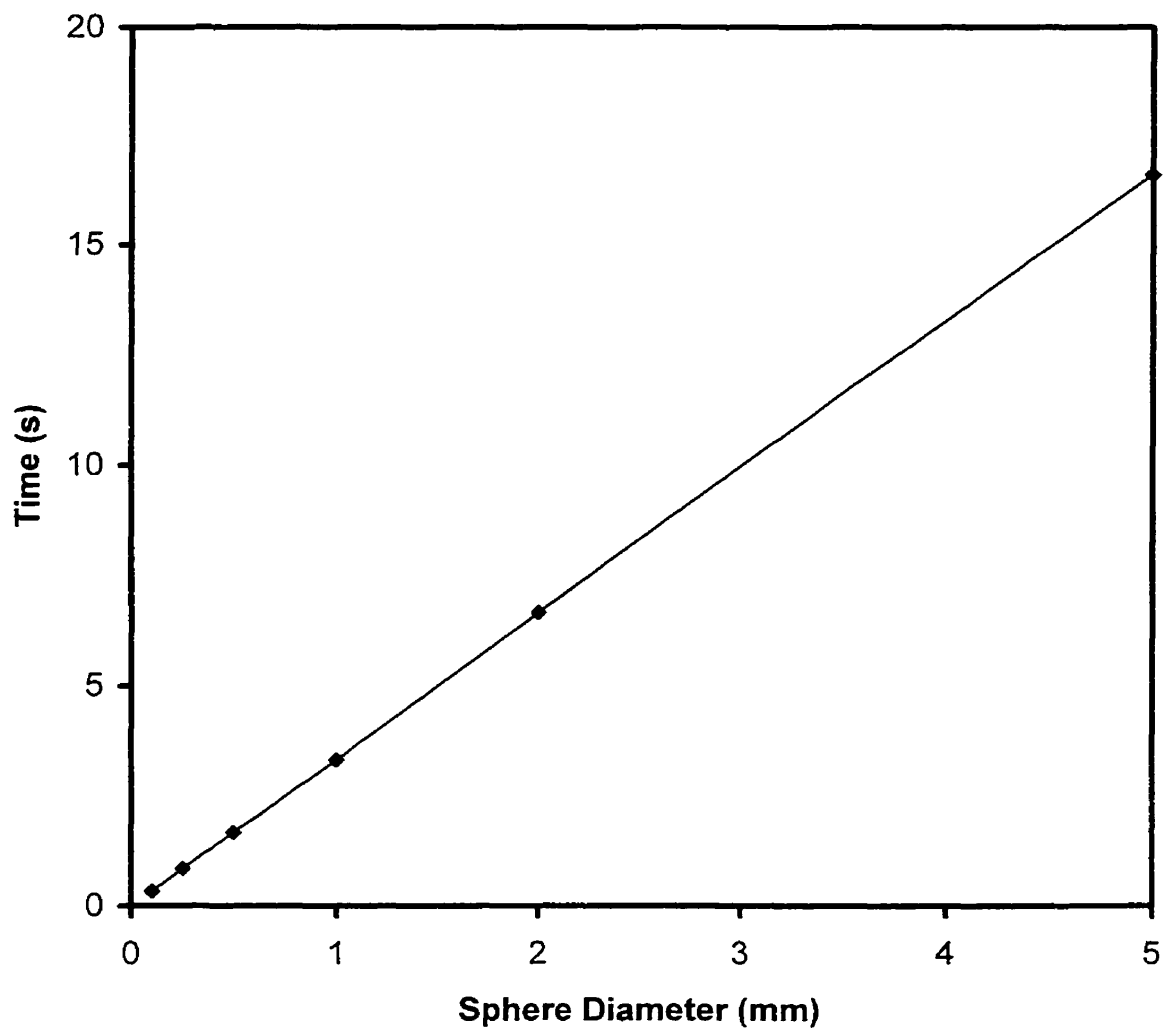


Figure 5.23 Time required for solid spheres to reach within 1% of the fluidized bed operating temperature for the system used in this study. The modeled system has a bed mass of 150g, an air flowrate of $0.085\text{m}^3/\text{min}$, an inlet air temperature of 298K, and an initial sphere temperature of 723K.

the balance due to cooling from the eutectic point to ambient conditions. Therefore, if solid spheres are to be fed to the fluidized bed, then the heat recovery system will be capable of recovering merely 57% of the total available heat. The heat of fusion of the molten material, as well as the sensible heat due to superheat above the liquidus temperature, must be recovered in the process that produces the solid spheres. Currently there is no process capable of doing this on an industrial scale. However, the rotary cup air blast atomizer depicted in Chapter 2 could theoretically recover this heat (i.e. superheat above the liquidus and the heat of fusion) as the air blast formed the solid spheres from the droplets. However, the high air velocities required for successful atomization of viscous molten material would produce a high volume of air with a low quality heat. Tall cooling columns placed above the fluidized bed feed mechanism could be used. In this way, molten material would experience a long free-fall, during which cooling would occur and the molten stream would break up into droplets and solidify as spheres. However, if the molten flowrate were too large, sufficient break up would not occur and the molten material would not freeze into discrete spheres. This would likely represent a process bottleneck and reduce the throughput of the fluidized bed system, since the heat transfer would be less efficient. Furthermore, the high volume of air required for the column would produce a low quality heat in a situation similar to the rotary cup air blast atomizer unit. Finally, a tall cooling column would have a significant capital cost, and its size might prove to be excessive in some installations.

The last issue regarding this heat recovery mechanism is the changes incurred to the system if slag were used instead of molten salt as the heat source. Blast furnace slag has a viscosity of 0.3-2.0 N/sm² whereas the LiCl-KCl melt used in this study had a viscosity on the order of 0.003 N/sm². This dramatic increase in viscosity would change

the properties of droplet formation in the quartz feeder; most likely a much larger aperture would be required. The increased viscosity may also lead to an increased chance of defluidization in the bed when molten material is present. In order to counteract this occurrence, higher air flowrates may be required; if so, the heat recovered by the air would have a lower quality. Also, for the LiCl-KCl melt, the eutectic composition was chosen, and slag, when tapped, would almost certainly be of a non-eutectic composition. As a result, a solid phase will be present upon cooling below the liquids temperature. The presence of these solid particles in the droplets fed to the fluidized bed would yield a highly complex system requiring more investigation. However, it is likely that discrete nucleation and the growth of solids would occur at the droplet surface as the molten droplet falls from the feeder to the fluidized bed.

Overall, it is evident that the small-scale fluidized bed heat recovery system used in this study was not capable of industrial throughputs. It is unclear if this is a result of the nature of the system or the scale on which the study was performed. The use of a 100mm or 200mm fluidized bed would allow for multiple feeding tubes, and a greater surface area to determine if this process could be viable on an industrial level.

6.0 Conclusion and Recommendations

The findings of this study on heat recovery from blast furnace slag in a fluidized bed using a low temperature analogue consisting of a LiCl-KCl eutectic salt melt are summarized below.

1. Simulations performed by the computer model indicate that the following parameters are important to the gas to particle heat transfer coefficient:
 - Dimensionless air velocity;
 - Density of bed particles;
 - Air pressure.

An increase in any of these variables will result in a significant increase in the fluid bed heat transfer.

2. A critical bed mass exists below which smooth, stable fluidization is not possible; for the system studied, this mass was 100g. As the bed mass is increased, fluidization characteristics change dramatically from smooth fluidization at 100g, to unstable bubbling and slugging at 125g, to stable and predictable slugging at 150g. As the bed mass is increased to promote slugging, less air is required for fluidization.
3. The heat recovery efficiency is approximately constant for the 100g and the 125g systems, and is in the range of 78 to 82%. For beds of 150g mass, the heat recovery efficiency is slightly lower, ranging from 65 to 80%. The lower efficiency values are a result of the lower air requirements for fluidization due to operation in the slugging regime; this reduces the gas to particle heat transfer coefficient.
4. The physical properties of the bed in this study change significantly with time. As a result of particle growth, granulation, and agglomeration phenomena, the gas to

particle heat transfer coefficient deviates from the predicted values particularly for data sets measured after ten minutes of experimentation. This phenomenon occurs because the bed mass changes, which results in operation in a different fluidization regime. Further studies should model the advanced fluid mechanics, particularly particle growth and agglomeration and their effect on the gas to particle heat transfer coefficient.

5. Varying the salt feedrate and the bed mass showed that the bed mass does not directly have an effect on the gas to particle heat transfer coefficient in the fluidized bed. Rather, altering the bed mass, either initially or over time through molten salt additions, changes the regime of fluidization. The highest heat recovery is achieved in a slugging fluidization regime.
6. Severe temperature gradients due to wall effects are induced as the air flowrate is decreased. As a result, the heat recovery efficiency is strongly correlated with the gas to particle heat transfer coefficient; both of which are functions of air flowrate.
7. Differences between the actual and the predicted gas to particle heat transfer coefficient decreases with increasing air flowrate, salt feedrate, and bed mass. The differences are a function of time due to temporal changes in the fluid mechanics which were not modeled by the computer simulation.
8. With respect to scale-up, a slugging bed in a large diameter reactor should be operated with as high a specific molten throughput as possible. The slag would be injected in multiple ports to uniformly distribute the molten feed, and discourage thermal gradients. The reactor would be run continuously in contrast to the batch operation in this study. Bed solids would be continually drawn off and classified in a cyclone. Cooled slag particles of a certain size fraction would be removed from the

system and sent to a storage hopper for use as an aggregate in asphalt, while particles suitable for reuse as bed material would be recycled to the fluid bed. In this process, the bed size would be kept constant, and thus changes in fluidization regimes and the gas to particle heat transfer coefficient would be avoided. The use of gas cleaning equipment for the off-gas downstream of the reactor would allow for operation of a uniformly slugging bed. This would eliminate thermal gradients along the radius of the reactor, and enhance particle mixing.

7.0 Literature Citations

Bacon, D: Participant Guide: Design of Experiments for Engineers Workshops Module One – Introduction to Design of Experiments. Unpublished notes for Chemical Engineering, course no. CHEE 418, Department of Chemical Engineering, Queen's University at Kingston (1992)

Becker, H.A.: Thesis Manual. Queen's University at Kingston (1969)

Berry, B.: Hoogovens means blast furnaces - and clean air. New Steel. 26 (1994)

Bisio, G.: Energy Recovery from Molten Slag and Exploitation of the Recovered Energy. Energy. 22, 501 (1997)

Botterill, J.S.M.: Fluid-Bed Heat Transfer: Gas-fluidized bed behaviour and its influence on bed thermal properties. Academic Press (1975)

Broadbent, C.P., and Warner, N.A.: Self-impinging Jet Disintegration of Slag for Energy Recovery. Transactions of the Institution of Mining and Metallurgy C: Mineral Processing and Extractive Metallurgy. 93, C130 (1984)

Brockner, W., Torklep, K., and Oye, H.A.: Viscosity of Molten Alkali Chlorides. Journal of Chemical Engineering Data. 26, 250 (1981)

Butov, A.I., Nevmerzhitkii, E.V., and Stepanov, V.P.: Problems in the Granulation of Blast-furnace Slag at the Combine. Metallurgist (USSR). 33, 129 (1990)

Campy, D., Eaves, T., Grudzinski, E.M., and Worthington, H.E.C.: Scale-up Considerations in Fluidized Bed Granulation: Air Flowrates and Air Pressure Distribution. Journal of Pharmaceuticals and Pharmacology. 26 Supplement, 76P (1974)

Davidson, J.F., Clift, R., and Harrison, D.,ed.: Fluidization. (Second Edition) Academic Press, Inc (1985)

Davies, W.L., and W.T. Gloor, Jr.: Batch Production of Pharmaceutical Granulations in a Fluidized Bed I: Effects of Process Variables on Physical Properties of Final Granulation. Journal of Pharmaceutical Sciences. 60, 1869 (1971)

Donald, J.R. and Pickles, C.A.: Energy Recovery from Molten Ferrous Slags Using a Molten Salt Medium. 77th Steelmaking Proceedings, p.681. The Iron and Steel Society, Warrendale, PA (1994)

Elchardus, E., and Laffitte, P. Bull.soc.chim. 51, 1572 (1932)

Fan, L.: Gas-Liquid-Solid Fluidization Engineering. Butterworths (1989)

Featherstone, W. B. and Holliday, K. A.: Slag Treatment Improvement by Dry Granulation. Iron and Steel Engineer. 19, 42 (1998)

Forrest, D.: Global Warming and the Primary Metals Industry. Journal of Metals. 23 (1990)

Goossens, W.R.A., Dumont, G.L., Spaepen, G.L. Chemical Engineering Progress, Symposium Series. 67, (1971)

Gudenau, H.W., Lindner, K., and Peters, K. Slag Heat Recovery. Stahl u. Eisen. 23, 57 (1986)

Incropera, F.P. and DeWitt, D.P.: Introduction to Heat Transfer. Wiley (1996)

Kasau, E., Kitajima, T., Akiyama, T., Yagi, J., Saito, F.: Rate of Methane-Steam Reforming Reaction on the Surface of Molten Blast Furnace Slag for Heat Recovery from Molten Slag by Using a Chemical Reaction.: ISIJ International. 37, 1031 (1997)

Kono, H: A New Concept for Three-phase Fluidized Beds. Hydrocarbon Processing. 83, 123 (1980)

Kunii, D., and Levenspiel, O.: Fluidization Engineering. (Second Edition) Butterworth-Heinemann (1991)

Lee, A.R.: Blast Furnace and Steel Slag: Production, Properties, and Uses. Edward Arnold (1974)

Lopez, F.A., Sainz, E., and Formoso, A.: Use of Granulated Blast Furnace Slag for Stabilisation of Steelmaking Flue Dust. Ironmaking and Steelmaking. 20, 293 (1993)

Lupis, C.H.P.: Greenhouse Gases and the Metallurgical Process Industry. Metallurgical and Materials Transactions B. 841 (1999)

Mamantov, G, ed.: Molten Salts: Characterization and Analysis. Marcel Dekker (1969)

Martocci, A.P.: Energy: Consumption, cost and conservation in the steel industry. Iron and Steel Engineer. 47 (1996)

Nagasawa, T.: How the Japanese Steel Industry is Addressing Global Environmental Problems. Energy Conservation and Management. 36, 843 (1996)

Norris, T.: <http://www.canadiansteel.ca/products/products01.html>. (1999).

Pickering, S.J., Hay, N., Roylance, T.F., and Thomas, G.H.: New Process for Dry Granulation and Heat Recovery from Molten Blast-furnace Slag. Ironmaking and Steelmaking. 12, 14 (1985)

Richardson, M.C.R., Rees, J.E., and Sendall, F.: Evaluation of a Small Scale Fluidized Bed Granulation Unit. Journal of Pharmaceuticals and Pharmacology. 27 Supplement, 80P (1975)

Schaafsma, S.H., Kossen, N.W.F., Mos, M.T., Blauw, L., and Hoffmann, A.C.: Effects and Control of Humidity and Particle Mixing in Fluid Bed Granulation. American Institute of Chemical Engineering Journal. 45, 1202 (1999)

Schmidt, H.: Blast Furnace Slag Heat Recovery. Stahl und Eisen. (1998)

Sharkey, A.G.: Energy-Efficiency Collaborative Research as a Component of a National Energy Policy to Address Global Climate Change.
<http://www.steel.org/policy/environment/statements.asp>. (1998)

Wakao, N., Kaguei, S., and Funazkri, T.: Effect of Fluid Dispersion Coefficients on Particle to Fluid Heat Transfer in Packed Beds. Chemical Engineering Science. 34 (1979)

Appendix A

Computer Model And Modeling and Experimental Data

Fluid Properties

MWair= 29 g/mol

Pinitial=	151988	Pa
Ta,i=	298	K
ρ =	1.779	kg/m ³
μ =	1.85E-05	Pas
cp=	1002	J/kgK
k=	2.62E-02	W/mK
Pr=	0.705	

Pbed=	101325	Pa
Ta,b=	376.23	K
ρ =	0.939	kg/m ³
μ =	2.74E-05	Pas
cp=	1014	J/kgK
k=	4.17E-02	W/mK
Pr=	0.667	

Bed->Initial

Pavg=	126656.5	Pa
Tavg=	337.1142	K
ρ =	1.359	kg/m ³
μ =	2.294E-05	Pas
cp=	1008	J/kgK
k=	0.033965	W/mK
Pr=	0.686	

Calculation of Minimum Fluidization Velocity:

Ga=	34.43
Mv=	1176.15
Umf=	0.322411516 m/s
Uo/Umf=	1.49

Air Flowrate=	1.28 SCFM
Air Flowrate=	1.28 ACFM
Air Flowrate=	0.0370584 mol/s
Air Flowrate=	0.0010747 kg/s
Air Velocity=	0.481 m/s
	1.5772175 AFPS

Salt Properties

MW LiCl= 42.3937 g/mol

Ts,i=	973	K
ρ =	1463	kg/m ³
μ =	1.152E-03	Pas
cp=	1412	J/kgK
k=	0.600	W/mK
Pr=	2.71	

Ts,b=	951.8	K
ρ =	1472	kg/m ³
μ =	1.214E-03	Pas
cp=	1405	J/kgK
k=	0.606	W/mK
Pr=	2.82	

MW KCl= 74.551 g/mol

Ts,i=	973	K
ρ =	1569	kg/m ³
μ =	1.364E-03	Pas
cp=	898	J/kgK
k=	0.401	W/mK
Pr=	3.05	

Ts,b=	952	K
ρ =	1581	kg/m ³
μ =	1.461E-03	Pas
cp=	898	J/kgK
k=	0.404	W/mK
Pr=	3.24	

Binary Properties

MWbinary= 61.476 g/mol

nLiCl=	0.4066	%mol/mol
nKCl=	0.5934	%mol/mol
xLiCl=	0.45	%wt/wt
xKCl=	0.55	%wt/wt

ΔH_{fusion} =	367624.083	J/kg
Teut=	625	K

Ts,i=	973	K
ρ =	1521	kg/m ³
μ =	1.269E-03	Pas
cp=	1129.338847	J/kgK
k=	0.490	W/mK
Pr=	2.92	

Ts,b=	951.82712	K
ρ =	1532	kg/m ³
μ =	1.350E-03	Pas
cp=	1126.1417	J/kgK
k=	0.495	W/mK
Pr=	3.07	

Tavg=	962.41356	K
ρ =	1527	kg/m ³
μ =	1.309E-03	Pas
cp=	1127.7403	J/kgK
k=	0.493	W/mK
Pr=	3.00	

Binary Flowrate=	5 g/min
Binary Flowrate=	8.333E-05 kg/s

Bed Properties

Twall=	298	K
Dparticle,avg=	1.00E-03	m
Dbed=	4.00E-02	m
XAbed=	0.00126	m ²
Mass Bed=	0.2	kg
$\rho_{\text{bed particles}}$ =	1600	kg/m ³
Nparticles in bed=	2.39E+05	
Aeff,bed, max=	0.75000	m ²
Correction Factor to Aeff,bed,max=	0.00463	
A*eff,bed=	0.00347	m ²
Expanded Bed Height=	7.62E-02	m
Alosses=	9.58E-03	m ²
Min=	0.00100	
Max=	1.50000	

HT From Falling Molten Droplet to 'Atomizing' Air

Ddrop=	2.0000E-03	m
Terminal Velocity=	120.8	m/s
Re=	56.96051017	—
Nu=	5.993531007	—
h=	101.7851403	W/m ² K
Bi=	0.00405389	— (Bi<<0.1 for lumped capacitance model to be valid)

HT From Fluidized Bed to Fluidizing Air

Re=	28.48025509	— (0.1<Re<100 is applicable range)
Nu=	9.169307773	—
h=	311.44	

Heat Losses

A. To Reactor Wall and Distributor

Re=	28.48025509	—		
Nu=	1.597220559			Both from EQN 13.21 p. 444 from Davidson
h=	54.25	W/m ² K		
Aloss=	0.01117	m ²		
Losses=	47.40889269	W	Total Losses=	51.172 W

B. To TC Tube

Re=	28.48025509	—
Nu=	1.597220559	
h=	54.25	W/m ² K
Aloss=	0.000886712	m ²
Losses=	3.763080857	W

1. Determine Tsb and in-flight heat transfer.

Drop Height=	0.2032	m
Drop Time=	0.20	s
Drop Time Required to Reach Eutectic Temperature=		
Drop Time Required to Reach Bed Temperature=		
Ts,b=	951.8	K
Adrop=	0.000012566	m ²
Vdrop=	4.18867E-09	m ³
Ndrops=	13.08	drops/s
Heat Gained by Air=	1.989792603	W
Heat Released by Salt=	1.989721647	W
Atomizing Balance=	2.55351E-14	W

2. Determine Tbed and Ta,e.

Tbed=	376.23	K	103.08 °C	Tinfinity=	377.14
Ta,e=	378.05	K	104.90 °C		
Bed Balance1=	0.00	W	(uses htc for air)		
Bed Balance2=	0.00	W	(uses mass flow for air)		
Total Qgained by air=	86.7069695	W			
Total Qreleased by salt=	86.72			Qfusion=	30.635 W
Heat Recovery Efficiency	99.99				
Overall Balance=	-0.59	W			
Approx. Time Required for Salt to Reach Tbed=	8.50	s	(eqn from p.274 levenspiel)		
1. Max Heat Gained by Air=	84.73		} in bed		
2. HTC Heat Gained by Air=	84.65				
1-2=Heat Transfer Efficiency=	0.92				

Bed Mass (g)	Salt Flow (g/min)	Air Flow (scfm)	Air Flow (m ³ /s)	ACTUAL		PREDICTED		ACTUAL		PREDICTED		ACTUAL hbed (W/m ² K)	PREDICTED hbed (W/m ² K)	HR Eff (%)
				Tbed (K)	T exh (K)	Tbed (K)	T exh (K)	ΔTbed (K)	ΔT exh (K)	ΔTbed (K)	ΔT exh (K)			
100	1.18	2.75	0.07787	304.95	305.45	304.53	304.68	5.5	5.5	4.8	5.0	450.7	480.4	78.7
	1.18	3	0.08495	304.15	305.65	304.20	304.35	4.7	5.7	4.5	4.7	488.9	502.6	80.1
	1.18	3.25	0.09203	303.45	304.65	303.92	304.06	4.0	4.7	4.2	4.4	563.3	524.1	81.3
	1.18	3.5	0.09911	303.15	304.95	303.67	303.81	3.7	5.0	4.0	4.1	590.9	544.9	82.4
	1.86	2.5	0.07079	305.35	307.15	307.56	307.82	6.3	7.5	8.2	8.4	478.3	456.6	77.0
	1.86	2.75	0.07787	306.65	307.15	306.98	307.23	5.3	6.8	7.6	7.8	353.3	479.6	78.7
	1.86	3.5	0.09911	304.45	306.45	305.65	305.86	7.5	7.5	6.2	6.5	662.0	544.2	82.5
	2.01	3	0.08495	302.15	302.45	306.05	306.30	4.0	3.8	7.7	7.9	543.4	501.6	80.1
	2.01	3.25	0.09203	301.65	303.65	305.58	305.82	3.5	5.0	7.2	7.4	571.1	523.1	81.3
	2.32	3.25	0.08495	302.65	304.45	306.97	307.26	5.0	5.8	8.8	9.1	564.9	501.3	80.1
	2.32	3.5	0.09203	302.15	301.65	306.42	306.70	4.5	3.0	8.3	8.5	598.1	522.8	81.3
	2.32	3.5	0.09911	302.15	303.45	305.94	306.20	4.5	4.8	7.8	8.1	624.1	543.6	82.4
	2.44	2.75	0.07787	299.95	300.65	306.11	306.43	3.8	4.0	10.0	10.3	567.6	478.9	78.6
125	0.65	3	0.08495	299.15	300.15	300.39	300.48	1.5	2.0	2.5	2.6	606.9	503.2	80.0
		3.25	0.09203	298.65	300.15	300.24	300.31	1.0	2.0	2.3	2.4	781.2	524.7	81.3
	0.86	2.75	0.07787	298.95	300.15	300.18	300.30	2.3	3.5	3.5	3.7	452.1	480.7	78.6
		3	0.08495	299.15	299.95	299.95	300.06	2.5	3.3	3.3	3.4	507.6	502.9	80.0
	1.22	2.75	0.07787	301.65	301.45	301.66	301.82	5.0	4.8	5.0	5.2	729.1	480.3	78.6
		3	0.08495	300.15	300.15	301.32	301.47	3.5	3.5	4.7	4.8	504.4	502.5	79.9
		3.25	0.09203	299.95	300.15	301.03	301.18	3.3	3.5	4.4	4.5	525.3	524.0	81.3
	1.52	3	0.08495	301.65	303.15	302.46	302.65	6.5	5.0	5.8	6.0	511.1	502.2	79.9
		3.5	0.09911	304.45	305.65	301.78	301.95	7.8	9.0	5.1	5.3	166.8	544.5	82.4
150	0.89	2.25	0.06371	298.95	299.95	299.37	299.51	4.0	4.8	4.3	4.4	369.7	433.7	74.9
		2.5	0.07079	298.15	298.15	299.05	299.17	3.2	3.0	3.9	4.1	413.6	457.6	76.9
		2.75	0.07787	298.65	299.95	298.76	298.88	3.7	4.8	3.7	3.8	439.2	480.7	78.5
		3	0.08495	297.65	299.15	298.52	298.63	2.7	4.0	3.4	3.5	492.2	502.8	80.0
	1.86	2.25	0.06371	307.95	306.45	308.27	308.54	7.8	5.5	7.7	7.9	436.6	432.9	65.4
		2.5	0.07079	308.45	308.15	308.75	309.00	8.3	7.2	8.1	8.4	405.9	456.6	77.0
		2.75	0.07787	308.15	309.65	308.17	308.42	8.0	8.7	7.6	7.8	412.3	479.7	78.7
	2.33	2.75	0.07787	311.15	311.45	309.43	309.74	11.0	10.5	8.8	9.1	314.4	479.3	73.6
	4.46	2.5	0.07079	311.65	306.15	312.48	313.09	17.0	11.0	17.6	18.2	456.5	454.0	69.8
	4.9	2.75	0.07787	315.15	310.65	318.06	318.68	16.0	10.5	18.5	19.1	480.1	476.7	74.0
		3	0.08495	312.95	313.15	317.98	318.57	14.0	13.0	18.4	19.0	506.7	498.6	80.2